Multiple Antenna Systems: Channel Capacity and Low-Density Parity-Check Codes

Geoffrey James Byers

Submitted in fulfillment of the academic requirements
for the degree of Doctor of Philosophy
in the School of Electrical, Electronic and Computer Engineering
at the University of KwaZulu-Natal, South Africa

March 5, 2005

Abstract

The demand for high data rate wireless communication systems is evident today as indicated by the rapid growth in wireless subscribers and services. High data rate systems are bandwidth intensive but bandwidth is an expensive and scarce commodity. The ability of future wireless systems to efficiently utilise the available bandwidth is therefore integral to their progress and development.

The wireless communications channel is a harsh environment where time varying multipath fading, noise and interference from other users and systems all contribute to the corruption of the received signal. It is difficult to overcome these problems and achieve the high data rates required using single antenna technology. Multiple-input-multiple-output (MIMO) systems have recently emerged as a promising technique for achieving very large bandwidth efficiencies in wireless channels. Such a system employs multiple antennas at both the transmitter and the receiver. These systems exploit the spatial dimension of the wireless channel to achieve significant gains in terms of capacity and reliability over single antenna systems and consequently achieve high data rates. MIMO systems are currently being considered for 3rd generations cellular systems.

The performance of MIMO systems is heavily dependent on the environment in which the system is utilised. For this reason a realistic channel model is essential for understanding the performance of these systems. Recent studies on the capacity of MIMO channels have focused on the effect of spatial correlation but the joint effect of spatial and temporal correlation has not been well studied. The first part of this thesis proposes a new spatially and temporally correlated MIMO channel model which considers motion of the receiver and nonisotropic scattering at both ends of the radio link. The outage capacity of this channel is examined where the effects of antenna spacing, array angle, degree of scattering and receiver motion are investigated. It is shown that the channel capacity still increases linearly with the number of transmit and receive antennas, despite the presence of both spatial and temporal correlation.

The capacity of MIMO channels is generally investigated by simulation. Where analytical expressions have been considered for spatially correlated channels, only bounds or approximations have been used. In this thesis closed form analytical expressions are derived for the ergodic capacity of MIMO channels for the cases of spatial correlation at one end and both ends of the radio link. The latter does not lend itself to numerical integration but the former is shown to be accurate by comparison with simulation results. The proposed analysis is also very general as it is based on the transmit and receive antenna correlation matrices.

Low-density parity-check (LDPC) codes have recently been rediscovered and have been shown to approach the Shannon limit and even outperform turbo codes for long block lengths. Non-binary LDPC codes have demonstrated improved performance over binary LDPC codes in the AWGN channel. Methods to optimise non-binary LDPC codes have not been well developed where only simulation based approaches have been employed, which are not very efficient. For this reason, a new approach is proposed which is based on extrinsic information transfer (EXIT) charts. It is demonstrated that by performing curve matching on the EXIT chart, good non-binary LDPC codes can be designed for the AWGN channel.

In order to approach the theoretical capacity of MIMO channels, many space-time coded, multiple antenna (MA) systems have been considered in the literature. These systems merge channel coding and antenna diversity and exploit the benefits of both. Binary LDPC codes have demonstrated good performance in MA systems but non-binary LDPC codes have not been considered. Therefore, the application of non-binary LDPC codes to MA systems is investigated where the codes are optimised for the system of interest, using a simulation and EXIT chart based design approach. It is shown that non-binary LDPC codes achieve a small gain in performance over binary LDPC codes in MA systems.

Preface

The research work presented in this thesis was performed by Mr Geoffrey Byers, under the supervision of Prof. Fambirai Takawira, at the University of KwaZulu-Natal's School of Electrical, Electronic and Computer Engineering, in the Centre for Radio Access Technologies. This work was partially sponsored by Alcatel SA and Telkom SA as part of the Centre of Excellence programme.

Parts of this thesis have been published in the IEEE Transactions on Vehicular Technology and presented by the student at the 2004 IEEE AFRICON conference, the 2003 IEEE Wireless Communications and Networking Conference (WCNC), the 2002, 2003 and 2004 Southern African Telecommunications Networks and Applications Conference (SATNAC). Parts of this thesis have also been submitted to the IEEE Transactions on Signal Processing, the 2005 IEEE International Conference on Communications (ICC) and the 2005 IEEE Global Telecommunications Conference (GLOBECOM).

The entire thesis, unless otherwise indicated, is the student's own original work and has not been submitted in part, or in whole, to any other University for degree purposes.

Acknowledgements

If we knew what we were doing, it wouldn't be called research, would it?
– Albert Einstein

I wish to thank my supervisor, Prof. Fambirai Takawira, for his invaluable guidance, help and support. His willingness to always set aside his time to assist me in any way has been most appreciated. His valuable input into my research and constant encouragement has been of paramount importance to the success of this thesis.

My parents and brother are owed many thanks for their support and their keen interest in my work. They have always encouraged me in whatever challenge I have taken up in my life and my PhD was no exception.

Thanks are owed to Telkom SA and Alcatel SA for their much appreciated financial support and for providing the equipment necessary for the completion of my PhD.

I would like to thank Dr Hongjun Xu, Dr Glenda Matthews, Dr Nico Crowther and Dr Donald Richards for their assistance with various parts of my research. I would also like to thank Mr Bruce Harrisson, Ms Brigitte Le Breton, Mrs Marie Wayne and Mrs Sharon McGregor for their help with many other issues not directly related to my research.

Finally I would like to thank my postgraduate colleagues for their help and friendship and for providing many hours of entertainment which helped create a most enjoyable working environment.

Contents

List of Figures

List of Tables

Chapter 1

Introduction

1.1 Background

1.1.1 The Wireless Market

Over the last 15 years the cellular industry has experienced tremendous growth, from only 10 million cellular subscribers worldwide in 1990 to 1.5 billion subscribers in March 2004 [1].

Many factors are driving the wireless information revolution. A computer literate society has emerged which is becoming more reliant on data and information. Personal and business lifestyles are placing increased demands on both travel and mobility. High speed and cost effective mobile systems which are small, powerful and application rich are now available thanks to significant advances in technology. The use of internet and mobile services have increased rapidly over the past few years, together with the use of portable computers and electronic commerce. These factors have increased the demand for high data rate wireless communication services which must be available anywhere and anytime.

Wireless systems provide access to these services such as cellular systems for wide area coverage and "wireless hot-spots" for local coverage.

1.1.2 Wireless Systems

In this section some of the existing wireless systems are discussed, starting at the cellular level where wide area coverage is achieved and then moving to systems providing local coverage such as wireless local and personal area networks.

Many cellular systems are present today and an overview of these is given in [2, 3]. The cellular communications industry began in the early 1980s with the introduction of analogue based first-generation Advanced Mobile Phone System (AMPS).

The introduction of second-generation (2G) systems in the 1990s marked the beginning of digital wireless communications. The current 2G systems are the Global System for Mobile communication (GSM), Time Division Multiple Access (TDMA), Personal Digital Cellular (PDC) and Code Division Multiple Access One (cdmaOne). GSM is the most popular 2G system which held a 72% market share in March 2004 [1]. GSM provides data rates up to 14.4 kbps which can be increased using enhanced 2G (2.5G) technologies such as the General Packet Radio Service (GPRS) and Enhanced Data rates for GSM Evolution (EDGE) which achieve 144 kbps and 384 kbps respectively.

Third-generation (3G) systems aimed to achieve an international standard for mobile communications and higher data rates up to 2 Mbps. Unfortunately a true international standard did not materialise and today there are two different 3G systems which are both based on code division multiple access (CDMA). The Universal Mobile Telecommunications System (UMTS) is chosen for the evolution of GSM and PDC networks and for this reason is the 3G network of choice for 85% of mobile operators [3]. CDMA-2000 is chosen for the evolution of cdmaOne networks. In the near future High-Speed Downlink Packet-Access (HSDPA) will be introduced to increase the data rate of UMTS to 10 Mbps. The general trend here is that significantly higher data rates are achieved by each successive generation of cellular networks.

To provide fixed broadband wireless access over a large coverage area, the IEEE 802.16 group of standards were proposed which are commonly known as Worldwide Interoperability for Microwave Access (WiMAX). WiMAX [4] aims to offer peak data rates up to 75 Mbps for ideal conditions and achieve communications up to a maximum range of 50 km using reduced data rates. The IEEE 802.16e standard offers some support for mobility.

Wireless Fidelity (Wi-Fi) is the commercial name for the IEEE 802.11 group of standards. IEEE 802.11b achieves a peak data rate of 11 Mbps while higher data rates up to 54 Mbps can be achieved using 802.11a and 802.11g. These standards allow computers to connect to the internet, a network or another computer. Wi-Fi "hot-spots" are becoming increasingly popular and are present at many airports, hotels, conference venues and shopping complexes. The range of a Wi-Fi network is limited to 50 m in a typical office environment.

Bluetooth [5] is a short range wireless standard which allows portable devices to connect to each other and to other terminals such as computers and also allows a number of devices to form an ad hoc network. In general Bluetooth supports data rates up to 700 kbps over a range of 10 m.

1.1.3 Future Wireless Systems

It is envisaged that in the future, seamless roaming between the various air interfaces will be possible, allowing the user to be always connected in the best possible manner. New or enhanced services such as web browsing, email, video conferencing, streaming video, mobile commerce and a host of multimedia applications are also expected.

These services require high data rates which in turn require large amounts of bandwidth or radio spectrum. However bandwidth is a very expensive and limited commodity as indicated by the high cost of the 3G licenses recently auctioned in Europe. Therefore, technologies which efficiently use the available bandwidth are paramount to the success of future wireless systems.

Work has already begun on wireless systems beyond 3G [6, 7]. Here it is predicted that future systems will achieve data rates of 100 Mbps for high mobility and 1 Gbps for low mobility.

1.2 Wireless Technologies

The wireless channel is a harsh environment where noise, multipath fading and interference from other users and systems all contribute to the corruption of the received signal. A host of technologies are available for improving the performance of wireless communication systems and a few of these will be discussed in this section.

Forward error correction (FEC) codes add redundancy to the transmitted information which can be used at the receiver to correct errors introduced by the channel. Until recently, two main classes of codes existed, block and convolutional codes [8]. A major breakthrough came in 1993 with the invention of turbo codes [9] which were the first practical coding scheme able to approach the Shannon limit. Low-density parity-check codes [10] have recently been rediscovered [11] and are also able to approach the Shannon limit.

In a broadband channel, orthogonal frequency division multiplexing (OFDM) [12] is a robust technique against multipath fading. With OFDM the signal bandwidth is divided into a number of orthogonal subcarriers and the information is transmitted in parallel over these subcarriers. Future wireless systems are considering combining OFDM with multiple access techniques [7].

Current 3G systems are based on CDMA and their performance is limited by the interference from other users and cells. The performance of these systems can be enhanced by attempting to remove this interference using multiuser detection techniques [13].

Receive antenna diversity has been used for many years to improve system performance by combining independently faded replicas of the original signal. Transmit antenna diversity [14] has been considered due to the limitations on the size and cost of the mobile terminal. With both transmit and receive diversity the capacity increases logarithmically with the number of antenna elements. Adaptive or smart antenna [15] systems shape the antenna radiation pattern such that the desired user's signal is enhanced and the interfering users' signals are suppressed. Smart antenna techniques do not perform well under non line-of-sight conditions as there are many interfering signals to cancel.

Multiple-input–multiple-output (MIMO) systems have recently emerged as a promising technique for achieving very large spectral efficiencies in wireless channels. MIMO systems employ multiple antennas at both the transmitter and receiver as shown in Fig. 1.1 and are able to exploit the spatial dimension of the wireless channel which is not well utilised using other technologies. In this way parallel data pipes are set up between transmitter and receiver which greatly enhances capacity as was shown in [16,17] where the capacity increases linearly with the number of antenna elements in a rich scattering environment. Unlike smart antenna systems, MIMO systems work very well in non line-of-sight conditions. An excellent overview of MIMO systems is given in [18] and a discussion on the latest trends in this field as well as future directions is presented in [19]. It is believed that MIMO technologies will play a major role in achieving the spectral efficiency and high data rates required for future wireless systems [6, 7]. To this end MIMO systems are currently under consideration for release 6 of UMTS [20].

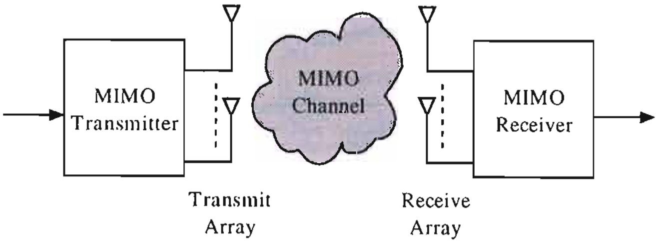

Figure 1.1: A MIMO system.

MIMO systems are able to enhance system performance in the following ways [19] without increasing the transmitted power or system bandwidth:

- **Array gain:** The multiple receive antennas can coherently combine the received signals to increase the signal-to-noise ratio (SNR). This requires channel state information (CSI) to be available to the receiver. The transmitter can also achieve array gain if CSI is available. Array gain is proportional to the number of antennas and improves the power efficiency of wireless systems.
- **Diversity gain:** Diversity is achieved by transmitting multiple replicas of the information signal over independently faded sub channels. In this way the probability of all signals being faded at any one time is significantly reduced which

improves system reliability. In MIMO systems the diversity gain is realised in the spatial dimension and reduces the sensitivity of the system to the effects of time varying multipath fading. The diversity gain is proportional to the product of the number of transmit and receive antennas.

- **Multiplexing gain:** By employing multiple antennas at both the transmitter and receiver, multiple data pipes or channel eigenmodes in the same frequency band are set up, which results in a linear capacity increase with the number of antennas. Therefore, the spectral efficiency is improved and higher data rates can be achieved using the same resources whereby multiple data streams are simultaneously transmitted.

From the perspective of a cellular system these gains translate into increased cell range or coverage, lower power consumption, improved link quality and reliability as well as increased spectral efficiency.

In order to realise the benefits of MIMO systems, various space-time coding schemes [21] have been developed which include layered space-time codes [22], space-time trellis codes [23] and space-time block codes [24,25]. Throughout this thesis multiple antenna (MA) systems refer to the case of multiple antennas at one end or both ends of the radio link while MIMO systems refer to the case of multiple antennas at both ends of the radio link.

1.3 Motivation for Research

The demand for high data rate wireless communication systems is evident but bandwidth is an expensive and scarce commodity. The ability of future wireless systems to efficiently use this radio spectrum is therefore integral to their progress and development.

A number of technologies are available to enhance the performance of wireless systems. Of these, MIMO techniques are one of the most promising. MIMO systems exploit the spatial dimension of the wireless channel and achieve significant gains over single antenna systems, in terms of spectral efficiency and link reliability. A large body of research has already been carried out in this field, covering areas such as field tests, channel modelling, channel capacity and space-time coding. However, there still remain a number of open issues and two of these are considered in this thesis, these being, the capacity of realistic MIMO channels and the design of practical LDPC based coding schemes able to realise the full potential of MIMO systems.

The capacity of MIMO channels is heavily dependent on the propagation environment. Initial work considered uncorrelated fading channels where many realistic effects were not modelled. But realistic channel models are essential for understanding and optimising the performance of MIMO systems. The influence of spatial correlation on the capacity of MIMO channels is becoming increasingly important as terminals grow smaller and utilise more antenna elements. In addition, temporal correlation, as a result of user mobility, is also important to model as future wireless systems are expected to operate at high data rates and high mobility. Recent studies on the capacity of MIMO channels have considered the effects of spatial correlation but the effects of both spatial and temporal correlation have not been well addressed. The first part of this thesis proposes a new spatially and temporally correlated channel model for MIMO systems which considers a number of effects not considered in previous works. The capacity of this channel is then studied through simulation where the influence of antenna spacing, array angle, angle spread and receiver motion on channel capacity is investigated.

Analytical expressions give further insight into the capacity of MIMO channels but these are mathematically difficult to derive and in most cases, bounds or approximations have been used. Spatial correlation has a severe impact on the capacity of MIMO channels but exact analytical expressions for the capacity are not available in the literature. For this reason, closed form analytical expressions are derived for the ergodic capacity of MIMO channels with spatial correlation at one end and both ends of the radio link.

Low-density parity-check (LDPC) codes have recently emerged as a powerful coding technique which are capable of approaching the Shannon limit and are considered a serious competitor to turbo codes. Initially, binary LDPC codes were considered but more recently non-binary versions of these codes have demonstrated improved performance. Although the literature pertaining to the optimisation of binary LDPC codes is fairly well developed where density evolution or extrinsic information transfer (EXIT) charts can be used, there has been little research into the optimisation of non-binary LDPC codes. In this thesis a new method, based on EXIT charts, is proposed to optimise the design non-binary LDPC codes for the AWGN channel.

In an attempt to realise the large spectral efficiencies promised by MIMO channels, many space-time coding techniques for MA systems have been studied. These techniques merge the fields of channel coding and antenna diversity and in this way exploit the diversity available in both the spatial and temporal dimensions. Binary LDPC codes applied to MA systems, have demonstrated good performance. Non-binary LDPC codes have been shown to outperform binary LDPC codes but these have not been considered for MA systems. The performance of non-binary LDPC codes in MA systems is therefore investigated. The structure of these codes is optimised for the system of interest using differential evolution in conjunction with a simulation based and EXIT chart based cost function.

1.4 Thesis Overview

This thesis is divided into six chapters. In chapter 1 the various factors driving the rapidly growing wireless market were discussed and an overview of the existing wireless systems including cellular systems was given. The vision for future wireless systems was presented and various technologies enhancing the performance of wireless systems were described. Motivation for the work done in this thesis was then discussed.

A geometric MIMO channel model is presented in chapter 2 which considers motion of the receiver and non-isotropic scattering at both ends of the radio link. In this way, both spatial and temporal correlation are modelled. A joint space-time cross-correlation function is derived, in closed form, for the geometric model presented. To enable efficient simulation of such a channel, the vector autoregressive stochastic model is used to generate variates with the desired spatial and temporal correlation. The outage capacity of this channel is studied where the effects of antenna spacing, antenna array angle, degree of non-isotropic scattering and receiver motion are investigated.

In chapter 3, new analytical expressions are derived for the ergodic capacity of spatially correlated MIMO channels. Spatial correlation at one end and at both ends of the radio link is considered. The proposed analysis is very general as it is based on the transmit and receive antenna correlations matrices. Simulation results are compared to the analytical expressions in order to assess their accuracy.

Non-binary LDPC codes are introduced in chapter 4 where the encoding and decoding operations as well as the code construction are discussed. Extrinsic information transfer (EXIT) charts are proposed to optimise non-binary LDPC codes for the AWGN channel. The *a priori* information of the LDPC decoder is shown to be accurately modelled using a Gaussian mixture distribution. Analytical expressions are presented for the EXIT curves of the variable and check node decoders for both regular and irregular LDPC codes. It is then demonstrated that by matching the EXIT curves of the variable and check node decoders, good non-binary LDPC codes can be designed.

A novel coding scheme for MA systems is proposed in chapter 5 which is based on non-binary LDPC codes. The optimisation of non-binary LDPC codes is considered for the system of interest where a simulation and EXIT chart based design approach is proposed. The performance of the optimised systems codes are then investigated by simulation.

The final chapter presents the conclusions drawn in this thesis.

1.5 Original Contributions

The original contributions of this thesis include:

1. Derivation of the joint space-time cross-correlation function for a spatially and temporally correlated MIMO channel and the investigation of the effects of spatial and temporal correlation on the outage capacity. [Chapter 2]
2. Derivation of exact analytical expressions for the ergodic capacity of spatially correlated MIMO channels. [Chapter 3]
3. Modelling the *a priori* information of the non-binary LDPC decoder and the application of EXIT charts to the optimisation of non-binary LDPC codes. [Chapter 4]
4. Optimisation of non-binary LDPC codes for MA systems using a simulation and EXIT chart based approach. [Chapter 5]

1.6 Publications

The following publications have resulted from the work done in this thesis:

1. G. J. Byers and F. Takawira, "EXIT charts for the optimisation of non-binary LDPC codes in MIMO systems," *Submitted to IEEE Transactions on Signal Processing.*
2. G. J. Byers and F. Takawira, "Spatially and temporally correlated MIMO channels: Modeling and capacity analysis," *IEEE Transactions on Vehicular Technology*, vol. 53, pp. 634–643, May 2004.
3. G. J. Byers and F. Takawira, "Optimisation of non-binary LDPC codes in MIMO systems," *Submitted to IEEE Global Telecommunications Conference (GLOBECOM)*, St. Louis, Missouri, USA, Nov. 2005.

4. G. J. Byers and F. Takawira, "EXIT charts for non-binary LDPC codes," *Submitted to IEEE International Conference on Communications (ICC)*, Seoul, Korea, May 2005.
5. G. J. Byers and F. Takawira, "Non-binary and concatenated LDPC codes for multiple-antenna systems," *in Proc. IEEE AFRICON*, Gaborone, Botswana, Sep. 2004.
6. G. J. Byers and F. Takawira, "The influence of spatial and temporal correlation on the capacity of MIMO channels," *in Proc. IEEE Wireless Communications and Networking Conference (WCNC)*, New Orleans, Louisiana, USA, Mar. 2003.
7. G. J. Byers and F. Takawira, "Fourier transform decoding of non-binary LDPC codes," *in Proc. Southern African Telecommunications Networks and Applications Conference (SATNAC)*, Stellenbosch, South Africa, Sep. 2004.
8. G. J. Byers and F. Takawira, "Analytical results for the capacity of spatially correlated MIMO channels," *in Proc. Southern African Telecommunications Networks and Applications Conference (SATNAC)*, George, South Africa, Sep. 2003.
9. G. J. Byers and F. Takawira, "On the Capacity of Spatially and Temporally Correlated MIMO Channels," *in Proc. Southern African Telecommunications Networks and Applications Conference (SATNAC)*, Champagne Sports Resort, Drakensberg, South Africa, Sep. 2002.

Chapter 2

Spatially and Temporally Correlated MIMO Channels

2.1 Introduction

The huge potential of MIMO systems was originally demonstrated from an information theoretic view point. The channel capacity C is the theoretical limit to error free transmission. According to Shannon's noisy channel coding theorem, it is possible to achieve reliable communications using advanced signal processing techniques if one transmits at a rate $R < C$.

Initial work on the capacity of MIMO channels [16] and later [17], demonstrated the huge potential of MIMO systems and it was shown that the capacity scales linearly with the number of transmit and receive antennas. A good tutorial on the capacity of MIMO channels is given in [26] and [18, 27] provides an overview of the literature in this field.

The availability of channel state information (CSI) to the transmitter and/or receiver has an impact on the capacity achieved by MIMO systems. In [16], the cases of CSI at the receiver only and CSI at the transmitter and receiver were investigated. If CSI is only available to the receiver, the optimal transmission strategy is to equally divide the transmission power between the transmit antennas. In feedback systems CSI is available to both the transmitter and receiver and waterfilling can be used to optimally allocate the transmission power. However, the gain of waterfilling over the equal power allocation is only significant at low SNRs as discussed in [18]. Furthermore in realistic time-varying channels it is difficult to accurately estimate the CSI at the transmitter. The capacity of MIMO systems with no CSI at the transmitter or receiver was investigated in [28]. In this thesis MIMO systems with CSI at the receiver only will be considered.

Quasi-static fading channels were considered in [17] where the path gains between antennas remained constant for the entire frame and were independent from one frame to the next. Later block fading channels were studied [28, 29] where the transmitted frame spanned a fixed number of independent channel realisations or blocks. In each block the path gains remain constant for a fixed number of symbols. These blocks could be separated in time or frequency.

The MIMO channel itself has a huge impact on the capacity as well as on the performance of practical systems. In [16, 17], it was assumed that the scattering was rich and the antenna elements were well spaced which allowed the path gains between antenna elements to be modelled independently. However, in realistic systems the scattering is not sufficiently rich and the antenna spacing is small due to limitations on the size of the mobile terminal. This results in spatial correlation and mutual coupling between the antenna elements which can limit the capacity of MIMO systems [30]. When either the transmitter or receiver is moving, a quasi-static channel model is no longer appropriate as the path gains change from one symbol to the next. Block fading channel models [28, 29] are not realistic either as they do not account for the correlation between successive symbols. This correlation between successive symbols will be referred to as temporal correlation. Many other parameters influence the capacity achieved by MIMO systems such as path loss, shadowing, delay spread and the Ricean K factor as discussed in [18, 27]. The work in this thesis is concerned with the influence of spatial and temporal correlation on the capacity of narrowband MIMO channels.

A common communications scenario is one where the base station is elevated and unobstructed by local scatterers and the signal is received within a given beamwidth. The user is situated at ground level where a high degree of local scattering occurs due to objects surrounding the user. The effect of spatial correlation on MIMO capacity in such a channel was investigated in [31–34] where the effect of various system parameters on capacity were investigated such as angle spread and antenna spacing. In all cases it was shown that spatial correlation diminishes the capacity achieved by MIMO systems. User mobility, resulting in Doppler spread, was only considered in [33].

Another common scenario occurs when both the transmitter and receiver are surrounded by objects resulting in local scattering at both ends of the radio link. The capacity of this channel was considered in [35–37] and again it was shown that spatial correlation reduces the capacity of MIMO systems. Here the effects of user mobility on channel capacity were not investigated.

Limited correlation between antenna elements at both the transmitter and receiver does not always guarantee maximum capacity. This is known as the keyhole or pinhole effect [36, 38] and can occur in hallways or tunnels but is rarely observed in practice and will not be considered here.

The effect of user mobility on the capacity of MIMO channels is becoming increasingly important as future communication systems are expected to operate at high data rates and high mobility. However, the effect of user mobility on the capacity of MIMO channels with local scattering at both ends of the radio link, resulting in both spatial and temporal correlation, has not been well studied.

In order to study the capacity of the MIMO channel described one can perform a number of field measurements from which the capacity can be calculated. MIMO field measurements have been performed by a number of authors for indoor [39–42], outdoor to indoor [43] and outdoor environments [44–47]. In several cases, capacities near to the theoretical case were obtained. However, capacity results obtained in this manner are only applicable to a particular environment and array configuration. Furthermore it is difficult to study the effect of particular parameters, such as angle spread, on capacity.

An excellent overview of MIMO channel models is given in [48]. These models can be classified as field measurement models or scatterer models. Field measurement models [43, 47, 49] are preferable as they are based on measurement data and give an accurate model of the environment under study. However, scatterer or geometric models are more flexible and give a good description of the communications channel. These models are simple and allow the main characteristics of the channel to be studied without the need for time consuming field measurements. Geometric models have been used to model single antenna systems [50,51] and systems with multiple antennas at one end of the radio link [52–56]. Geometric models for MIMO systems with local scattering at one end [31–33, 57] and both ends of the radio link [35, 36, 57] are available in the literature. However, only the model of [35] considered local scattering at both ends of the radio link as well as user mobility but this model requires lengthly simulations to generate the path gains. What is desired is a closed form expression describing the spatial and temporal correlation from which the path gains of the MIMO channel can be efficiently generated.

In this chapter, a geometric MIMO channel model is presented which accounts for user mobility and non-isotropic scattering at both the transmitter and receiver. From this model, a closed form, joint, space-time cross-correlation function is derived. The path gains of this channel are efficiently generated with the desired spatial and temporal correlation using the vector autoregressive (AR) stochastic model. The effects of spatial and temporal correlation on the outage capacity of this channel are then investigated.

The chapter is arranged as follows. The geometric model for the MIMO channel is presented in section 2.2, for which a joint space-time cross-correlation function is derived. The validity of this model is assessed by comparing the derived correlation function to existing channel models in the literature. The generation of the correlated variates and the calculation of the outage capacity is described in section 2.3 and 2.4 respectively. Simulation results, validating aspects of the model and investigating the outage capacity of this channel are presented in section 2.5. A summary is given section 2.6.

2.2 MIMO Channel Model

In this section a geometric model for a spatially and temporally correlated MIMO channel is presented which considers non-isotropic scattering at both ends of the radio link as well as user mobility. Using this model a joint space-time cross-correlation function is derived which describes the correlation of the path gains across antenna elements and over time. This cross-correlation function is then compared to correlation results in the literature in order to assess the validity of the proposed MIMO channel.

2.2.1 Geometric Model for the MIMO Channel

Consider a narrowband, single user communications system with n_T transmit and n_R receive omnidirectional antenna elements. It is assumed that there is no line-of-sight between the transmitter and receiver and that the fading is caused by scatterers at both ends of the radio link. Only local scattering is considered as it is assumed that the path loss will limit the contribution of remote scatterers to the total channel energy. The transmitter is taken to be fixed and the receiver is taken to be moving.

The link between the transmit and receive antenna arrays is represented using the complex baseband vector notation

$$\underline{y}(t) = \boldsymbol{H}(t)\underline{x}(t) + \underline{n}(t). \tag{2.1}$$

The $n_T \times 1$ transmit vector $\underline{x}(t)$ has elements $x_j(t)$ which denote the signal transmitted from antenna $j = \{1, \ldots, n_T\}$. The $n_R \times 1$ receive vector $\underline{y}(t)$ has elements $y_i(t)$ which denote the signal received on antenna $i = \{1, \ldots, n_R\}$. The $n_R \times 1$ noise vector $\underline{n}(t)$ has elements $n_i(t)$ which denote the additive white Gaussian noise (AWGN) at receiver branch i. Finally $\boldsymbol{H}(t)$ is the $n_R \times n_T$ channel matrix of complex path gains $h_{ij}(t)$ between transmit antenna j and receive antenna i.

The entries of the noise vector are independent and identically distributed complex Gaussian random variables with variance N_0, where N_0 is the noise power spectral density. It is assumed that the channel is known to the receiver and unknown to the transmitter which must equally divide the total transmit power over all antennas.

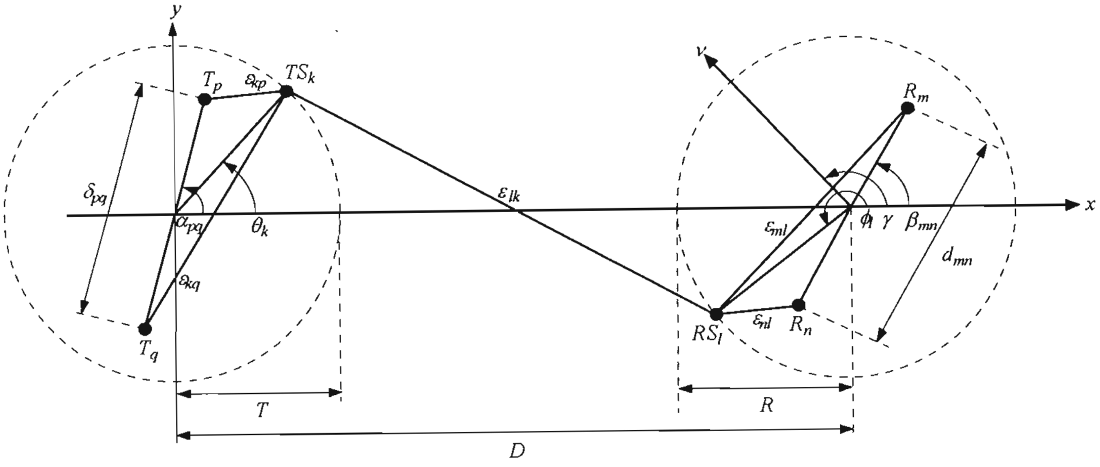

Figure 2.1: Geometric model for the MIMO channel with $n_T = n_R = 2$.

In Fig. 2.1 a geometric model for the MIMO channel under consideration is presented where $n_T = n_R = 2$. This general structure can be used to represent any array configuration. The geometric model presented here is the two-ring model which has been considered by a number of authors [35,36,48,54,57] to model local scattering at both the transmitter and receiver. The two-ring model is a generalisation of the classic one-ring model employed by Jakes [50] where a ring of scatterers is used to model local scattering around the user.

There are K omnidirectional scatterers at the transmitter which lie on a ring of radius T where the kth transmit scatterer is denoted by TS_k. Similarly there are L omnidirectional scatterers at the receiver which lie on a ring of radius R where the lth receive scatterer is denoted by RS_l. Only local scattering is considered i.e. $T \ll D$ and $R \ll D$ where D is the distance between the transmitter and receiver.

Each scatterer introduces a gain and a phase shift. It is assumed that the gain and phase shift introduced by a particular scatterer is dependent on the direction of the rays arrival. Thus the gain and phase shift introduced by RS_l when a ray is received from TS_k is different to that introduced when a ray is received from $TS_{k'}$ where $k \neq k'$. If the antenna spacing is small relative to the scattering radius it can be assumed that rays from different antenna elements arrive at a particular scatterer at approximately the same angle. Thus for a particular scatterer the gain and phase shift is the same for rays arriving from different antenna elements. For this reason g_{lk} and ψ_{lk} are used to denote the joint gain and phase shift of the scatterers TS_k and RS_l. A similar assumption was made in [35] and this avoids the difficulties experienced in the two-ring model discussed in [48]. The scatterer gains are taken to be independent, finite variance, positive random variables which are independent of the scatterer phase shifts. Furthermore it is assumed that

$$\frac{1}{KL}\sum_{k=1}^{K}\sum_{l=1}^{L}E[g_{lk}^2]=1. \tag{2.2}$$

The scatterer phase shifts are independent and identically distributed and uniformly distributed over the interval $[0,2\pi)$.

Both scattering rings are assumed to be fixed and the motion of the receiver is modelled by a speed ν and a direction γ. By making these assumptions a stationary cross-correlation function is obtained as discussed in [33].

Consider a single transmission path from transmit antenna T_p to receive antenna R_m where the power transferred through this link is Ω_{mp}. The plane waves transmitted from antenna T_p are scattered by the transmit scatterers and then by the receive scatterers which results in many rays impinging on antenna R_m. The channel gain $h_{mp}(t)$ for the $T_p - R_m$ link, considering the contributions of all scatterers, can be represented as

$$\begin{aligned} h_{mp}(t) &= \sqrt{\Omega_{mp}}\lim_{K,L\to\infty}\frac{1}{\sqrt{KL}}\sum_{k=1}^{K}\sum_{l=1}^{L}g_{lk} \\ &\quad\cdot\exp\left[\jmath\psi_{lk}-\jmath\frac{2\pi}{\lambda}(\varepsilon_{kp}+\varepsilon_{lk}+\varepsilon_{ml})+\jmath 2\pi f_D\cos(\phi_l-\gamma)t\right]. \end{aligned} \tag{2.3}$$

Here, ε_{kp}, ε_{lk}, ε_{ml} are the distances as shown in Fig. 2.1, λ is the carrier wavelength, $f_D=\nu/\lambda$ is the maximum Doppler frequency and $\jmath=\sqrt{-1}$.

Given the statistical properties of the channel, the central limit theorem states that $h_{mp}(t)$ is a zero-mean, complex Gaussian random process. Therefore the envelope of $|h_{mp}(t)|$ is a Rayleigh fading process.

2.2.2 Space-Time Cross-Correlation Function

The joint space-time cross-correlation function for the MIMO channel presented is now derived in a similar manner to [33]. The correlation between the links $T_p - R_m$ and $T_q - R_n$ for a time delay τ is defined as

$$\rho_{mp,nq}(t,\tau) = \rho_{mp,nq}(\tau) = \frac{E[h_{mp}(t)h_{nq}^*(t+\tau)]}{\sqrt{\Omega_{mp}\Omega_{nq}}} \tag{2.4}$$

where * is the complex conjugate. This expression defines the spatial correlation between transmission paths which is related to the temporal correlation over time if the receiver is moving.

The space-time cross-correlation is calculated by substituting (2.3) into (2.4) and after some cancellation of terms and noting that the random variables g_{lk} and ψ_{lk} are independent,

$$\begin{aligned} \rho_{mp,nq}(\tau) &= \lim_{K,L\to\infty} \frac{1}{KL} \sum_{k=1}^{K}\sum_{l=1}^{L}\sum_{k'=1}^{K}\sum_{l'=1}^{L} E[g_{lk}g_{l'k'}] \cdot E[\exp(\jmath\psi_{lk} - \jmath\psi_{l'k'})] \\ &\quad \cdot \exp\Big[-\jmath\frac{2\pi}{\lambda}(\varepsilon_{kp} + \varepsilon_{lk} + \varepsilon_{ml} - \varepsilon_{k'q} - \varepsilon_{l'k'} - \varepsilon_{nl'}) \\ &\qquad -\jmath 2\pi f_D \cos(\phi_{l'} - \gamma)\tau \Big]. \end{aligned} \tag{2.5}$$

Now, $E[g_{lk}g_{l'k'}] = 0$ if $k \neq k'$ or $l \neq l'$, as the random variables g_{lk} are independent and for this reason (2.5) reduces to

$$\begin{aligned} \rho_{mp,nq}(\tau) &= \lim_{K,L\to\infty} \frac{1}{KL} \sum_{k=1}^{K}\sum_{l=1}^{L} E[g_{lk}^2] \\ &\quad \cdot \exp\Big[-\jmath\frac{2\pi}{\lambda}(\varepsilon_{kp} + \varepsilon_{ml} - \varepsilon_{kq} - \varepsilon_{nl}) - \jmath 2\pi f_D \cos(\phi_l - \gamma)\tau \Big]. \end{aligned} \tag{2.6}$$

An important result here is that the correlation between links is independent of the parameter ε_{lk} and hence independent of D. In general (2.6) must be evaluated using numerical methods. However by making the approximations, discussed in this section, a closed form expression for (2.6) can be obtained. As the number of scatterers approaches infinity, $E[g_{lk}^2]/(KL) = p(\theta)p(\phi)d\theta d\phi$ [33] where $p(\theta)$ and $p(\phi)$ are the probability distributions of the transmit and receive scatterers respectively. Therefore (2.6) can be expressed in integral form as follows

$$\begin{aligned}\rho_{mp,nq}(\tau) &= \int_{-\pi}^{\pi}\int_{-\pi}^{\pi} \exp\Big\{-\jmath\frac{2\pi}{\lambda}(\varepsilon_{\theta p}+\varepsilon_{m\phi}-\varepsilon_{\theta q}-\varepsilon_{n\phi}) \\ &\qquad -\jmath 2\pi f_D\cos(\phi-\gamma)\tau\Big\}p(\theta)p(\phi)d\theta d\phi \qquad (2.7)\end{aligned}$$

where the term $\varepsilon_{\theta p}$ is the distance from T_p to the point on the transmit scattering ring at an angle θ from the array centre and the other ε terms are defined in a similar fashion.

For a given scatterer distribution (2.7) can be calculated numerically using the following equations which are derived using the law of cosines

$$\begin{aligned}\varepsilon_{\theta p}^2 &= \frac{\delta_{pq}^2}{4}+T^2-\delta_{pq}T\cos(\alpha_{pq}-\theta)\\ \varepsilon_{\theta q}^2 &= \frac{\delta_{pq}^2}{4}+T^2+\delta_{pq}T\cos(\alpha_{pq}-\theta)\\ \varepsilon_{m\phi}^2 &= \frac{d_{mn}^2}{4}+R^2-d_{mn}R\cos(\phi-\beta_{mn})\\ \varepsilon_{n\phi}^2 &= \frac{d_{mn}^2}{4}+R^2+d_{mn}R\cos(\phi-\beta_{mn}). \qquad (2.8)\end{aligned}$$

The integration of (2.7) can be simplified by assuming $T \gg \delta_{pq}$ and $R \gg d_{mn}$ and by using the approximation $\sqrt{1+x} \approx 1 + x/2$. Thus the equations in (2.8) simplify to

$$\begin{aligned}\varepsilon_{\theta p} &\approx T-\frac{\delta_{pq}}{2}\cos(\alpha_{pq}-\theta)\\ \varepsilon_{\theta q} &\approx T+\frac{\delta_{pq}}{2}\cos(\alpha_{pq}-\theta)\\ \varepsilon_{m\phi} &\approx R-\frac{d_{mn}}{2}\cos(\phi-\beta_{mn})\\ \varepsilon_{n\phi} &\approx R+\frac{d_{mn}}{2}\cos(\phi-\beta_{mn}). \qquad (2.9)\end{aligned}$$

Many different scatterer distributions have been proposed in the literature such as the uniform, Gaussian, wrapped Gaussian and the cardioid pdfs. In this thesis the von Mises pdf [51] is used which approximates many of these distributions and provides mathematical convenience leading to closed form solutions for many problems. In [51], it was shown that this pdf provides a good fit to measured results. The von Mises pdf is defined as [51]

$$p(\theta) = \frac{1}{2\pi I_0(\kappa)}\exp\left[\kappa\cos(\theta-\mu)\right], \quad \theta \in [-\pi,\pi). \qquad (2.10)$$

Here $I_0(\cdot)$ is the modified Bessel function of the 1st kind of order zero, $\mu \in [-\pi, \pi)$ is the mean angle at which the scatterers are distributed on the ring and κ controls the spread of scatterers around this mean. When $\kappa = 0$, $p(\theta) = 1/2\pi$ is a uniform distribution and one has isotropic scattering. As κ increases, the scatterers become more clustered around μ and the scattering becomes increasingly non-isotropic.

By grouping the terms in (2.7) into those containing θ and those containing ϕ the double integral can be calculated as the product of two single integrals corresponding to the transmit and receive antenna correlations, $\rho^T_{p,q}$ and $\rho^R_{m,n}(\tau)$ respectively. Note that the transmit antenna correlation is independent of τ. Separable transmit and receive antenna correlations were also considered in [36, 37, 43, 47, 49]. Thus the space-time cross-correlation function can be expressed as

$$\rho_{mp,nq}(\tau) = \rho^T_{p,q} \cdot \rho^R_{m,n}(\tau). \tag{2.11}$$

Let $a = 2\pi f_D \tau$, $b_{pq} = 2\pi\delta_{pq}/\lambda$ and $c_{mn} = 2\pi d_{mn}/\lambda$. Now substituting $p(\theta)$ and $p(\phi)$ with (2.10), using the approximate expressions in (2.9) and applying some common trigonometric identities, (2.7) can be rewritten as

$$\begin{aligned} \rho^T_{p,q} &\approx \frac{1}{2\pi I_0(\kappa_T)} \int_{-\pi}^{\pi} \exp\Big\{ (\jmath b_{pq}\cos\alpha_{pq} + \kappa_T \cos\mu_T)\cos\theta \\ &\qquad + (\jmath b_{pq}\sin\alpha_{pq} + \kappa_T\sin\mu_T)\sin\theta \Big\} d\theta && (2.12) \\ \rho^R_{m,n}(\tau) &\approx \frac{1}{2\pi I_0(\kappa_R)} \int_{-\pi}^{\pi} \exp\Big\{ (\jmath c_{mn}\cos\beta_{mn} - \jmath a\cos\gamma + \kappa_R\cos\mu_R)\cos\phi \\ &\qquad + (\jmath c_{mn}\sin\beta_{mn} - \jmath a \sin\gamma + \kappa_R\sin\mu_R)\sin\phi \Big\} d\phi && (2.13) \end{aligned}$$

Using the following integral [58, eq. 3.338-4]

$$\int_{-\pi}^{\pi} e^{x\cos z + y\sin z} dz = 2\pi I_0\left(\sqrt{x^2+y^2}\right) \tag{2.14}$$

closed form expressions for the transmit and receive antenna correlations are given by

$$\begin{aligned} \rho^T_{p,q} &\approx \frac{1}{I_0(\kappa_T)} \cdot I_0\Big\{ \big[\kappa_T^2 - b_{pq}^2 + 2\jmath\kappa_T b_{pq}\cos(\alpha_{pq} - \mu_T)\big]^{1/2} \Big\} && (2.15) \\ \rho^R_{m,n}(\tau) &\approx \frac{1}{I_0(\kappa_R)} \cdot I_0\Big\{ \big[\kappa_R^2 - a^2 - c_{mn}^2 + 2ac_{mn}\cos(\beta_{mn} - \gamma) \\ &\qquad + 2\jmath\kappa_R c_{mn}\cos(\beta_{mn} - \mu_R) - 2\jmath a\kappa_R\cos(\gamma - \mu_R)\big]^{1/2} \Big\}. && (2.16) \end{aligned}$$

The cross-correlation function obtained here is in a compact closed form and one can easily generate new correlation results for different configurations as opposed to simulation based models [35] where lengthly simulations are required.

2.2.3 Validity of the MIMO Channel Model

In order to validate this channel model, one should ideally compare these results to field measurements. Because this model is very general, field measurements would need to be averaged over a range of environments. To the extent of the author's knowledge such results are currently not available in the literature for comparison.

In section 2.5.1, the cross-correlation functions (2.15) and (2.16) are compared to the correlation results obtained from the geometric model to assess the validity of the derivation where good agreement is observed. The validity of this channel model is also assessed by comparison of the derived correlation results with existing channel models in the literature. The transmit antenna correlation (2.15) is a special case of the receive antenna correlation (2.16) for the case of $\tau = 0$. For this reason only (2.16) will be compared with existing models. The model proposed in [33] was also validated in this way.

For the case of a single receive antenna ($d_{mn} = 0$) and isotropic scattering ($\kappa_R = 0$), (2.16) reduces to Clarke's model for temporal correlation $\rho^R_{1,1}(\tau) = J_0(2\pi f_D \tau)$ [50]. Here $J_0(\cdot)$ is the zeroth-order Bessel function of the 1st kind. When there is non-isotropic scattering around the user ($\kappa_R \neq 0$) and $\gamma = \pi$ (2.16) simplifies to

$$\rho^R_{1,1}(\tau) = \frac{1}{I_0(\kappa_R)} \cdot I_0\Big(\sqrt{\kappa_R^2 - 4\pi^2 f_D^2 \tau^2 + 4\pi \jmath f_D \tau \kappa_R \cos \mu_R}\Big) \tag{2.17}$$

which is the temporal correlation model of [51, eq. 2] which demonstrated good agreement with measured results.

For the case of multiple antennas at the receiver where a uniform linear array is used (2.16) reduces to Lee's spatio-temporal model [52, Sec. VI] which assumes isotropic scattering around the user. This result is obtained by setting $\kappa_R = 0$, $\beta_{mn} = \pi$ and

$f_D = -f_D$ which gives

$$\rho^R_{m,n}(\tau) = J_0\left(\sqrt{a^2 + c_{mn}^2 + 2ac_{mn}\cos\gamma}\right). \tag{2.18}$$

For non-isotropic scattering around the user with $\beta_{mn} = \pi$ and $f_D = -f_D$ (2.16) can be reduced to the spatio-temporal model of [56, eq. 3] as follows

$$\begin{aligned} \rho^R_{m,n}(\tau) &= \frac{1}{I_0(\kappa_R)} \cdot I_0\Big\{\big[\kappa_R^2 - a^2 - c_{mn}^2 - 2ac_{mn}\cos\gamma \\ &\qquad -2\jmath\kappa_R c_{mn}\cos\mu_R - 2\jmath a\kappa_R\cos(\mu_R - \gamma)\big]^{1/2}\Big\} \end{aligned} \tag{2.19}$$

which was shown to agree well with correlation results published in the literature.

2.3 Generation of the Correlated Variates

The generation of correlated variates with the desired spatial and temporal correlation is described in this section. A direct approach is to linearly transform sequences of uncorrelated variates using the square root of desired correlation matrix. This method is computationally intensive and not feasible for long sequences. For example if N symbols are transmitted from each antenna in a single frame and $M = n_T n_R$, the computational complexity required to calculate the square root of the $NM \times NM$ correlation matrix using Cholesky reduction is $O((NM)^3)$ and to generate each frame of correlated variates is $O((NM)^2)$.

Previous methods used to efficiently generate spatially and temporally correlated fading processes, generated independent fading processes with the desired autocorrelation function, which were then multiplied by a colouring matrix to obtain the desired cross-correlation function. This method of generation is only suitable when the temporal and spatial correlation statistics are separable. In [59], the vector autoregressive (AR) stochastic model of [60] was generalised to multiple channels to generate Rayleigh fading processes with specified autocorrelation and cross-correlation functions.

The correlation function in this thesis is complex and has joint statistics and for this reason the AR model for variates with correlated quadrature components [59] is used. The complexity of the AR model can be reduced because the transmit and receive antenna correlation functions are separable. Note that the transmit antenna correlation function describes spatial correlation only while the receive antenna correlation function jointly describes spatial and temporal correlation.

The following process is followed to generate the spatially and temporally correlated variates. For each time instance t a $n_R \times n_T$ matrix $\boldsymbol{U}_t$ of independent zero mean complex Gaussian random variates with unit variance is generated. The $n_R \times n_T$ matrix $\boldsymbol{V}_t$ with the desired transmit antenna correlation is generated by

$$\boldsymbol{V}_t = \boldsymbol{U}_t \sqrt{\boldsymbol{\Sigma}_T} \tag{2.20}$$

where $\boldsymbol{\Sigma}_T$ is the $n_T \times n_T$ transmit antenna correlation matrix with elements $\rho^T_{p,q}$ calculated using (2.15). The matrix square root of $\boldsymbol{\Sigma}_T$ is

$$\sqrt{\boldsymbol{\Sigma}_T} = \boldsymbol{X} \begin{bmatrix} \sqrt{\sigma_1} & \cdots & 0 \\ \vdots & \ddots & \vdots \\ 0 & \cdots & \sqrt{\sigma_{n_R}} \end{bmatrix} \boldsymbol{X}^{\dagger} \tag{2.21}$$

where $\dagger$ is the transpose conjugate, $\boldsymbol{X} = [\underline{x}_1, \ldots, \underline{x}_{n_R}]$ and σ_i and $\underline{x}_i$ are the eigenvalues and eigenvectors of $\boldsymbol{\Sigma}_T$ respectively.

The correlated matrix $\boldsymbol{V}_t$ is then used as the input to the vector AR stochastic model [59, Sec. 3-B] where (2.16) is used to calculate the required space-time correlation matrix at the receiver.

2.4 Calculation of the Outage Capacity

For the system of interest, the transmitted frame spans a fixed number of symbols which generally occurs when delay constraints are imposed such as in speech transmission systems. In this case a capacity in the Shannon sense does not exist with non-zero probability. For this reason the outage capacity [16, 17] is employed which has been used to study the capacity of many communication systems. The outage capacity C_{out} is associated with an outage probability P_{out} which gives the probability that the channel capacity C falls below C_{out}. This can be expressed mathematically as

$$P_{out} = P(C < C_{out}). \tag{2.22}$$

The normalised capacity C_t for a particular realisation $\boldsymbol{H}_t$ of a MIMO channel at time t is given by [16,17]

$$C_t = \log_2 \det \left(\boldsymbol{I}_{n_R} + \frac{\rho}{n_T} \boldsymbol{H}_t \boldsymbol{H}_t^\dagger \right) \text{ bps/Hz} \tag{2.23}$$

where $\det(\cdot)$ is the matrix determinant, $\boldsymbol{I}_{n_R}$ is the $n_R \times n_R$ identity matrix and ρ is the average SNR at each receive antenna. The capacity of a frame comprising N symbols is [29,32]

$$C = \frac{1}{N} \sum_{t=1}^{N} C_t \text{ bps/Hz}. \tag{2.24}$$

2.5 Simulation Results

In this section, the correlation results obtained from the geometric model are compared to the derived space-time cross-correlation function. The outage capacity of the proposed MIMO channel is then investigated.

The expressions derived for the correlation at the transmitter and receiver in (2.15) and (2.16) can be applied to any array configuration. Here uniform linear arrays (ULAs) are considered where the antenna spacing at the transmitter and receiver is given by δ and d respectively. The angle of the transmit and receive antenna arrays is given by α and β respectively. In this way $\delta_{pq} = \delta(p-q)$ and $\alpha_{pq} = \alpha$ for the transmit array and $d_{mn} = d(m-n)$ and $\beta_{mn} = \beta$ for the receive array. It is assumed that the scatterers are centred around the x-axis facing the opposing antenna array which gives $\mu_T = 0°$ and $\mu_R = 180°$.

Unless indicated otherwise, the following default parameters are used. The carrier frequency is set to 1 GHz which corresponds to a carrier wavelength λ of 0.3 m. The SNR ρ is set to 10 dB and the frame length N is set to 100. The number of transmit and receive antennas is set to 3 i.e. $n_T = n_R = 3$ and the antenna arrays have $\delta = d = \lambda$ and $\alpha = \beta = 45°$. The normalised Doppler frequency $f_D T_s$ is set to 0.1 where T_s is the symbol period and the receiver is moving at an angle of $\gamma = 20°$. The degree of local scattering at the transmitter and receiver is $\kappa_T = \kappa_R = 10$. The order of the AR model is 80.

2.5.1 Correlation Results

To assess the accuracy of the derived cross-correlation function (2.11) and the AR model, these cross-correlations are compared to those obtained from the geometric model given in Fig. 2.1. The path gains of the geometric model are calculated from (2.3) using the parameters, $K = L = 10$, $T = R = 10$ m and $D = 1000$ m. The scatterers are distributed around the transmit and receive antenna arrays according to the von Mises distribution (2.10). In all cases the default system parameters are used. The results are illustrated in Fig. 2.2 where good agreement of the closed form cross-correlation function and the AR model with the geometric model is observed.

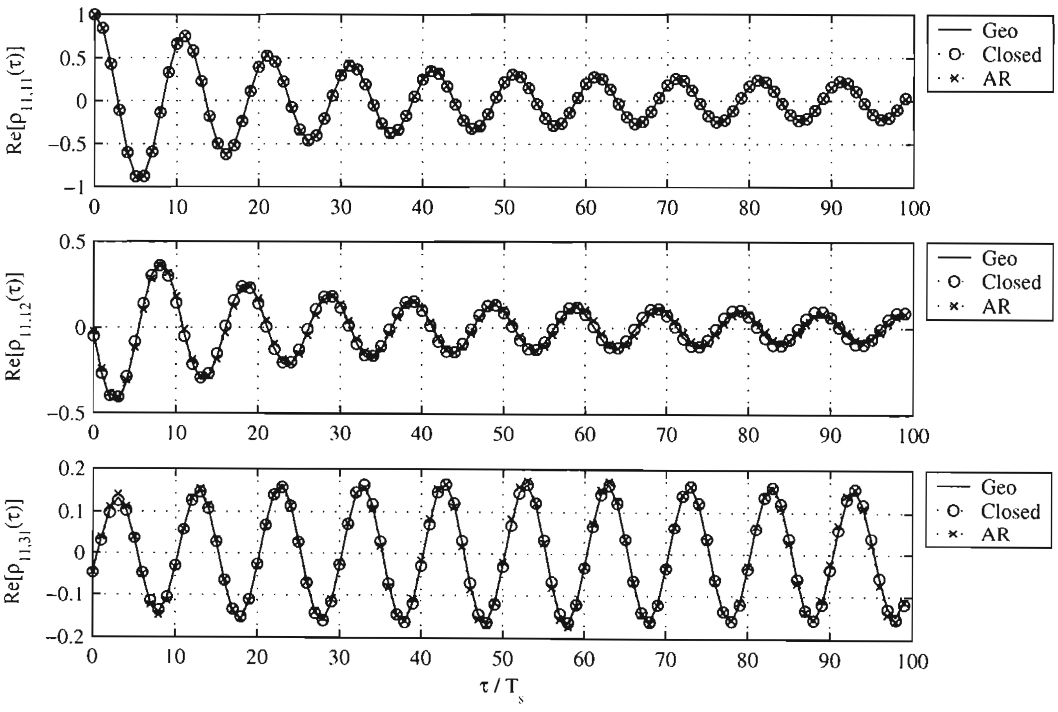

Figure 2.2: Autocorrelation and cross-correlation functions for the geometric model (Geo), the closed form cross-correlation function (Closed) and the AR model (AR).

2.5.2 Outage Capacity Results

The effect of spatial and temporal correlation on the outage capacity of the proposed MIMO channel is investigated here for a 1% outage probability. The influence of a number of system parameters on the outage capacity are now examined.

In Fig. 2.3 the capacity dependence on the transmitter and receiver antenna spacing is illustrated. Increasing δ beyond 2λ and d beyond 5λ has a negligible effect on capacity. A larger antenna spacing is thus required at the receiver to achieve maximum capacity. This is because the receiver is moving and for this reason a larger antenna spacing is required to overcome the temporal correlation. It is also observed that a reasonable antenna spacing at both ends of the radio link is necessary to achieve maximum capacity.

The influence of the transmitter and receiver array angle is studied in Fig. 2.4. The change in capacity is greatest when the antenna array is between 10° and 60°. Note that the capacity achieved for $\alpha = \beta = 45°$ is only 0.6 bps/Hz lower than the maximum capacity achieved when $\alpha = \beta = 90°$.

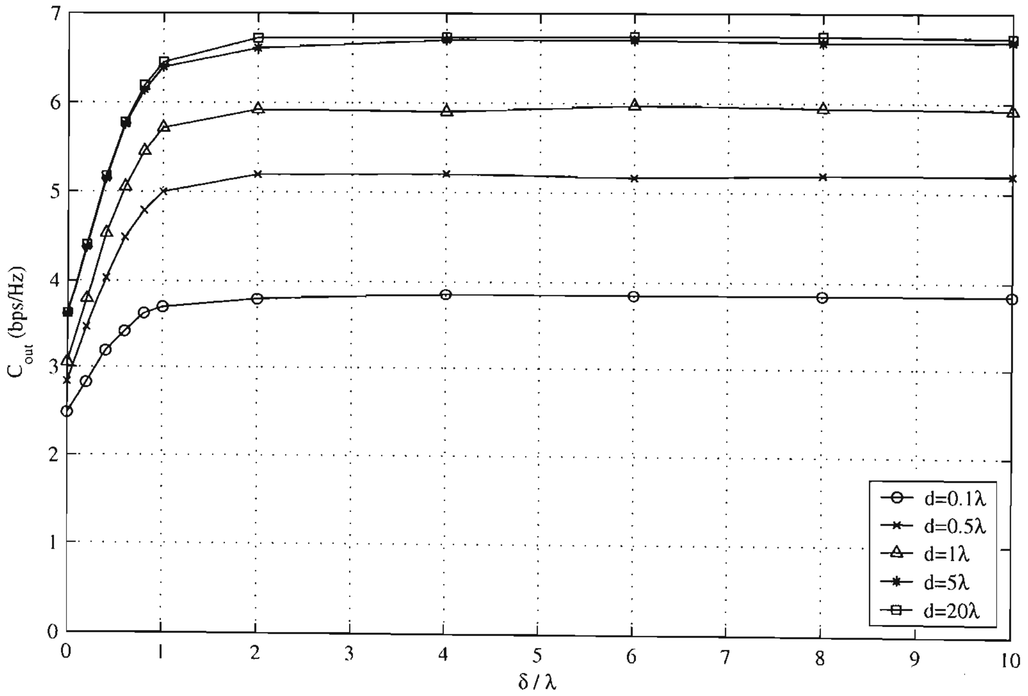

Figure 2.3: Capacity dependence on the transmitter and receiver antenna spacing (δ, d).

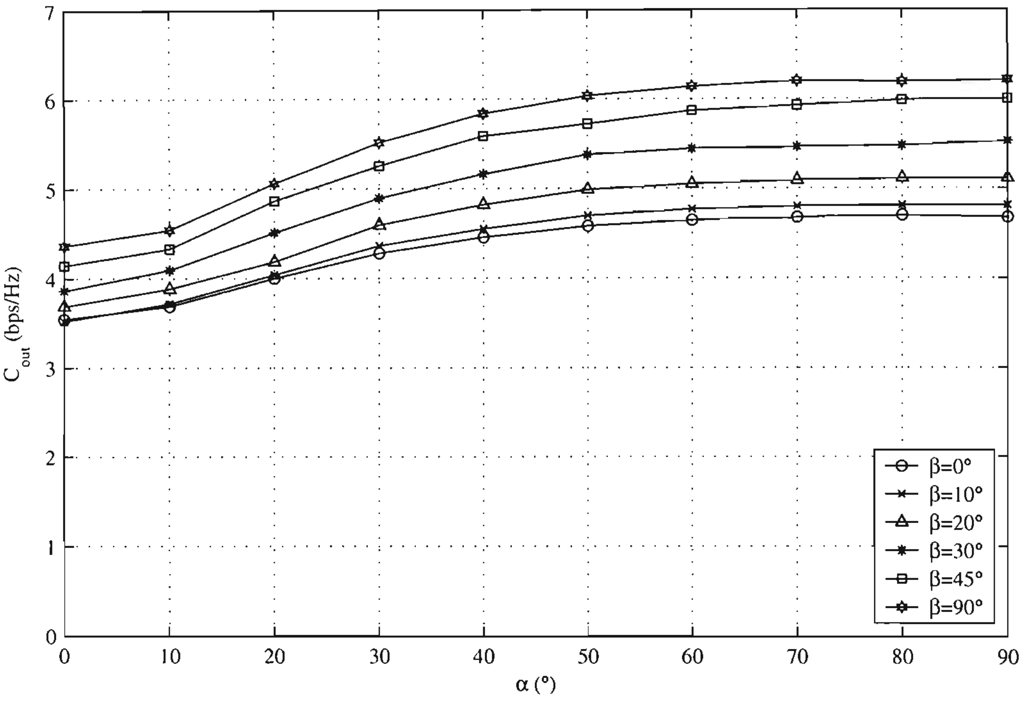

Figure 2.4: Capacity dependence on the transmitter and receiver array angle (α, β).

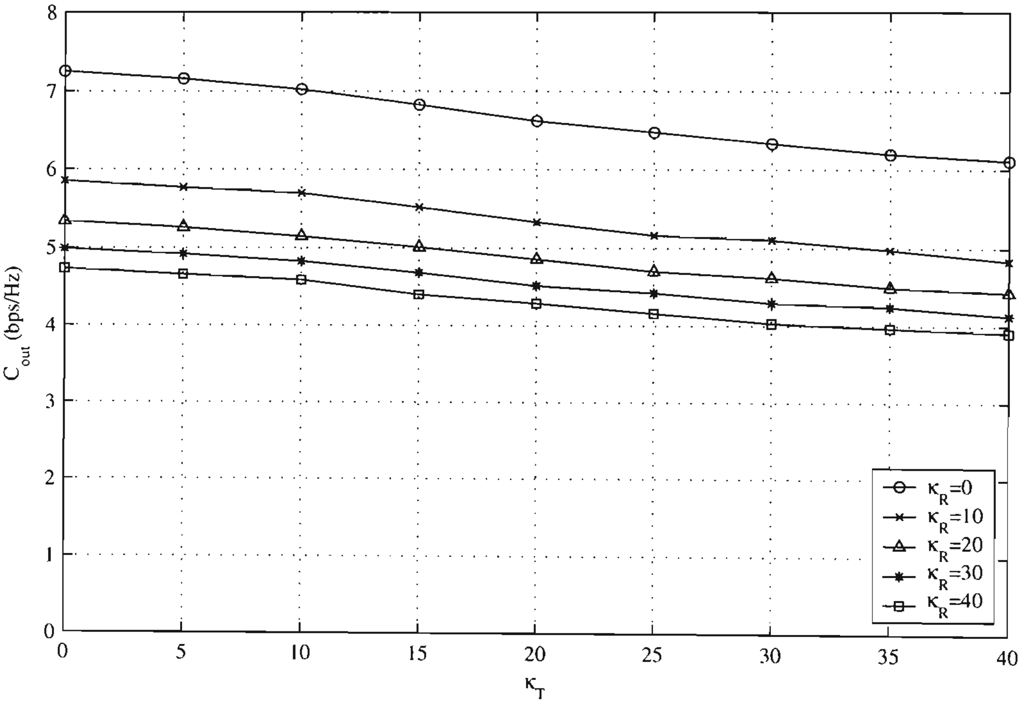

Figure 2.5: Capacity dependence on the degree of non-isotropic scattering at the transmitter and receiver (κ_T, κ_R).

The effect of non-isotropic scattering is observed in Fig. 2.5. The capacity decreases as the scattering becomes more non-isotropic which corresponds to an increase in κ_T and κ_R. The capacity is more sensitive to a change in κ_R than κ_T where a capacity gain of 2.5 bps/Hz is obtained for a change in κ_R from 0 to 40 and only 1 bps/Hz for the same change in κ_T. This is due to the movement of the receiver where the amount temporal correlation is also dependent on κ_R.

In Fig. 2.3 to Fig. 2.5 it is shown that as the spatial correlation at either the transmitter or receiver increases so the capacity decreases. In all cases optimising the parameters at only one end of the radio link is not sufficient to ensure maximum capacity thus both ends of the radio link must be considered.

In Fig. 2.6 and Fig. 2.7 the outage capacity is plotted with respect to n which describes a system with n transmit and n receive antennas. In Fig. 2.6 the capacity is given for various degrees of spatial correlation. The system described at the beginning of this section is denoted by 'Default' and the case of no spatial correlation is denoted by 'Uncorrelated'. The remaining curves give the capacity of the default system with various parameters modified as indicated in the legend. An important result here is that capacity always increases linearly with n despite the presence of spatial and temporal correlation. Only the slope of the capacity curve is reduced as the spatial correlation increases.

The effect of temporal correlation is investigated in Fig. 2.7 by varying the normalised Doppler frequency and the receiver direction γ. The case of temporally uncorrelated fading is shown and is denoted by 'Uncorrelated'. It is observed that an increase in Doppler frequency results in an increase in capacity due to the decrease in temporal correlation. Increasing γ, which results in the receiver moving more towards the transmitter, also causes an increase in capacity. Unlike the effect of spatial correlation, an increase in temporal correlation does not effect the slope or linearity of the capacity curve with respect to n, but results in a downward shift of the capacity curve.

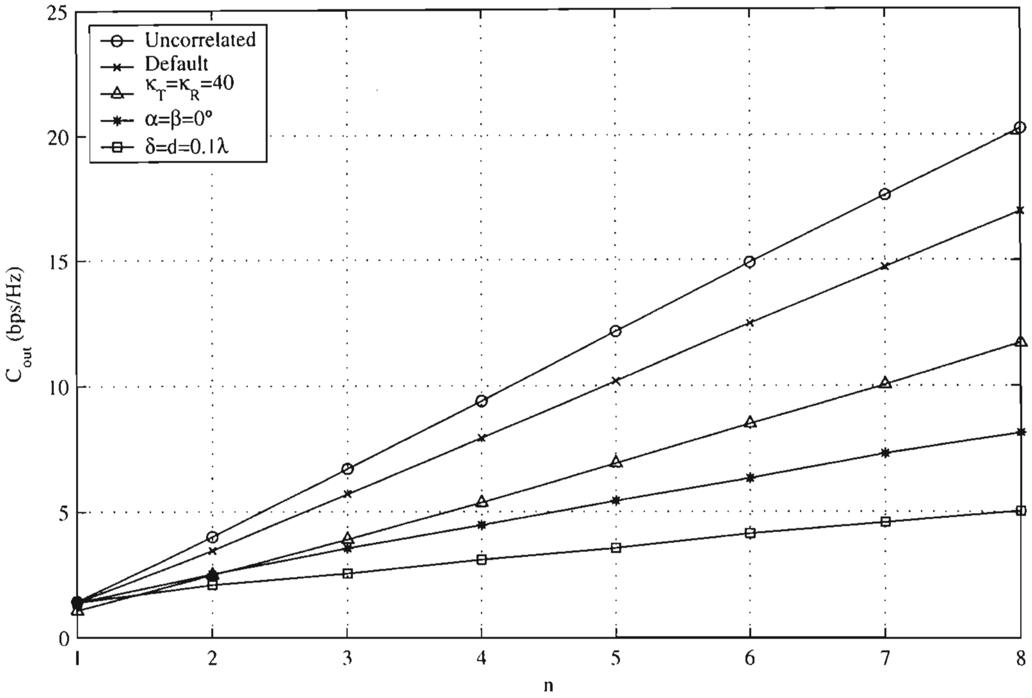

Figure 2.6: Capacity dependence on the number of transmit and receive antennas (n) for varying degrees of spatial correlation.

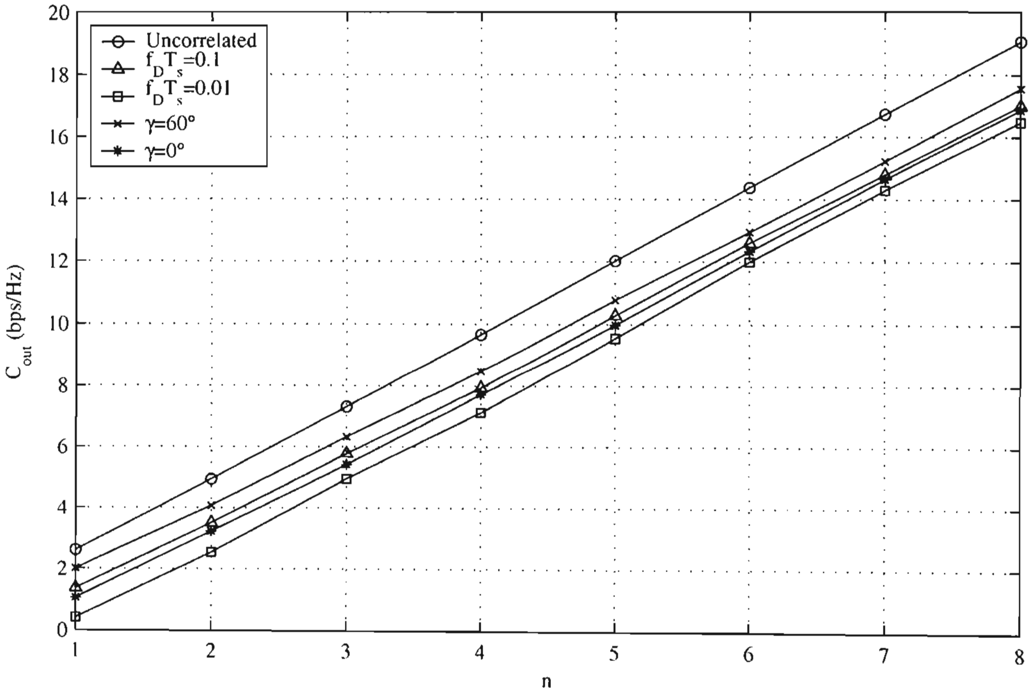

Figure 2.7: Capacity dependence on the number of transmit and receive antennas (n) for varying degrees of temporal correlation.

2.6 Summary

In this chapter the outage capacity of MIMO channels with receiver motion and non-isotropic scattering at both ends of the radio link was considered. A geometric model for this channel was introduced and a closed form space-time cross-correlation function was then derived. This derivation was shown to be accurate by comparison with correlation results obtained from the geometric model and existing models in the literature. The MIMO channel with the specified correlation statistics was generated using the vector AR stochastic model.

The outage capacity of this channel was then investigated where the effects of antenna spacing, antenna array angle, degree of non-isotropic scattering, Doppler frequency and receiver direction were considered. It was shown that it is necessary to optimise the parameters at both ends of the radio link in order to achieve maximum capacity. Furthermore, the antenna spacing at the receiver was more critical than that at the transmitter. It was also shown that in the presence of both spatial and temporal correlation, the capacity still scales linearly with respect to n, where n describes the case of n transmit and n receive antennas. In general, an increase in spatial correlation reduced the slope of the capacity curve while an increase in temporal correlation caused a downward shift of the capacity curve.

Chapter 3

Analysis of Spatially Correlated MIMO Channels

3.1 Introduction

The capacity of MIMO channels has largely been studied through Monte-Carlo simulation methods due to the difficulty experienced in deriving analytical expressions. Analytical expressions give a deeper understanding of the main factors affecting capacity. A good overview of the analytical work on MIMO capacity is given in [18, Sec. III] from a different perspective to that presented here.

Initially analytical expressions for uncorrelated MIMO channels were considered. The first analytical expressions appeared in [16] where the ergodic or average capacity of the MIMO channel was derived. The capacity was calculated by integrating over the eigenvalue distribution of a Wishart matrix to obtain an integral expression for the capacity which contained Laguerre polynomials. This integral was then solved numerically. A lower bound on ergodic capacity was given in [17] using chi-squared variates. Analytical bounds were also investigated in [31, 61, 62]. In [63–65], the capacity distribution function was approximated using a Gaussian distribution which was shown to be accurate in most cases. An exact expression for the ergodic capacity was derived in [71] but unlike [16] did not require numerical integration. Exact densities and distribution functions were given in [66] for the capacity of systems with a few antennas in uncorrelated Ricean fading.

It is well known that spatial correlation reduces the capacity of MIMO channels as was shown in the previous chapter. Analytical work on the capacity of MIMO channels with spatial correlation at one end of the radio link will now be discussed. Upper and lower bounds based on chi-squared variates were derived in [31] for the ergodic capacity. In [67], Jensen's inequality was used to derive an upper bound on the capacity. An asymptotic analysis was proposed in [32] but this was only accurate if the number of transmit antennas is large. Asymptotic expressions were also presented in [68]. In [69], the exact density and distribution functions were derived for the capacity of systems with a few antennas but expressions for the ergodic capacity were not presented.

Analytical results for the capacity of MIMO channels with spatial correlation at both ends of the radio link were considered in [37, 70–73]. In [37], an asymptotic analysis was given which was valid if the number of transmit and receive antennas is large. Closed form expressions were derived in [70] which were asymptotic in the number of transmit antennas. Upper and lower bounds on ergodic capacity were presented in [71] and [72] respectively. Lower bounds for both the ergodic and outage capacity were derived in [73].

Analytical work on the capacity of MIMO channels is vast but in the literature discussed thus far, exact expressions for the ergodic capacity of spatially correlated MIMO channels were not derived. In this chapter exact analytical expressions are derived for the ergodic capacity of MIMO channels with spatial correlation at one end and at both ends of the radio link. The analysis is based on the transmitter and receiver antenna correlation matrices and can thus be applied to any spatially correlated MIMO channel.

After the completion of the work in this chapter, independent work was published in [74, 75] where exact analytical expressions were derived for the ergodic capacity of MIMO channels with correlation at one end of the radio link. These expressions contain a one-dimensional integral and are therefore different to the expressions derived here which contain a multi-dimensional integral. This chapter also considers exact analytical expressions for the case of spatial correlation at both ends of the radio link which has not been considered in the literature, as far as the author is aware.

This chapter is organised as follows. The spatially correlated MIMO channel model is presented in section 3.2. Analytical expressions are derived in section 3.3 for the ergodic capacity of MIMO channels with correlation at receiver only and with correlation at both the transmitter and receiver. In section 3.4, the accuracy of the analysis is assessed by comparing the analytical results with results obtained from simulation. The chapter is then summarised in section 3.5.

3.2 MIMO Channel Model

In this section the spatially correlated MIMO channel model is presented. This is a simplified version of the model proposed in the previous chapter where the temporal correlation is ignored and uniform linear arrays are used. The main details of the model are given here but the reader is referred to section 2.2 for more detail.

Consider a narrowband, single user communications system with n_T transmit and n_R receive omnidirectional antenna elements. It is assumed that the channel is known to the receiver and unknown to the transmitter which must equally divide the total transmit power over all antenna elements. The link between the transmit and receive antenna arrays is represented using the complex baseband vector notation

$$\underline{y} = \boldsymbol{H}\underline{x} + \underline{n}. \tag{3.1}$$

The $n_T \times 1$ transmit vector $\underline{x}$ has elements x_j which denote the signal transmitted from antenna $j = \{1, \ldots, n_T\}$. The $n_R \times 1$ receive vector $\underline{y}$ has elements y_i which denote the signal received on antenna $i = \{1, \ldots, n_R\}$. The $n_R \times 1$ noise vector $\underline{n}$ has elements n_i which denote the AWGN at receiver branch i. The entries of the noise vector are independent and identically distributed complex Gaussian random variables with variance N_0 where N_0 is the noise power spectral density. $\boldsymbol{H}$ is the $n_R \times n_T$ channel matrix of complex path gains h_{ij} between transmit antenna j and receive antenna i.

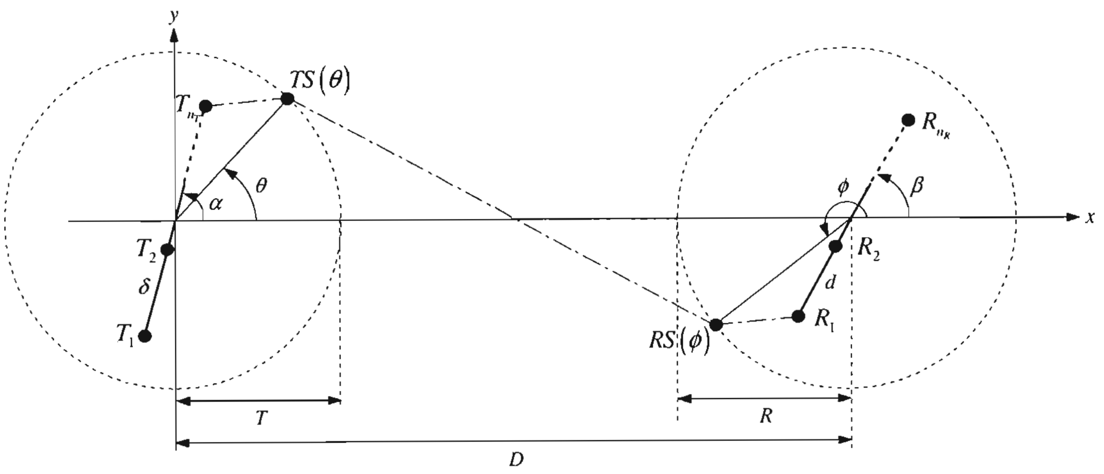

Figure 3.1: Geometric model for the spatially correlated MIMO channel.

Consider the scenario where both the transmitter and receiver are surrounded by objects resulting in local scattering at both ends of the radio link and that no line-of-sight exists between the transmitter and receiver. It is assumed that the channel is memoryless and for this reason there is no correlation between consecutive symbols.

In Fig. 3.1 a geometric model for the MIMO channel under consideration is presented. Uniform linear arrays are employed at both the transmitter and receiver. The transmit antenna array lies at an angle α from the x-axis with elements denoted by T_p spaced by δ. Similarly the receive antenna array lies at an angle β from the x-axis with elements R_m spaced by d. Both the transmitter and receiver are surrounded by omnidirectional scatterers which lie on a ring of radius T and R respectively. $TS(\theta)$ and $RS(\phi)$ denote arbitrary transmit and receive scatterers at angles θ and ϕ from the x-axis.

The correlation between arbitrary transmit antennas T_p and T_q is obtained by substituting $\alpha_{pq} = \alpha$ and $\mu_T = 0$ into (2.15) and is given by

$$\rho^T_{p,q} \approx \frac{1}{I_0(\kappa_T)} \cdot I_0\Big\{\big[\kappa_T^2 - b_{pq}^2 + 2\jmath\kappa_T b_{pq}\cos(\alpha)\big]^{1/2}\Big\}. \tag{3.2}$$

The correlation between arbitrary receive antennas R_m and R_n is obtained by substituting $\beta_{mn} = \beta$, $\tau = 0$ and $\mu_R = \pi$ into (2.16) as follows

$$\rho^R_{m,n} \approx \frac{1}{I_0(\kappa_R)} \cdot I_0\Big\{\big[\kappa_R^2 - c_{mn}^2 + 2\jmath\kappa_R c_{mn}\cos(\beta - \pi)\big]^{1/2}\Big\}. \tag{3.3}$$

Here $b_{pq} = 2\pi\delta(p-q)/\lambda$ and $c_{mn} = 2\pi d(m-n)/\lambda$. The parameters κ_T and κ_R control the degree of local scattering at the transmitter and receiver respectively. The function $I_0(\cdot)$ is the zeroth-order modified Bessel function of the 1st kind and $\jmath = \sqrt{-1}$.

3.3 Analytical Expressions for the Ergodic Capacity

Both the outage and the ergodic capacity have been used as capacity measures for MIMO channels, however the latter is mathematically less complicated to study analytically. The ergodic capacity measure is generally applied when the channel is memoryless, has no delay constraints and the transmission time is long enough to reveal the long term ergodic properties of the channel.

In this section analytical expressions are derived for the ergodic capacity of MIMO channels with spatial correlation at one end and at both ends of the radio link. This derivation is very general as it is based on the transmit and receive antenna correlation matrices. The simpler case of spatial correlation at one end of the radio link is considered first and the more complicated case of spatial correlation at both ends of the radio link is dealt with next. Throughout this analysis it is assumed that $n_T \geq n_R$ although the analysis can be easily modified to consider the case where $n_T < n_R$ [16].

The ergodic capacity of the MIMO channel described by the $n_R \times n_T$ random channel matrix $\boldsymbol{H}$ of complex path gains, is calculated as follows [16]

$$E[C] = E\left[\log_2 \det\left(\boldsymbol{I}_{n_R} + \frac{\rho}{n_T}\boldsymbol{H}\boldsymbol{H}^{\dagger}\right)\right] \tag{3.4}$$

where † is the transpose conjugate, $\det(\cdot)$ is the matrix determinant, $\boldsymbol{I}_{n_R}$ is the $n_R \times n_R$ identity matrix and ρ is the average SNR at each receive antenna. This can be rewritten in terms of the eigenvalues $\lambda_1, \ldots, \lambda_{n_R}$ of $\boldsymbol{A} = \boldsymbol{H}\boldsymbol{H}^{\dagger}$ such that

$$E[C] = E\left[\sum_{i=1}^{n_R} \log_2(1 + \frac{\rho}{n_T}\lambda_i)\right]. \tag{3.5}$$

Let $p(\underline{\lambda})$ denote the distribution of the eigenvalues of $\boldsymbol{A}$ where $\underline{\lambda} = [\lambda_1, \ldots, \lambda_{n_R}]$. The ergodic capacity can be calculated by integrating over $p(\underline{\lambda})$ and is given by

$$E[C] = \int_0^{\infty} \cdots \int_0^{\infty} \sum_{i=1}^{n_R} \log_2(1 + \frac{\rho}{n_T}\lambda_i) p(\underline{\lambda})\, d\underline{\lambda}. \tag{3.6}$$

Note that the limits of integration are 0 and ∞ as the eigenvalues of Hermitian matrix $\boldsymbol{A}$ are always non-negative real numbers. By integrating over the distribution of the eigenvalues of $\boldsymbol{A}$ as opposed to the distribution of $\boldsymbol{H}$ the order of integration is reduced from $2n_T n_R$ to n_R.

When $n_T \geq n_R$ the matrix $\boldsymbol{A}$ has a Wishart distribution with n_T degrees of freedom [76, 77]. However when $n_T < n_R$ $\boldsymbol{A}$ is singular and no distribution for $\boldsymbol{A}$ exists. The transmit antenna correlation matrix is denoted by $\boldsymbol{\Sigma}_T$ with elements $\rho^T_{p,q}$ (3.2) and the receive antenna correlation matrix is denoted by $\boldsymbol{\Sigma}_R$ with elements $\rho^R_{m,n}$ (3.3).

3.3.1 Spatial Correlation at the Receiver

The distribution of the eigenvalues of $\boldsymbol{A}$ is presented here for the case of spatial correlation at the receiver. This analysis can be easily modified to study spatial correlation at the transmitter by interchanging the subscripts T and R. Here $\boldsymbol{H}$ is zero mean and normally distributed with independent columns and covariance matrix $\boldsymbol{\Sigma}_R$.

In [77], the distribution of the ordered eigenvalues of the complex Wishart distributed matrix was given. By scaling this distribution by the factor $1/n_R!$ the distribution of the unordered eigenvalues of the complex Wishart distributed matrix $\boldsymbol{A}$ is given by

$$\begin{aligned} p(\underline{\lambda}) &= C_1 \cdot {}_0\tilde{F}_0(-\boldsymbol{\Sigma}_R^{-1}, \boldsymbol{\Lambda}) \cdot \prod_{i=1}^{n_R} \lambda_i^{n_T-n_R} \cdot \prod_{i<j}^{n_R} (\lambda_i - \lambda_j)^2 \qquad (3.7) \\ C_1 &= \frac{\pi^{n_R(n_R-1)}}{n_R! \tilde{\Gamma}_{n_R}(n_T) \tilde{\Gamma}_{n_R}(n_R)} \cdot \det(\boldsymbol{\Sigma}_R)^{-n_T} \\ \tilde{\Gamma}_m(n) &= \pi^{m(m-1)/2} \cdot \prod_{i=1}^{m} \Gamma(n-i+1) . \end{aligned}$$

Here ${}_0\tilde{F}_0(\cdot,\cdot)$ is the hypergeometric function of two matrix arguments, $\tilde{\Gamma}_m(n)$ is the complex multivariate gamma function, $\Gamma(\cdot)$ is the gamma function and $\boldsymbol{\Lambda} = \text{diag}(\lambda_1, \ldots, \lambda_{n_R})$. This expression would be straightforward to evaluate, if it were not for the hypergeometric function of matrix arguments which is generally expressed as a series expansion of zonal polynomials [76, 77]. However this formulation is not practical for numerical work as zonal polynomials are well known for being extremely difficult to compute and the series expansion is slow to converge. A more tractable formulation was proposed in [78] where the hypergeometric function of two matrix arguments was computed in terms of classical hypergeometric functions as follows

$$\begin{aligned}
{}_0\tilde{F}_0(\boldsymbol{S},\boldsymbol{T}) &= \frac{\det[{}_0F_0(s_it_j)]}{V(\boldsymbol{S})V(\boldsymbol{T})}\cdot\prod_{j=1}^{n}(j-1)! \qquad (3.8)\\
\det({}_0F_0(s_it_j)) &= \det\begin{pmatrix} {}_0F_0(s_1t_1) & \cdots & {}_0F_0(s_1t_n)\\ \vdots & \ddots & \vdots\\ {}_0F_0(s_nt_1) & \cdots & {}_0F_0(s_nt_n)\end{pmatrix}\\
V(\boldsymbol{S}) &= \prod_{i<j}^{n}(s_i-s_j)\\
V(\boldsymbol{T}) &= \prod_{i<j}^{n}(t_i-t_j)
\end{aligned}$$

where $\boldsymbol{S}$ and $\boldsymbol{T}$ are $n\times n$ Hermitian matrices with real eigenvalues $s_1,\ldots,s_n$ and $t_1,\ldots,t_n$ respectively. The function ${}_0F_0(x)=\exp(x)$ is the classical hypergeometric function. This formulation requires that the eigenvalues of the matrices $\boldsymbol{S}$ and $\boldsymbol{T}$ are unequal but this does not pose a problem as discussed later. By substituting (3.8) into (3.7), the distribution of the unordered eigenvalues of $\boldsymbol{A}$ can be written as

$$\begin{aligned}
p(\underline{\lambda}) &= C_2\cdot\det(\exp(\lambda_i\sigma_j))\cdot\prod_{i=1}^{n_R}\lambda_i^{n_T-n_R}\cdot\prod_{i<j}^{n_R}(\lambda_i-\lambda_j) \qquad (3.9)\\
C_2 &= \frac{\pi^{n_R(n_R-1)}}{n_R!\tilde{\Gamma}_{n_R}(n_T)\tilde{\Gamma}_{n_R}(n_R)V(-\boldsymbol{\Sigma}_R^{-1})}\cdot\det(\boldsymbol{\Sigma}_R)^{-n_T}\cdot\prod_{j=1}^{n_R}(j-1)!
\end{aligned}$$

where the σ_j's are the eigenvalues of $-\boldsymbol{\Sigma}_R^{-1}$. Note that the problem of equal eigenvalues of $\boldsymbol{\Lambda}$ is avoided because $V(\boldsymbol{\Lambda})$ is cancelled out by the 2nd product term of (3.7). Furthermore the eigenvalues of the correlation matrix $\boldsymbol{\Sigma}_R$ as well as its inverse are unequal for most practical cases. The ergodic capacity can now be calculated by substituting $p(\underline{\lambda})$ in (3.6) with (3.9) and evaluating the integral numerically.

3.3.2 Spatial Correlation at the Transmitter and Receiver

In this section the distribution of the eigenvalues of $\boldsymbol{A}$ is presented where spatial correlation at the transmitter and receiver is accounted for. In this case $\boldsymbol{H}$ is zero mean and normally distributed where $\boldsymbol{\Sigma}_T$ and $\boldsymbol{\Sigma}_R$ are the covariance matrices of the rows and columns respectively.

The distribution of $\boldsymbol{A}$ is a special case of the quadratic form of normal vectors and has been studied by a number of authors [79,80]. In [80], the distribution of the eigenvalues of the quadratic form of complex normal vectors was derived. The distribution of the unordered eigenvalues of $\boldsymbol{A}$ is obtained by setting the constant matrices in [80, Sec. 8] to identity matrices and scaling the distribution by $1/n_R!$. Hence $p(\underline{\lambda})$ is given by

$$\begin{aligned} p(\underline{\lambda}) &= C_3 \cdot {}_0\tilde{F}_0(\boldsymbol{\Sigma}_T^{-1}, \boldsymbol{\Lambda}, -\boldsymbol{\Sigma}_R^{-1}) \cdot \prod_{i=1}^{n_R} \lambda_i^{n_T-n_R} \cdot \prod_{i<j}^{n_R} (\lambda_i - \lambda_j)^2 \qquad (3.10) \\ C_3 &= \frac{\pi^{n_R(n_R-1)}}{n_R!\tilde{\Gamma}_{n_R}(n_T)\tilde{\Gamma}_{n_R}(n_R)} \cdot \det(\boldsymbol{\Sigma}_T)^{-n_R} \cdot \det(\boldsymbol{\Sigma}_R)^{-n_T} \end{aligned}$$

where ${}_0\tilde{F}_0(\cdot,\cdot,\cdot)$ is the hypergeometric function of three matrix arguments. This function can be evaluated using a series expansion of zonal polynomials but as discussed previously, this formulation is not practical for numerical work. As far as the author is aware, no practical formulation for this function exists which can be evaluated numerically with realisable complexity.

3.4 Analytical Results

In this section the analysis in section 3.3 for the ergodic capacity of MIMO channels with spatial correlation at the receiver is compared to simulation results.

The following method is used to generate spatially correlated variates with receive antenna correlation matrix $\boldsymbol{\Sigma}_{\boldsymbol{R}}$. For each time instance a $n_R \times n_T$ matrix $\boldsymbol{U}$ of independent zero mean complex Guassian random variables with unit variance is generated. The channel matrix $\boldsymbol{H}$ with the desired spatial correlation is generated as follows

$$\boldsymbol{H} = \sqrt{\boldsymbol{\Sigma}_{\boldsymbol{R}}}\boldsymbol{U}. \qquad (3.11)$$

The calculation of matrix square root of $\boldsymbol{\Sigma}_{\boldsymbol{R}}$ is discussed in section 2.3.

In all cases the ergodic capacity $E[C]$ is used as the capacity measure. The simulation results are generated using Monte-Carlo methods where many instances of the channel $\boldsymbol{H}$ are generated according to (3.11) and the ergodic capacity is calculated using (3.4). The analytical expression (3.6) with (3.9) substituted for $p(\underline{\lambda})$ is evaluated numerically using a multi-dimensional adaptive step size integration technique with limits of integration of 0 and 100 for each dimension.

Let n describe a MIMO system with equal transmit and receive antennas i.e. $n = n_T = n_R$. Unless indicated otherwise, the following parameters are used. The SNR is set to 10 dB. The receiver antenna spacing is $d = \lambda$ and the antenna array angle is $\beta = 45°$. The degree of local scattering at the receiver is $\kappa_R = 10$. The carrier frequency is set to 1 GHz which corresponds to a carrier wavelength λ of 0.3 m.

In Fig. 3.2 and Fig. 3.3 the distribution of the eigenvalues $p(\lambda_1, \lambda_2)$ of $\boldsymbol{A}$ is given for a $n = 2$ system for $d = \lambda$ and $d = 0.1\lambda$ respectively. When $d = \lambda$, the two peaks are small and spread out while for a smaller spacing of $d = 0.1\lambda$, the peaks are higher and sharper due to the increase in spatial correlation. Therefore as the spatial correlation increases the probability of small eigenvalues becomes greater which results in a decrease in capacity. These sharp peaks increase the computational complexity of the numerical integration as a smaller step size is required to obtain accurate results. Thus for large dimension systems with high spatial correlation, it is not computationally feasible to obtain analytical results using this analysis.

The analytical results are compared to simulation results for the $n = 2$ and $n = 3$ systems in Fig. 3.4 to Fig. 3.6. In all cases it is shown that the analysis agrees well with the simulation results. In Fig. 3.4 a reduction in antenna spacing results in a decrease in capacity as there is a higher degree of correlation between antenna elements. The influence of the receiver array angle is investigated in Fig. 3.5. It is noted that the capacity is at a minimum when the array is parallel to the direction of the wavefront ($\beta = 0°$) and at a maximum when the array is perpendicular to the direction of the wavefront ($\beta = 90°$). The effect of non-isotropic scattering on capacity is considered in Fig. 3.6. As the scattering becomes more non-isotropic, corresponding to an increase in κ_R, the capacity decreases as the wavefront arriving at the antenna array is now more correlated.

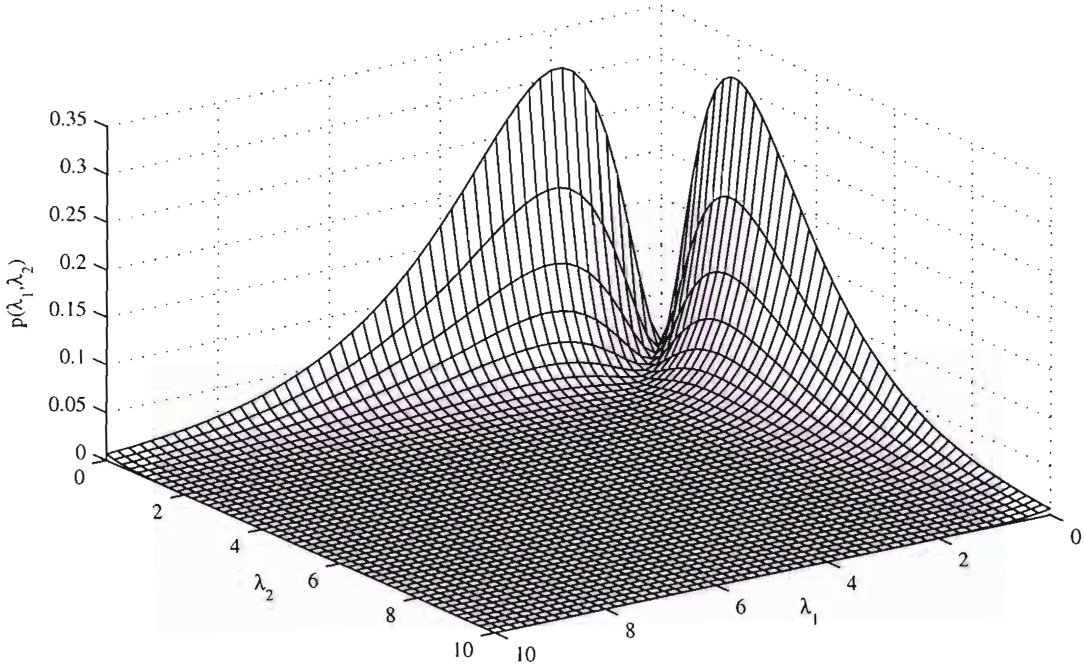

Figure 3.2: Distribution of the eigenvalues of $\boldsymbol{A}$ for $d = \lambda$

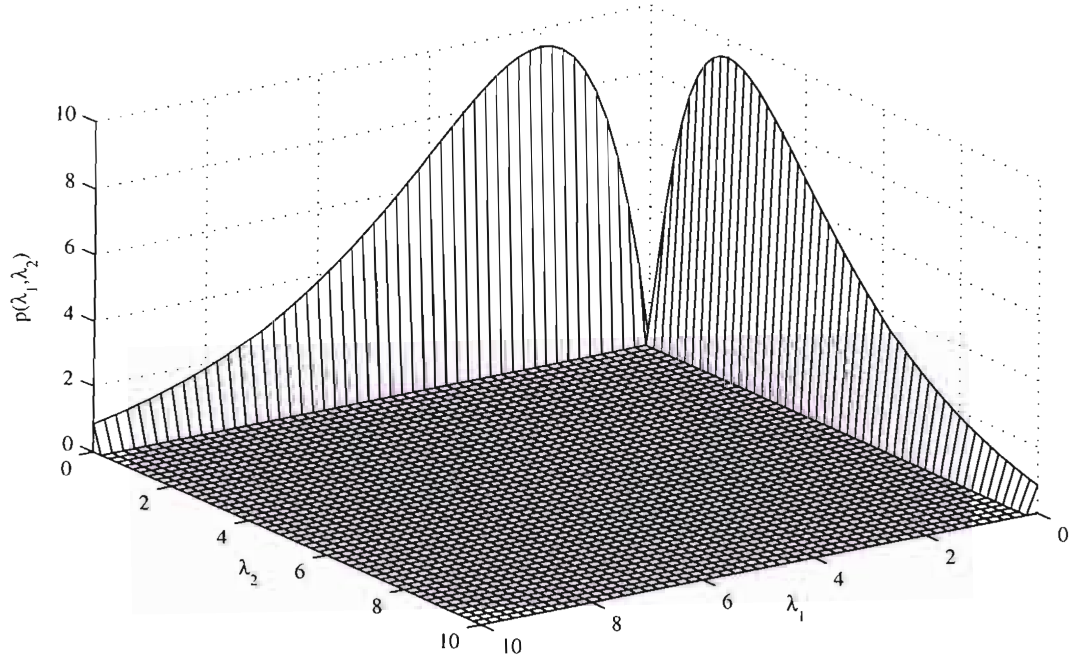

Figure 3.3: Distribution of the eigenvalues of $\boldsymbol{A}$ for $d = 0.1\lambda$

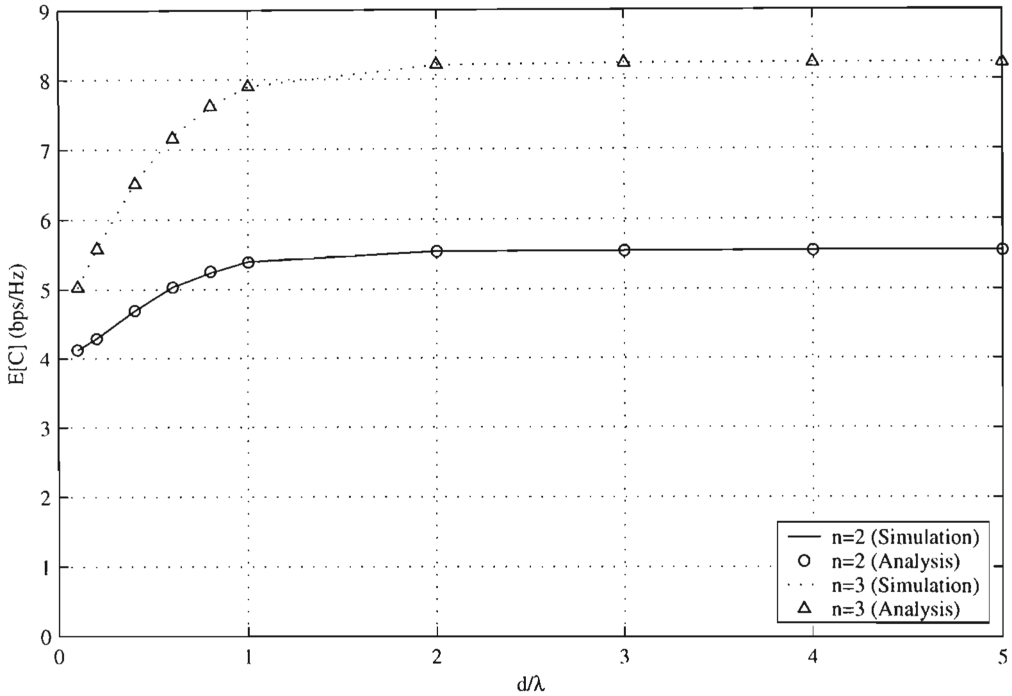

Figure 3.4: Analytical results for the ergodic capacity of a n transmit, n receive antenna system with varying receiver antenna spacings d.

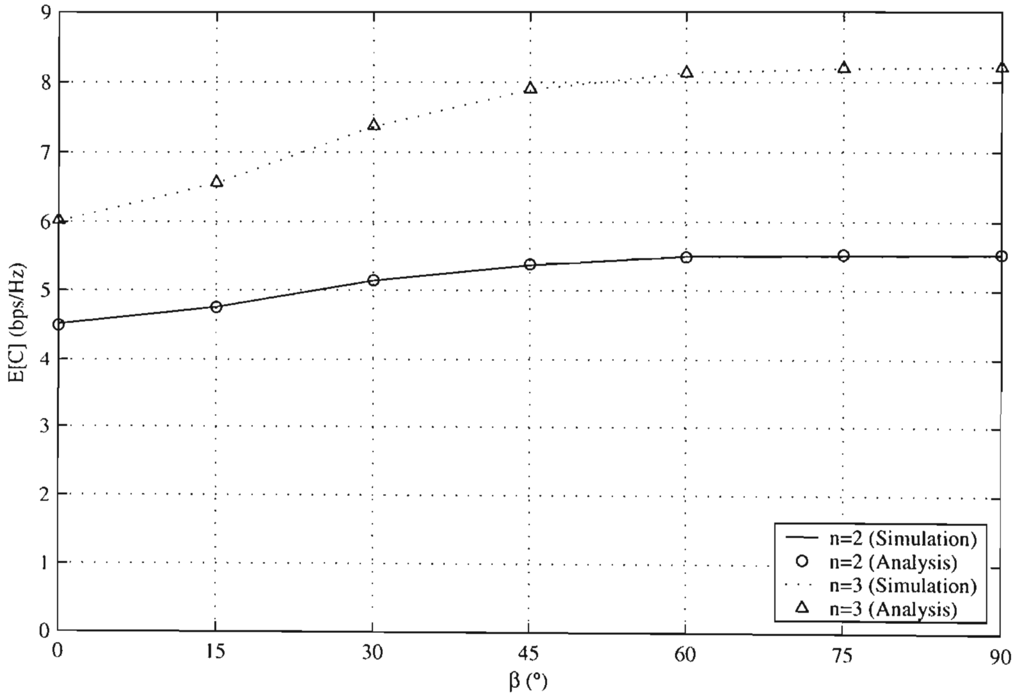

Figure 3.5: Analytical results for the ergodic capacity of a n transmit, n receive antenna system with varying receiver array angles β.

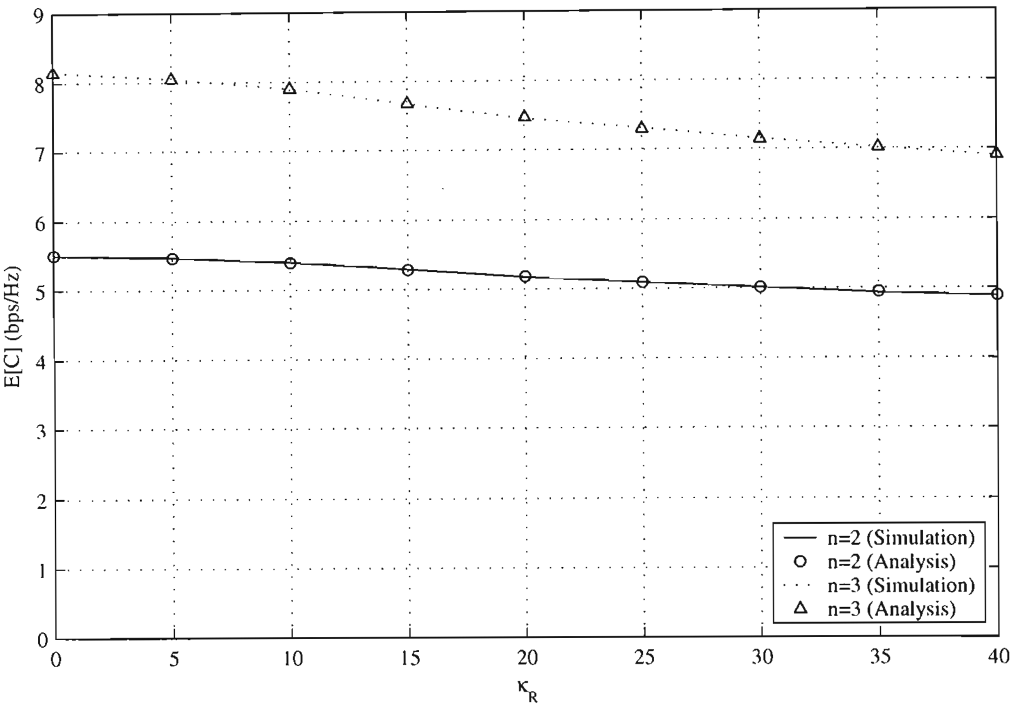

Figure 3.6: Analytical results for the ergodic capacity of a n transmit, n receive antenna system with varying degrees of non-isotropic scattering κ_R at the receiver.

3.5 Summary

Analytical expressions were derived for the ergodic capacity of spatially correlated MIMO channels. For the case of spatial correlation at the receiver, the analytical expression was evaluated using multi-dimensional numerical integration. The analysis agreed well with simulation results for a range of channel parameters for both the $n = 2$ and $n = 3$ systems. For the case of spatial correlation at the transmitter and receiver, the derived analytical expression contained a hypergeometric function of 3 matrix arguments which could not be evaluated numerically with realisable complexity. The proposed analysis is useful as it is based on the transmitter and receiver antenna correlation matrices and can thus be applied to any spatially correlated MIMO channel.

Chapter 4

Non-Binary LDPC Codes

4.1 Introduction

Low-density parity-check (LDPC) codes have recently been rediscovered and are currently considered a serious competitor to turbo codes due to their near Shannon limit performance. Initially binary LDPC codes were considered but more recently non-binary LDPC codes have shown promising results. Optimising the structure of these codes is critical to their performance and methods such as density evolution or extrinsic information transfer (EXIT) charts have been applied to the design of binary LDPC codes. Efficient methods used to optimise the design of non-binary LDPC codes are not well developed. The main focus of this chapter is on the application of EXIT charts to the optimisation of non-binary LDPC codes for the AWGN channel.

An overview of the literature on binary and non-binary LDPC codes is presented in section 4.2, as well as the various methods employed to optimise the design of these codes. The proposed EXIT chart approach for the optimisation of non-binary LDPC codes, is discussed at the end of this section. The encoding, construction and decoding of non-binary LDPC codes are described in detail in section 4.3, 4.4 and 4.5 respectively. A complete description of the non-binary LDPC decoder, that uses the log domain Fourier transform decoding algorithm, is presented here which has not been fully described in the literature. In section 4.6, EXIT charts are proposed to optimise non-binary LDPC codes for the AWGN channel. The *a priori* information of the LDPC decoder is accurately modelled using a Gaussian mixture distribution. Analytical expressions are given for the EXIT curves of the variable and check node decoders, for both regular and irregular LDPC codes. These are shown to agree well with simulation results. It is then described how the LDPC codes can be optimised by matching the EXIT curves of the variable and check node decoders. Simulation results for the optimised codes are presented in section 4.7 and the chapter is summarised in section 4.8

4.2 LDPC Codes

This section provides a brief overview of binary and non-binary LDPC codes as well as the various techniques utilised to optimise the design of these codes.

4.2.1 Binary LDPC Codes

LDPC codes were originally proposed by Gallager [10,81] in 1962 and had the computing power been available at that time, these codes would have outperformed the best known codes prior to the invention of turbo codes [9] in 1993. However Gallager's codes remained largely forgotten until they were rediscovered by MacKay [11,82] in 1996. A few authors did consider LDPC codes prior to 1996 and the more significant contributions include [83–85]. Gallager's codes were defined by a sparse parity check matrix $\boldsymbol{H}$ with uniform row and column weights[1] and are generally referred to as regular LDPC codes in the literature.

Irregular LDPC codes have non-uniform row and column weights and were originally proposed in [86, 87] where they were shown to outperform regular LDPC codes. In [88, 89], optimal irregular LDPC codes were designed using density evolution. These codes have achieved excellent performance where a rate 1/2 code of length 10^6 bits achieved a BER of 10^{-6} at a SNR of 0.31 dB which is 0.13 dB away from the Shannon

---

[1] The number of ones in a row (column) of $\boldsymbol{H}$ is referred to as the row (column) weight of $\boldsymbol{H}$.

limit of a binary input AWGN channel. These results were improved in [90] where a rate 1/2 code of length 10^7 bits achieved a BER of 10^{-6} within 0.04 dB of the Shannon limit. In [91], irregular LDPC codes were optimised for the Rayleigh fading channel using density evolution.

Another class of LDPC codes is known as generalised LDPC codes where each parity check is replaced by a small linear block code. Generalised LDPC codes were independently proposed in [92] and [93] where good performance, comparable to LDPC codes and turbo codes, was achieved in the AWGN channel.

Turbo codes [9] proposed by Berrou *et al.* in 1993 are another class of powerful error correcting codes. In [89], it was shown that for frame lengths, greater than 10 000 bits, irregular LDPC codes outperform turbo codes. In addition to superior performance, LDPC codes have a number of other advantages over turbo codes: the minimum distance increases linearly with code length; an error floor is not usually observed as is the case with turbo codes; the decoding algorithm is highly parallelisable; can be decoded using many different decoding algorithms with different performance/complexity tradeoffs; decoding is a verifiable event i.e. one can check if the decoded codeword is correct; have a built in stopping criteria; simple to design codes with arbitrary rates. For these reasons LDPC codes are seen as a good alternative to turbo codes and a promising coding technique for future communication systems.

4.2.2 Non-Binary LDPC Codes

Binary LDPC codes, discussed in the previous section, are defined over the finite field $GF(2)$. Non-binary LDPC codes are a generalisation of binary LDPC codes to higher order fields $GF(q = 2^p)$. These codes were originally proposed by Davey and MacKay in 1998 [94, 95] and are comprehensively treated in [96].

Regular and irregular non-binary LDPC codes were optimised for the AWGN channel in [96] where it was shown that for the same optimisation algorithm, optimised non-binary LDPC codes outperform binary LDPC codes. Non-binary LDPC codes may also be useful for improving the performance of short frame length LDPC codes where turbo codes still achieve superior performance. Non-binary LDPC codes have been applied to magnetic recording channels [97] and MIMO channels [98].

In [11], it was proven that LDPC codes can approach Shannon limit performance if the column weight of $\boldsymbol{H}$ is made sufficiently high and an optimal decoder is used. However, as the column weight increases, the number of cycles in the corresponding bipartite graph also increases which degrades the performance of the iterative decoding algorithm. With non-binary LDPC codes, one can increase the mean column weight but still retain the same bipartite graph. In this way, the complexity of the LDPC code is increased while the decoder performance is not degraded. Therefore, by encoding over $GF(q)$ each parity check becomes more complex while the decoding remains tractable. Increasing the field size of a LDPC code is comparable to increasing the constraint length of convolutional codes. The disadvantage of non-binary LDPC codes is that the decoding complexity is greater than that for binary LDPC codes which will be discussed later in this chapter.

4.2.3 Optimisation of Binary LDPC Codes

With irregular LDPC codes, the set of column weights as well as the fraction of columns of a particular weight is referred to as the column profile. The row profile is similarly defined. The performance of irregular LDPC codes is strongly influenced by the choice of the row and column profile. To this end, it is important to select the optimal profile to ensure that the code achieves good performance. The most rudimentary way to achieve this would be to select a profile and run a BER simulation to assess the performance of the corresponding code. An optimisation algorithm could then be used to permute this profile in such a way that the code achieving the lowest BER, for the SNR range of interest, is found. This process is very time consuming and for this reason a number of more efficient approaches have been proposed to facilitate searches for optimal LDPC profiles.

Density Evolution

As the frame length of a LDPC code tends to infinity a threshold phenomenon is observed whereby very low BERs can be achieved if the SNR is greater than some threshold. On the other hand, for SNRs below this threshold it becomes very difficult to achieve low BERs. The threshold region of a code is equivalent to the waterfall region in the BER plot of the code performance where a sharp increase in the gradient of the curve is observed and the BER decreases rapidly over a small range of SNRs.

The threshold phenomenon was first observed by Gallager [81] and was initially used to optimise irregular LDPC codes in [86, 87] on the binary-symmetric channel using hard decision decoding.

This concept was generalised in [88] to a range of binary-input channels including the AWGN channel using message-passing decoding. In this paper it was proven that as the frame length tends to infinity: almost all instances of a LDPC code behave the same (concentration theorem); the average behaviour is equal to the behaviour of cycle free graphs; a threshold phenomenon is observed which clearly separates the regions of reliable and unreliable transmission. An algorithm known as density evolution was proposed which is an exact numerical technique used to track the evolution of the message densities as they are iteratively exchanged between the variable and check node decoders. Using this algorithm, the SNR at which the threshold of a particular profile occurs could be determined. Density evolution was then applied in [89] to search for optimal irregular LDPC codes.

Tracking the message densities using density evolution is a computationally intensive task and it is difficult to extend this to more complex channels. To simplify density evolution the message densities were approximated using a Gaussian distribution in [99]. It was shown that the message densities could be reasonably described by their mean, and in this way, only the mean of the message densities needs to be tracked as opposed to the message densities themselves.

EXIT Charts

Extrinsic information transfer (EXIT) charts were introduced in [100] where they were used to optimise an iterative demapping and decoding scheme. They were later applied in [101] to select the optimal constituent codes for a parallel concatenated convolutional code. EXIT charts are based on the mutual information measure and describe the exchange of extrinsic information between the constituent decoders. By plotting the EXIT curves of the constituent decoders on the same set of axes the convergence behaviour of the concatenated system can be determined without the need to run lengthly BER simulations for the entire system. In order to calculate the EXIT curves of the constituent decoders, the *a priori* information is modelled using a Gaussian distribution as described in [101].

Mutual information is not the only measure which can be used to describe the distribution of the *a priori* or *a posteriori* information. In [101], various SNR measures, based on the mean, variance and BER as well as the mutual information measure, were compared. It was shown here, that the mutual information measure describes the decoder behaviour the most accurately. The convergence prediction of six different measures were compared in [102] for turbo coding, turbo equalisation and turbo bit-interleaved coded modulation. Again, it was shown that the mutual information measure is the most accurate.

EXIT charts were used to analyse LDPC codes in [103] for a binary erasure channel. A number of important properties were proven here and it was shown that optimal LDPC codes can be designed by matching the variable and check node EXIT curves. This approach was applied in [104] to design optimal LDPC codes for the AWGN and MIMO channels where the optimised codes achieved near capacity performance. The approach was also applied to the optimisation of repeat-accumulate codes for MIMO systems in [105] and a number of serially concatenated systems in [106].

4.2.4 Optimisation of Non-Binary LDPC Codes

The optimisation of binary LDPC codes has been well treated in the literature and techniques such as density evolution or EXIT charts, described previously, can be used to find the optimal row and column profiles. The optimisation of non-binary LDPC codes has only been considered by Davey in his thesis work [96] where two techniques were proposed. These techniques are now briefly discussed as well as the proposed technique using EXIT charts.

Davey's Methods

In [96], two methods were considered to optimise the row and column profiles of non-binary LDPC codes, namely, the Monte-Carlo cost function and the empirical cost function.

The Monte-Carlo cost function simulates an infinite code which corresponds to the cycle free case in the bipartite graph. Initially a random ensemble of messages is generated according to the channel model. This ensemble is iteratively updated by simulating a code fragment for each group of messages from the ensemble. The average bit entropy after a fixed number of iterations is then used to rate the effectiveness of the chosen profile. This method worked well for regular codes but not for irregular codes.

The empirical cost function uses the average number of decoding iterations required to decode a particular code in order to rate the effectiveness of a chosen profile. This method was used to optimise irregular, non-binary LDPC codes for the AWGN channel where good results were achieved. Although this method is simple, it is computationally intensive as for each profile a new parity check matrix must be generated and many frames must be decoded to obtain a sufficient average for the number of decoding iterations. Therefore, for the optimisation of long codes with complex profiles, this method is not practical.

Proposed Method based on EXIT Charts

The optimisation methods proposed by Davey are either not effective for irregular codes or have high computational complexity.

EXIT charts have been applied to the optimisation of binary LDPC codes in both the AWGN and MIMO channels [104]. The optimised codes achieved near capacity performance and the design method, based on matching the variable and check node EXIT curves, is very efficient. Density evolution can also be used to optimise LDPC codes for a range of channels but is computationally intensive and difficult to apply to more complex channels. EXIT charts model the *a priori* information using a Gaussian distribution and for this reason density evolution may lead to LDPC codes with superior performance.

In this chapter the EXIT chart approach [104] is extended to the optimisation non-binary LDPC codes for the AWGN channel as this method is more efficient than density evolution and can be extended to more complex systems. To the extent of the author's knowledge EXIT charts have not been considered for the analysis or optimisation of non-binary LDPC codes.

4.3 LDPC Encoding

LDPC codes are linear block codes which are defined by a very sparse parity check matrix $\boldsymbol{H}$ with dimensions $m \times n$. With binary LDPC codes the elements of $\boldsymbol{H}$ are defined over the finite field $GF(2)$ while with non-binary LDPC codes the elements are defined over $GF(q = 2^p)$. It is important to note that $GF(4)$ and $GF(2^2)$ are not the same finite fields. Finite fields are described appendix B where lookup tables are given for $GF(2^2)$ and $GF(2^3)$. In the sequel the notation $GF(q)$ is used to denote the finite field $GF(2^p)$.

The parity check matrix is generated as in the binary case but each non-zero element can take on $q - 1$ possible values. Initially $\boldsymbol{H}$ is not in systematic form and is reduced to the form

$$\boldsymbol{H} = [\boldsymbol{P}|\boldsymbol{I}_m] \tag{4.1}$$

using Gaussian elimination where $\boldsymbol{I}_m$ is the $m \times m$ identity matrix and $\boldsymbol{P}$ has dimensions $m \times k$ where $k = n - m$. All arithmetic operations are implemented over the finite field $GF(q)$. The $k \times n$ generator matrix can now be expressed as

$$\boldsymbol{G} = [\boldsymbol{I}_k|\boldsymbol{P}'] \tag{4.2}$$

where $'$ denotes the matrix transpose.

The encoding of non-binary LDPC codes is similar to the encoding of binary LDPC codes. A block diagram of the LDPC encoder is shown in Fig. 4.1 where B/S and S/B denote bit-to-symbol and symbol-to-bit conversions respectively. The input frame $\underline{u}$ consisting of K information bits is converted to a frame $\underline{v}$ of length $k = K/p$ symbols from $GF(q)$. This frame is then encoded to give codeword $\underline{w}$ of length n symbols as follows

$$\underline{w} = \boldsymbol{G}\underline{v} \tag{4.3}$$

where the matrix multiplication is performed over the finite field $GF(q)$. The rate of the encoder is $R = k/n$. The codeword $\underline{w}$ is then converted to a binary codeword $\underline{c}$ of length of $N = np$ bits.

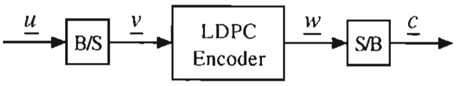

Figure 4.1: Block diagram of the non-binary LDPC encoder.

The encoded bits $\underline{c}$ are then modulated to give BPSK symbols $s_t = 2c_t - 1$ where $t = \{1, \ldots, N\}$ and are then transmitted over the AWGN channel. The received signal after matched filtering is expressed as

$$r_t = s_t + \eta_t. \tag{4.4}$$

Here η_t is the AWGN noise which is modelled as an independent, zero-mean Gaussian random sequence with variance

$$\sigma_n^2 = \frac{1}{2RE_b/N_0} \tag{4.5}$$

where E_b/N_0 is the signal-to-noise ratio. The LDPC decoder then calculates the most likely estimate $\underline{\hat{u}}$ of the original information bits $\underline{u}$ given the received signal $\underline{r}$.

4.4 Code Construction

LDPC codes can be represented using a bipartite graph which consists of n variable nodes on the left corresponding to the transmitted codeword and m check nodes on the right corresponding to the parity checks. A connection or edge exists between variable node j and check node i if the corresponding entry H_{ij} in the parity check matrix $\boldsymbol{H}$ is non-zero. The number of edges connected to variable node j is referred to as the variable node degree which is equal to the weight of column j in $\boldsymbol{H}$. Similarly, the number of edges connected to check node i is referred to as the check node degree which is equal to the weight of row i in $\boldsymbol{H}$. The weight of a row or column is defined as the number of non-zero entries in that row or column.

With regular LDPC codes, all variable nodes have degree d_v and all check nodes have degree d_c. The notation (d_v, d_c) is used to describe a regular LDPC code. With irregular LDPC codes the variable and check node degrees are chosen according to some profile. The variable node profile $\underline{\lambda}$ has elements λ_i which gives the fraction of variable nodes of degree i. Similarly the check node profile $\underline{\rho}$ has elements ρ_i which gives the fraction of check nodes of degree i. For example $\lambda_3 = 1$ and $\rho_6 = 1$ describes a regular LDPC code where all variable nodes have degree 3 and all check nodes have degree 6. Note that in the literature on LDPC codes it is common to define λ_i and ρ_i in terms of fractions of edges in the bipartite graph whereas in this thesis they are defined in terms of fractions of nodes as was the case in [96].

Given $\underline{\lambda}$ and $\underline{\rho}$ one can construct $\boldsymbol{H}$ such that the row and column weights have the desired profile. In order to ensure that the LDPC codes achieve good performance, the parity check matrix $\boldsymbol{H}$ must be carefully constructed so that short cycles are avoided. Cycles in the bipartite graph degrade the performance of the iterative decoding algorithm. Various constructions of LDPC codes were discussed and compared in [11, 107].

In [96], the UL-A and UL-B methods were proposed to systematically construct the columns of weight 2 but the performance of the LDPC codes constructed in this manner were not compared. Using the $GF(4)$ code of [96, Appendix F.3] as given in Table 4.1, the performance of the UL-A and UL-B construction methods are compared in Fig. 4.2 for frames of length of N = 12 000 and N = 60 000 bits. The log-FFT decoding algorithm described in section 4.5 is used and the number of decoding iterations is 100. It is observed that the UL-A method gives superior performance for both frame lengths.

Throughout this thesis the LDPC codes are constructed as follows. The 1st m columns of weight 2 of the parity check matrix, corresponding to variable nodes of degree 2, are

Table 4.1: Profiles for the $GF(4)$ code of [96] with $R = 1/2$.

Variable nodes	$\lambda_2 = 0.478633,\ \lambda_3 = 0.4085,\ \lambda_8 = 0.000067$ $\lambda_{11} = 0.045233,\ \lambda_{17} = 0.067567$
Check nodes	$\rho_7 = 0.341,\ \rho_8 = 0.659$

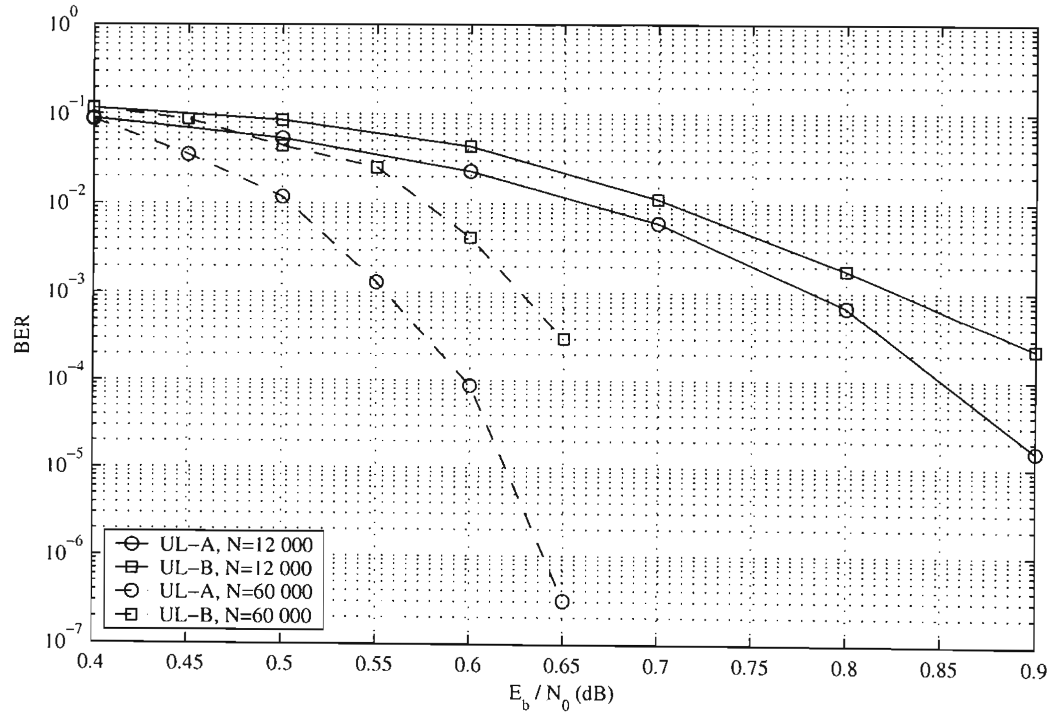

Figure 4.2: Comparison of the UL-A and UL-B construction methods.

constructed using the UL-A method. The remaining weight 2 columns and the columns of weight 3 to 5 are constructed such that the overlap between these columns as well as the weight 2 columns is at most 1 which ensures that cycles of length 4 or less are avoided. The column overlap is the number of non-zero elements in the same position in two different columns. No restrictions are placed on columns of weight greater than 5. For each new column it must be ensured that the row weight is not exceeded. The non-zero entries are uniformly distributed in $GF(q)$.

The UL-A method, used to construct the 1st m weight 2 columns, is now described. The 1st $m/2$ columns are constructed by stacking two $m/2 \times m/2$ identity matrices on top of each other, as shown in Fig. 4.3. The next $m/4$ columns are constructed by stacking two $m/4 \times m/4$ identity matrices beside the previous one. This process is repeated where the size of the identity matrix is halved each time until a maximum of m weight 2 columns are constructed. Care must taken not to exceed the row weight of the parity check matrix.

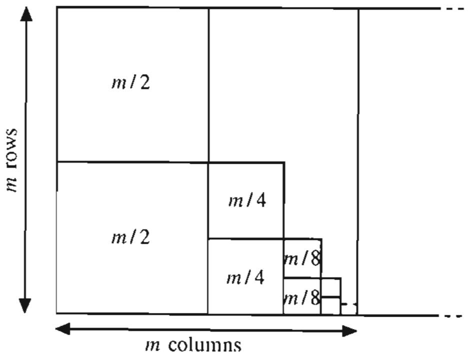

Figure 4.3: Illustration of the UL-A construction method. The number in each block denotes the size of the identity matrix.

4.5 LDPC Decoding

The LDPC decoder attempts to find the most likely codeword $\underline{\hat{w}}$ such that $\boldsymbol{H}\underline{\hat{w}} = 0$ given the received information. The decoding of non-binary LDPC codes is not equivalent to the decoding of binary LDPC codes as the non-binary decoder operates on the symbol level, not on the bit level. Non-binary LDPC codes can be decoded using the sum product algorithm together with the forward-backward algorithm [95] with a computational complexity of $O(nq^2)$. Fourier transform decoding [96] reduces the complexity to $O(nqp)$ but implementing this algorithm in the probability domain has a number of draw backs. Many multiplications are required which are costly to implement in hardware and may lead to numerical instability after many iterations. These problems are avoided by implementing the algorithm in the log domain. This idea was introduced in [97] but a complete description of the algorithm was not given. The probability and log domain versions of the Fourier transform decoding algorithm will be referred to as the FFT and log-FFT decoding algorithms throughout this thesis.

In this section the log-FFT decoding algorithm is described in detail where some minor modifications on the algorithm proposed in [97] are introduced. The computational complexity of the FFT and log-FFT algorithms is then compared.

4.5.1 Overview

It is simplest to explain the decoding of LDPC codes in terms of a bipartite graph which was described in the previous section and is illustrated in Fig. 4.4. The decoder operates by exchanging messages between connected nodes in an iterative fashion until a valid codeword is found.

These messages are represented as log-likelihood ratios (LLRs) where the LLR that $w_j = a$ where $a \in GF(q)$ is defined as

$$\log \frac{P(w_j = a)}{P(w_j = 0)}. \tag{4.6}$$

The channel messages F_j^a represent the prior LLR that $w_j = a$ according to the channel model. The variable node messages Q_{ij}^a represent the LLR that $w_j = a$ given the information obtained from all connected check nodes except i as well as the channel message F_j^a. The check node messages R_{ij}^a represent the LLR of check i being satisfied if $w_j = a$ taking into account information received from all connected variable nodes except j.

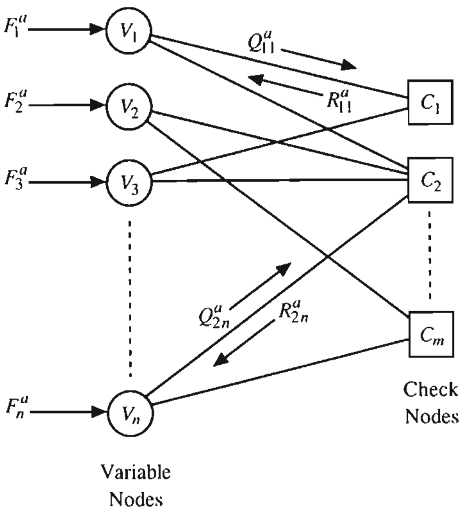

Figure 4.4: Bipartite graph illustrating the exchange of messages between variable and check nodes.

The algorithm is initialised by calculating the channel messages F_j^a and setting each check node message R_{ij}^a to zero. Each variable node j then sends the message Q_{ij}^a to all connected check nodes i. Each check node i sends the message R_{ij}^a to all connected variable nodes j. A tentative decision is then made and if this decision satisfies the parity constraints the decoding is terminated. Otherwise the variable and check node messages are iteratively updated until a valid codeword is found or the maximum number of iterations is reached.

In the following description only messages of connected nodes i, j are updated which correspond to non-zero entries H_{ij} in the parity check matrix. In all cases $i = \{1, \ldots, m\}$, $j = \{1, \ldots, n\}$, and $a \in GF(q)$.

4.5.2 Initialisation

The algorithm is initialised by calculating the channel messages F_j^a and setting the check node messages to zero as follows

$$\begin{aligned} F_j^a &= \log \frac{P(w_j = a | r_j^1, \ldots, r_j^p)}{P(w_j = 0 | r_j^1, \ldots, r_j^p)} = \sum_{l:\ a_l = 1} 2r_j^l / \sigma_n^2 & (4.7) \\ R_{ij}^a &= 0. & (4.8) \end{aligned}$$

Here $r_j^l = r_{jp+l}$ is the lth received bit corresponding to symbol j of $\underline{w}$ and a_l is the lth bit in the binary representation of a.

4.5.3 Update Variable Node Messages

The variable node messages are updated by

$$Q_{ij}^a = F_j^a + \sum_{k \in M_{j,!i}} R_{kj}^a - \alpha_{ij} \tag{4.9}$$

$$\alpha_{ij} = \max_a Q_{ij}^a \tag{4.10}$$

where $M_{j,!i}$ is the set of all check nodes connected to variable node j excluding check node i. Therefore check node i does not receive information sent to variable node j on the previous iteration which ensures that only extrinsic information is exchanged between nodes. To avoid numerical overflow problems the normalisation constant α_{ij} is introduced.

4.5.4 Update Check Node Messages

As discussed in [96] it is more efficient to update the check node messages in the Fourier domain. The fast Fourier transform (FFT) is used to transform the messages into the Fourier domain. The FFT is not a q-point FFT but a p-dimensional two-point FFT and is described in detail in section 4.5.6. In the probability domain the FFT involves both addition and subtraction operations which may result in negative numbers. In order to handle negative numbers in the log domain a sign dimension is included such that

$$\bar{x} = [\bar{x}(s), \bar{x}(m)] = [\text{sgn}(x), \log|x|] \tag{4.11}$$

where x denotes numbers in the probability domain and $\bar{x}$ denotes numbers in the signed log domain.

The incoming variable node messages Q_{ij}^a are converted to signed LLRs where $\bar{Q}_{ij}^a(m) = Q_{ij}^a$ and $\bar{Q}_{ij}^a(s) = 1$. These are then permuted and transformed to the Fourier domain such that

$$\underline{\tilde{Q}}_{ij} = \mathcal{F}\left[\mathcal{P}_{ij}\left(\underline{\bar{Q}}_{ij}\right)\right]. \tag{4.12}$$

Here $\underline{\bar{Q}}_{ij} = [\bar{Q}^0_{ij}, \ldots, \bar{Q}^{q-1}_{ij}]$, $\mathcal{F}(\underline{x})$ is the FFT of $\underline{x}$ and $\mathcal{P}_{ij}(\underline{x})$ is the permutation of $\underline{x}$ by H_{ij}. The elements of $\underline{x}$ are permuted by moving the ath element of $\underline{x}$ to position aH_{ij} where the multiplication is performed over $GF(q)$.

The Fourier domain check node messages are updated as follows

$$\begin{aligned} \tilde{R}^a_{ij}(s) &= \prod_{k \in N_{i,!j}} \tilde{Q}^a_{ik}(s) & (4.13) \\ \tilde{R}^a_{ij}(m) &= \sum_{k \in N_{i,!j}} \tilde{Q}^a_{ik}(m) & (4.14) \end{aligned}$$

where $N_{i,!j}$ is the set of all variable nodes connected to check node i excluding variable node j which ensures only extrinsic information is exchanged between nodes.

The Fourier domain check node messages are transformed back to the signed log domain by an inverse FFT and inverse permutation which is given by

$$\underline{\bar{R}}_{ij} = \mathcal{P}^{-1}_{ij}\left[\mathcal{F}^{-1}\left(\underline{\tilde{R}}_{ij}\right)\right] \tag{4.15}$$

where $\mathcal{F}^{-1}(\underline{x})$ is the inverse FFT of $\underline{x}$ and $\mathcal{P}^{-1}_{ij}(\underline{x})$ is the inverse permutation of $\underline{x}$ by H_{ij}. The signed LLRs $\bar{R}^a_{ij}$ are then converted to check node messages where $R^a_{ij} = \bar{R}^a_{ij}(m)$.

4.5.5 Tentative Decoding

A tentative decision $\underline{\hat{w}}$ on the original codeword $\underline{w}$ is given by

$$\hat{w}_j = \underset{a}{\operatorname{argmax}} \; F^a_j + \sum_{k \in M_j} R^a_{kj} \tag{4.16}$$

where M_j is the set of all check nodes connected to variable node j. If $\boldsymbol{H}\underline{\hat{w}} = 0$ then the decoding is terminated as a valid codeword has been found. Otherwise the decoding process is repeated whereby the messages R^a_{ij} and Q^a_{ij} are iteratively updated until a valid codeword is found or the maximum number of iterations is reached. On the final iteration the first k symbols of $\underline{\hat{w}}$ are converted to kp information bits $\underline{\hat{u}}$.

4.5.6 The Fast Fourier Transform

An iterative algorithm is used to calculate $\mathcal{F}(\underline{a})$ where the elements of $\underline{a}$ are in the signed log domain. The inverse FFT is simply $\mathcal{F}^{-1}(\underline{a}) = \mathcal{F}(\underline{a})$ where the normalisation by $1/q$ in [96] can be ignored as one is dealing with LLRs.

The algorithm is initialised by setting $\underline{x}_1 = \underline{a}$. For each iteration $d = \{1, \ldots, p\}$ and each vector in the set $l = \{1, \ldots, 2^{d-1}\}$ of length 2^{p-d+1}, two new vectors of length 2^{p-d} are formed by taking the sum and difference of element pairs in $\underline{x}_l$ as follows

$$\underline{x}_l^+ = [x_{l1} \oplus x_{l2}, x_{l3} \oplus x_{l4}, \ldots] \tag{4.17}$$

$$\underline{x}_l^- = [x_{l1} \ominus x_{l2}, x_{l3} \ominus x_{l4}, \ldots]. \tag{4.18}$$

Here $\oplus$ and $\ominus$ denote addition and subtraction in the signed log domain respectively which will be discussed in section 4.5.7. A new set of 2^d vectors is then formed where the first 2^{d-1} vectors in the set are $\underline{x}_l^+$ and the remaining 2^{d-1} vectors are $\underline{x}_l^-$. This new set of vectors is used as the input for the next iteration. On the final iteration p one has a set of q scalars and $\mathcal{F}(\underline{a}) = [x_1, \ldots, x_q]$ where the vector notation for $\underline{x}$ can be dropped as one is dealing with scalars.

To clarify the algorithm, an example is given to find $\mathcal{F}(\underline{a})$ over $GF(4)$. Two new vectors of length 2 are calculated on 1st iteration where

$$\begin{aligned} \underline{x}_1^+ &= [a_1 \oplus a_2, a_3 \oplus a_4] \\ \underline{x}_1^- &= [a_1 \ominus a_2, a_3 \ominus a_4]. \end{aligned}$$

A new set of vectors is then formed by setting $\underline{x}_1 = \underline{x}_1^+$ and $\underline{x}_2 = \underline{x}_1^-$. On the 2nd iteration four new vectors of length 1 are calculated where

$$\begin{aligned} x_1^+ &= [(a_1 \oplus a_2) \oplus (a_3 \oplus a_4)] \\ x_1^- &= [(a_1 \oplus a_2) \ominus (a_3 \oplus a_4)] \\ x_2^+ &= [(a_1 \ominus a_2) \oplus (a_3 \ominus a_4)] \\ x_2^- &= [(a_1 \ominus a_2) \ominus (a_3 \ominus a_4)]. \end{aligned}$$

A new set of vectors is then formed by setting $x_1 = x_1^+$, $x_2 = x_2^+$, $x_3 = x_1^-$ and $x_4 = x_2^-$. It follows that $\mathcal{F}(\underline{a}) = [x_1, x_2, x_3, x_4]$.

4.5.7 Signed Log Domain Addition and Subtraction

Addition and subtraction in the signed log domain is rather complex where separate calculations are required for the sign and magnitude. The calculation of $z = x \oplus y$ is given by

$$z(s) = \begin{cases} x(s), & \text{if } x(s) = y(s) \text{ or } x(m) \geq y(m) \\ -x(s), & \text{otherwise} \end{cases} \tag{4.19}$$

and

$$\begin{aligned} z(m) &= \max\left[x(m), y(m)\right] + \log\left(1 + \gamma e^{-|x(m)-y(m)|}\right) \\ \gamma &= \begin{cases} 1, & \text{if } x(s) = y(s) \\ -1, & \text{otherwise.} \end{cases} \end{aligned} \tag{4.20}$$

The calculation of $z = x \ominus y$ is accomplished by setting $y(s) = -y(s)$ and then calculating $z = x \oplus y$ as described in (4.19) and (4.20). The calculation of (4.20) can be computed more efficiently using a lookup table.

4.5.8 Decoding Complexity

A comparison of the approximate computational complexity of the FFT and log-FFT decoding algorithms for a constant input frame length of K bits is presented in Table 4.2. In this table, the number of floating point operations per iteration is given for the variable and check node update steps. Here $N = np$, $M = mp$ and the average variable and check node degrees are denoted by $\bar{d}_v$ and $\bar{d}_c$ respectively. In moving from $GF(2)$ to $GF(q)$, the size of the parity check matrix is reduced by a factor of p as each symbol now represents p bits. It can be seen that the advantage of the implementing the FFT decoding algorithm in the log domain, is that floating point multiplications are replaced by floating point additions which are far less computationally intensive to implement. Therefore, ignoring table lookups, the approximate complexity of the log-FFT algorithm is $O(q/p)$. Note that N remains constant for all field sizes q.

Table 4.2: Decoding complexity of the FFT and log-FFT algorithms, in floating point operations per iteration.

	Addition	Multiplication	Lookup
FFT			
Variable Nodes	0	$N\bar{d}_v^2 q/p$	0
Check Nodes	$2M\bar{d}_c q$	$M(\bar{d}_c^2 - 1)q/p$	0
log-FFT			
Variable Nodes	$N\bar{d}_v^2 q/p$	0	0
Check Nodes	$M(\bar{d}_c^2 - 1)q/p$	0	$2M\bar{d}_c q$

4.6 EXIT Charts for Non-Binary LDPC Codes

The LDPC decoder operates by exchanging *extrinsic* messages between a set of variable nodes and a set of check nodes in an iterative fashion. The set of variable and check nodes and the operations they perform will be referred to as the variable node decoder (VND) and the check node decoder (CND) as shown in Fig. 4.5. Here the notation I_{ch} denotes the mutual information of the channel messages, I_{av} and I_{ev} denote the mutual information at the VND input and output and I_{ac} and I_{ec} denote the mutual information at the CND input and output.

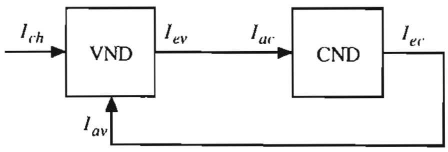

Figure 4.5: Iterative LDPC decoder.

An EXIT curve describes the transfer of mutual information through a particular decoder. An EXIT chart is the superposition of the VND and CND EXIT curves on the same set of axes which graphically illustrates the exchange of mutual information between the two decoders thus giving insight into the decoder operation. In this way, the convergence behaviour of the LDPC decoder can be determined, without the need to run lengthly BER simulations.

The EXIT curves of both the VND and CND could be obtained by simulating the decoding process and measuring the mutual information at the input and output of the decoder for each iteration. However for low SNRs and high variable or check node degrees, it is difficult to obtain an EXIT curve for the full range of I_{av} or I_{ac} as the decoder may fail to converge on the correct codeword. For this reason a model for the VND and CND is proposed whereby the input messages are modelled using a Gaussian distribution which allows the input messages to be generated with the desired I_{av} or I_{ac}. In this way the entire EXIT curve can be generated for the full range of mutual information. Analytical expressions are also presented which can be used to calculate the EXIT curves of the VND and CND orders of magnitude faster than the decoder model.

The optimisation of non-binary LDPC codes using EXIT charts is considered in this section. Firstly the calculation of the mutual information is described. The proposed model for the VND and CND of regular LDPC codes is presented and analytical expressions are given for the VND and CND EXIT curves. The EXIT curves obtained from the model and analysis are compared to simulation results to assess their accuracy. Analytical expressions are then presented for the EXIT curves of irregular LDPC codes and are compared to simulation results. Finally the optimisation of non-binary LDPC codes is described which involves matching the EXIT curves of the VND and CND.

4.6.1 Calculation of the Mutual Information

With binary LDPC codes, a single message is passed along each edge of the bipartite graph while with non-binary codes, q messages are passed along each edge. EXIT charts for non-binary codes have been considered in [108–110]. Here, the calculation of the mutual information required the numerical evaluation of a multi-dimensional integral. For non-binary LDPC codes over $GF(q)$ this requires evaluating a $q-1$ dimensional integral which is computationally expensive for $q > 4$. Furthermore it is found that when using this metric the EXIT curve of an irregular code is not the average of the component code EXIT curves for $q > 2$ as was the case in [104] for binary LDPC codes.

For these reasons a new metric is proposed. The symbol LLRs are converted to bitwise LLRs and the mutual information between the bitwise LLRs and their corresponding bits is calculated. In this way the $q-1$ dimensional integration is reduced to a one dimensional integration. It is also found that by using this metric, the EXIT curve of an irregular code is simply the average of the component code EXIT curves. The remainder of this section describes the calculation of the proposed metric.

Let L^a be an arbitrary symbol LLR or decoder message and define $\underline{L} = [L^0, \dots, L^{q-1}]$. Let λ be an arbitrary bitwise LLR and denote the conversion from symbol LLRs to bitwise LLRs as $\lambda = \mathcal{B}(\underline{L})$. For each symbol LLR p bitwise LLRs λ_l are calculated for $l = \{1, \dots, p\}$ which corresponds to the l_{th} bit of a. This conversion was discussed in [111] and is given by

$$\lambda_l = \underset{a:a_l=1}{\overset{*}{\max}} \left(L^a\right) - \underset{a:a_l=0}{\overset{*}{\max}} \left(L^a\right) \tag{4.21}$$

where the $\overset{*}{\max}$ operator denotes addition in the log domain as follows

$$\underset{j}{\overset{*}{\max}}(x_j) = \log\left[\sum_{j=1}^{J} e^{x_j}\right]. \tag{4.22}$$

This can be computed recursively in the log domain by setting $\delta_1 = x_1$ and for $j = \{2, \dots, J\}$

$$\delta_j = \max(\delta_j, \delta_{j-1}) + \ln\left[1 + \exp(-|\delta_j - \delta_{j-1}|)\right]. \tag{4.23}$$

On the final iteration δ_J is the solution to (4.22).

The pdfs $p(\lambda|X = 0)$ and $p(\lambda|X = 1)$ are obtained from the histogram of λ. The mutual information between the bits X and the bitwise LLRs $\lambda = \mathcal{B}(\underline{L})$ is [101]

$$I(X; \mathcal{B}(\underline{L})) = \frac{1}{2} \cdot \sum_{x=0,1} \int_{-\infty}^{\infty} p(\lambda|X = x) \log_2 \frac{2p(\lambda|X = x)}{p(\lambda|X = 0) + p(\lambda|X = 1)} d\lambda \tag{4.24}$$

which can be solved numerically.

4.6.2 EXIT Curves for the Variable Node Decoder

Modelling the Variable Node Decoder

Consider an arbitrary variable node of degree d_v which receives d_v messages $L^a_{i,iv}$ from the CND and one message L^a_{ch} from the channel. The variable node computes the d_v output messages as follows for $i = \{1, \dots, d_v\}$ and $a \in GF(q)$

$$L^a_{i,ov} = L^a_{ch} + \sum_{k \neq i} L^a_{k,iv}. \tag{4.25}$$

Assume that the variable node is associated with symbol $x \in GF(q)$ which has binary representation $[x_1, \dots, x_p]$ where $x_l \in \{0, 1\}$. The channel message L^a_{ch} can be modelled using a Gaussian mixture distribution which is obtained by substituting the BPSK representation of x into (4.4) and (4.7) as follows

$$\begin{aligned} L^a_{ch} &= \frac{2}{\sigma_n^2} \sum_{l:\, a_l=1} (2x_l - 1) + \eta_l & (4.26) \\ &= \sum_{l:\, a_l=1} \mu_{ch} \cdot (2x_l - 1) + n_{ch,l}. & (4.27) \end{aligned}$$

Here $\mu_{ch} = \sigma^2_{ch}/2$ and $n_{ch,l}$ is Gaussian distributed with mean zero and variance

$$\sigma^2_{ch} = 8R\frac{E_b}{N_0}. \tag{4.28}$$

The input messages of the VND are more difficult to model and their distribution was carefully studied by simulation as shown in Fig. 4.6. A number of observations were made:

- The input messages of a particular variable node are independent in i.
- The messages approach a Gaussian like distribution with an increasing number of iterations where the mean and the variance are related by $\mu = \sigma^2/2$. This approximation has been successfully made in [99,104] for the binary LDPC codes.
- The messages $L^1_{i,iv}, \dots, L^{q-1}_{i,iv}$ are correlated due to the normalisation of the VND output messages (4.9).

Based on these observations the following model is proposed for VND input messages

$$L_{i,iv}^{a}(\sigma) = \begin{cases} 0, & \text{if } a = 0 \\ \mu + n_i^0 + n_i^a, & \text{if } x = a,\ a \neq 0 \\ -\mu + n_i^0 + n_i^a, & \text{if } x = 0,\ a \neq 0 \\ n_i^0 + n_i^a, & \text{otherwise} \end{cases} \tag{4.29}$$

Here the $\mu = \sigma^2/2$ and n_i^0 and n_i^a are Gaussian distributed with mean zero and variance $\sigma^2/2$ which ensures the variance of $L_{i,iv}^{a}(\sigma)$ is σ^2. The random variable n_i^0 is introduced to model the correlation between the messages $L_{i,iv}^{1}, \ldots, L_{i,iv}^{q-1}$.

The proposed model for the VND input messages is compared to simulation results to investigate its validity. A (3,6) regular LDPC code over $GF(4)$ is used, the SNR is 2 dB and the decoder is allowed to run for 8 iterations. Before calculating the pdf, the simulated input messages $L_{i,iv}^{0}, \ldots, L_{i,iv}^{q-1}$ are normalised by subtracting $L_{i,iv}^{0}$ from each message. The normalised pdfs are presented in Fig. 4.6 where the markers indicate the pdfs obtained from simulation and the solid lines indicate the pdf of the proposed model (4.29). It can be seen that the proposed model, based on the Gaussian distribution, provides a good fit to the simulated results. Although there is a small discrepancy for the central pdfs, it is shown that the EXIT curves obtained using this model are a close match to the simulation results.

Analytical Expressions for the VND EXIT Curves

For binary LDPC codes the channel messages, input messages and output messages of the VND can all be modelled using a Gaussian distribution while for non-binary LDPC codes these messages are modelled using different Guassian mixture distributions given by (4.27), (4.29) and (4.25) respectively. For this reason the analytical expressions for the EXIT curves presented in [104] do not apply directly to non-binary LDPC codes. Therefore two functions

$$J_v(\sigma) = I\left[X; \mathcal{B}(\underline{L}_{ch} + \underline{L}_{iv}(\sigma))\right] \tag{4.30}$$

$$J_c(\sigma) = I\left[X; \mathcal{B}(\underline{L}_{iv}(\sigma))\right] \tag{4.31}$$

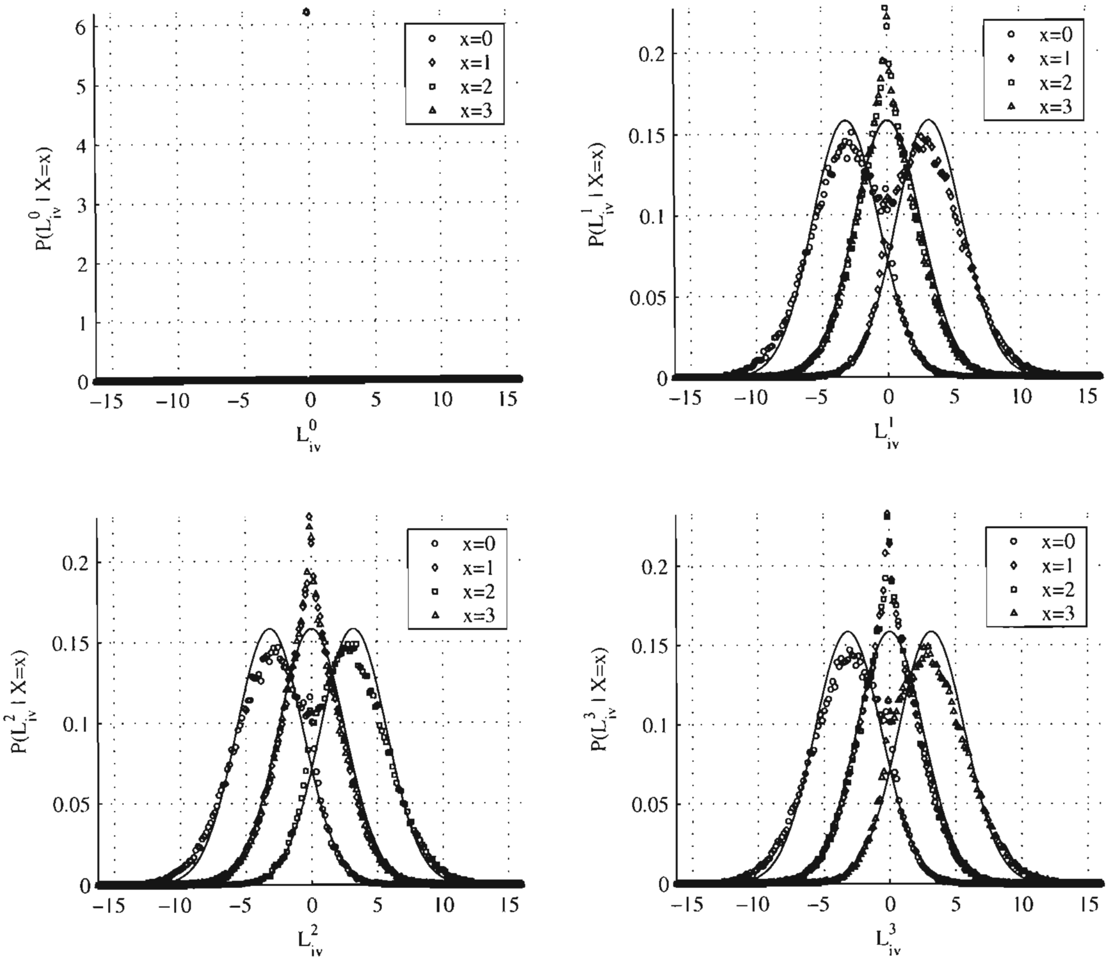

Figure 4.6: Simulated (markers) and modelled (solid lines) pdfs of the normalised VND input messages of a (3,6) regular LDPC code over $GF(4)$ with $E_b/N_0 = 2$ dB.

are defined which relate the standard deviation of the pdf to the mutual information of the messages. In [104], only one such function was defined. Note that $J_v(\sigma)$ accounts for the mutual information of the channel messages where $J_v(0) = I[X; \mathcal{B}(\underline{L}_{ch})]$ which is also the channel capacity. Using these two functions the EXIT curve of a degree d_v variable node is given by

$$I_{ev}(I_{av}, d_v) = J_v\left(\sqrt{d_v - 1} \cdot J_c^{-1}(I_{av})\right). \tag{4.32}$$

Here $I_{av} = I[X; \mathcal{B}(\underline{L}_{iv})]$ is the average mutual information at the VND input and $I_{ev}(I_{av}, d_v) = I[X; \mathcal{B}(\underline{L}_{ov})]$ is the average mutual information at the VND output. For computer implementation the functions $J_v(\sigma)$ and $J_c^{-1}(I_{av})$ can be computed using a lookup table or the curve fitting approach suggested in [104].

Comparison with Simulation Results

In Fig. 4.7 the VND EXIT curves are presented for a $GF(4)$ LDPC code with varying variable node degrees. The EXIT curves obtained from the model (4.25) and the analysis (4.32) are compared with the simulation results of a "free-running" iterative decoder with a frame length of $N = 12\ 000$ bits. For the decoder model the EXIT curve is averaged over 10^6 messages while for the simulation the snapshot trajectory [101] for a single frame is taken. It can be seen that there is good agreement between the model, analysis and simulation.

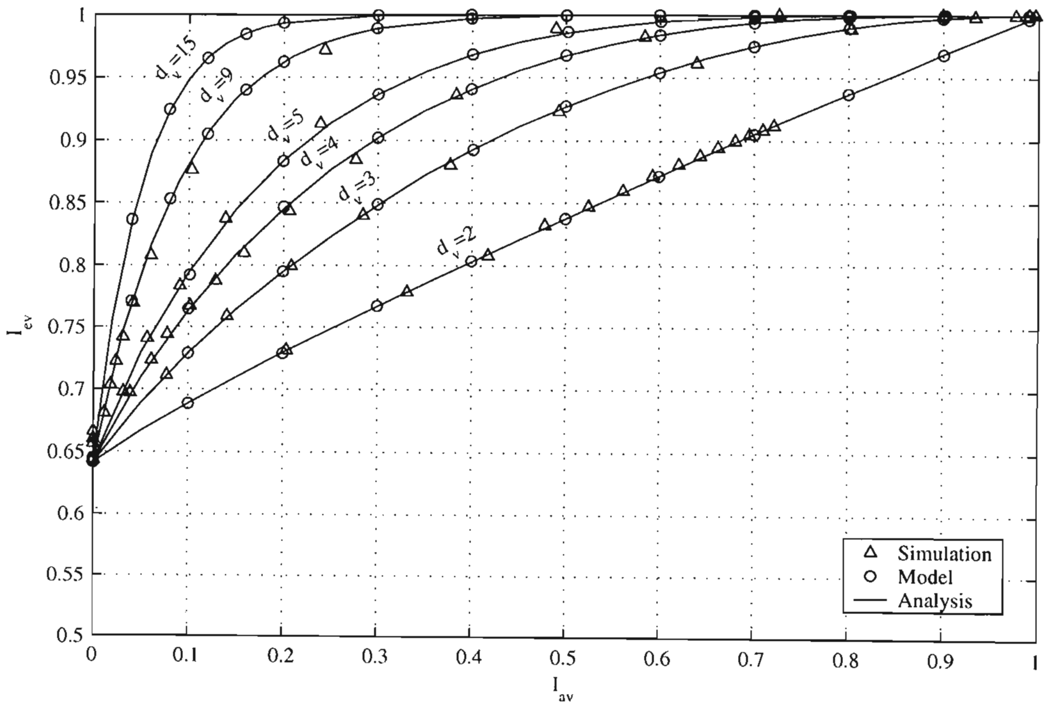

Figure 4.7: VND EXIT curves for $GF(4)$ LDPC codes with $R = 1/2$ and $E_b/N_0 = 2$ dB.

4.6.3 EXIT Curves for the Check Node Decoder

Modelling the Check Node Decoder

Consider an arbitrary check node of degree d_c which receives d_c messages $L^a_{i,ic}$ from the VND. Define $\underline{h}$ as the vector of parity checks associated with this check node and $\underline{x}$ as the encoded symbols which satisfy these checks. These length d_c vectors contain elements from $GF(q)$ and satisfy the equality $\underline{h}\,\underline{x}' = 0$ where the arithmetic is performed over $GF(q)$.

The check node computes the d_c output messages $L^a_{i,oc}$ as follows for $i = \{1, \ldots, d_c\}$ and $a \in GF(q)$

$$\begin{aligned}
\underline{\tilde{L}}_{i,ic} &= \mathcal{F}\left[\mathcal{P}_i\left(\underline{\bar{L}}_{i,ic}\right)\right] && (4.33)\\
\tilde{L}^a_{i,oc}(s) &= \prod_{k \neq i} \tilde{L}^a_{k,ic}(s) && (4.34)\\
\tilde{L}^a_{i,oc}(m) &= \sum_{k \neq i} \tilde{L}^a_{k,ic}(m) && (4.35)\\
\underline{\bar{L}}_{i,oc} &= \mathcal{P}_i^{-1}\left[\mathcal{F}^{-1}\left(\underline{\tilde{L}}_{i,oc}\right)\right] && (4.36)
\end{aligned}$$

The notation used here as well as the conversion between signed LLRs $\bar{L}^a_{i,ic}$ and decoder messages $L^a_{i,ic}$ is described in section 4.5.4. The permutation of the elements in the vector $\underline{\bar{L}}_{i,ic}$ is with respect to element h_i of $\underline{h}$.

In order to construct a model for the input messages of the CND, their distribution was studied by simulation. It was observed that the input messages are independent and that their pdf is a composite of the pdfs of the input and channel messages of the VND. For this reason the model for the CND input messages is effectively a combination of the models for the VND input and channel messages. However, each VND input message corresponds to the same symbol x while each CND input message corresponds to a possibly different symbol x_i.

Based on these observations, the CND input messages can be modelled by

$$L^a_{i,ic}(\sigma) = L^a_{i,c}(\sigma) + \sum_{l:\, a_l=1} \mu_{ch} \cdot (2x_{i,l} - 1) + n_{ch,i,l} \tag{4.37}$$

$$L^a_{i,c}(\sigma) = \begin{cases} 0, & \text{if } a = 0 \\ \mu + n^0_i + n^a_i, & \text{if } x_i = a,\ a \neq 0 \\ -\mu + n^0_i + n^a_i, & \text{if } x_i = 0,\ a \neq 0 \\ n^0_i + n^a_i, & \text{otherwise} \end{cases} \tag{4.38}$$

where $x_{i,l}$ is the lth bit of x_i, $\mu = \sigma^2/2$ and $n_{ch,i,l}$ and n^a_i are Gaussian distributed with mean zero and variance σ^2_{ch} and $\sigma^2/2$ respectively.

Analytical Expressions for the CND EXIT Curves

In [104], the EXIT curve of the CND was expressed in terms of the EXIT curve of the VND based on the duality property [103]. Define $I_{ac} = I[X; \mathcal{B}(\underline{L}_{ic})]$ as the average mutual information at the CND input and $I_{ec}(I_{ac}, d_c) = I[X; \mathcal{B}(\underline{L}_{oc})]$ as the average mutual information at the CND output. The analytical expression for the EXIT curve of a degree d_c check node is given by [104]

$$I_{ec}(I_{ac}, d_c) = 1 - J_c\left(\sqrt{d_c - 1} \cdot J_c^{-1}(1 - I_{ac})\right) \tag{4.39}$$

which is accurate for $GF(2)$ but did not prove accurate for $GF(q > 2)$. In [104], binary LDPC codes were considered where the pdf of the input and output messages was described by the same model which is not the case for non-binary LDPC codes. The problem is compounded because $J_v(\sigma)$ is defined for the range $[J_v(0), 1]$ and for this reason no inverse $J_v^{-1}(I_a)$ exists for $I_a < J_v(0)$. For these reasons it is not possible to extend the analytical expressions of [104] to the non-binary case.

However the EXIT curve of a degree d_c check node can be well approximated by

$$I_{ec}(I_{ac}, d_c) = I_{ac}^{\alpha(d_c) \cdot I_{ac} + \beta(d_c)} \tag{4.40}$$

where the constants $\alpha(d_c)$ and $\beta(d_c)$ are dependent on the check node degree, field size and SNR. These constants can be calculated by fitting (4.40) to the CND EXIT curves of interest. The CND EXIT curves can be generated using the decoder model proposed in the previous section.

Comparison with Simulation Results

The CND EXIT curves for a number of different check node degrees are presented in Fig. 4.8 for a $GF(4)$ LDPC code. The EXIT curves from the model (4.36) and the analysis (4.40) are compared with the simulation results. The parameters used for the model and simulation are the same as those used for the VND EXIT curves. It is observed that the model, analysis and simulation agree.

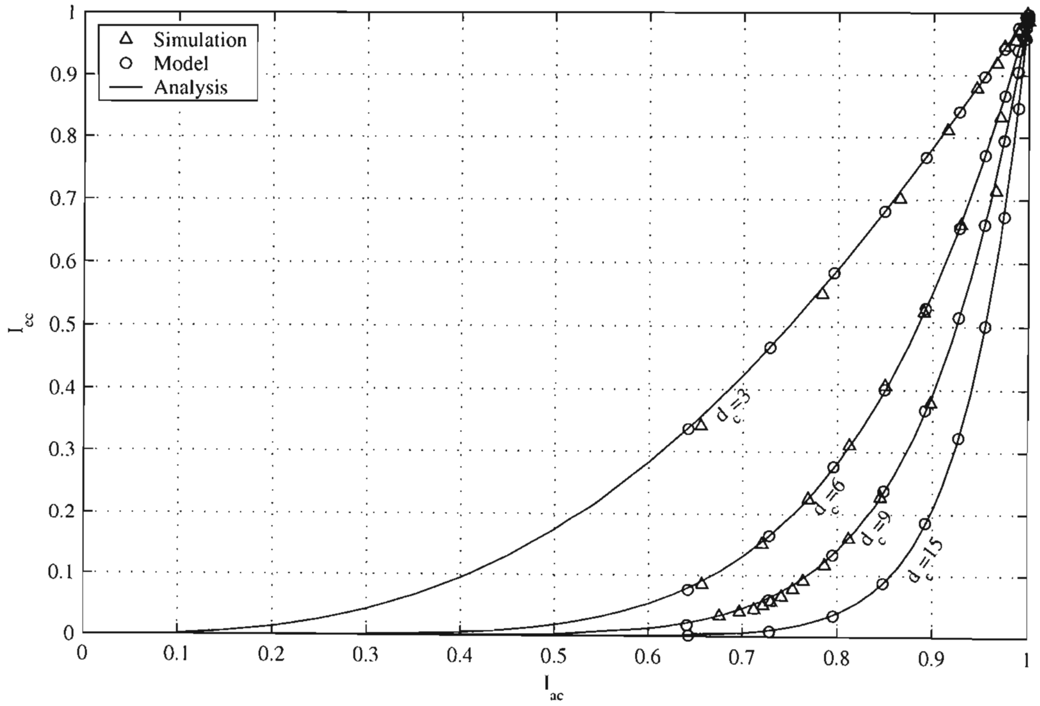

Figure 4.8: CND EXIT curves for $GF(4)$ LDPC codes with $R = 1/2$ and $E_b/N_0 = 2$ dB.

4.6.4 Irregular LDPC Codes

For binary LDPC codes the EXIT curve of an irregular code is simply the average of the component code EXIT curves [103, 104, 112]. Using the proposed metric this was found to be true for non-binary LDPC codes as well. The averaging must be done with respect to the edge fractions, not the node fractions as defined previously, because it is the edges which carry the decoder messages. The node fractions λ_i and ρ_i are converted to edge fractions λ_i^e and ρ_i^e as follows

$$\lambda_i^e = \frac{i\lambda_i}{\sum_i i\lambda_i} \tag{4.41}$$

$$\rho_i^e = \frac{i\rho_i}{\sum_i i\rho_i} \tag{4.42}$$

The VND and CND EXIT curves of an irregular LDPC code are given by

$$I_{ev}(I_{av}) = \sum_i \lambda_i^e \cdot I_{ev}(I_{av}, i) \tag{4.43}$$

$$I_{ec}(I_{ac}) = \sum_i \rho_i^e \cdot I_{ec}(I_{ac}, i). \tag{4.44}$$

In Fig. 4.9 and Fig. 4.10 the analytical EXIT curves, (4.43) and (4.44), are compared to the average decoding trajectory obtained from simulation for the finite fields $GF(4)$ and $GF(8)$. The axes for the CND EXIT curve are swapped. The $GF(4)$ code from [96] is considered where the variable and check node profiles are given in Table 4.1. The frame length is $N = 12\ 000$ bits and the decoding trajectory is averaged over 20 frames. It is observed that the analysis provides a good approximation of the decoding trajectory.

4.6.5 Optimisation of Non-Binary LDPC Codes using EXIT Charts

In [103], it was shown that to design LDPC codes which approach capacity the VND and CND EXIT curves must be matched exactly. This design approach was applied in [104] to optimise LDPC codes for both the AWGN and MIMO channels and in [105] to optimise repeat-accumulate codes for the MIMO channel. This approach is employed here to optimise non-binary LDPC codes for the AWGN channel.

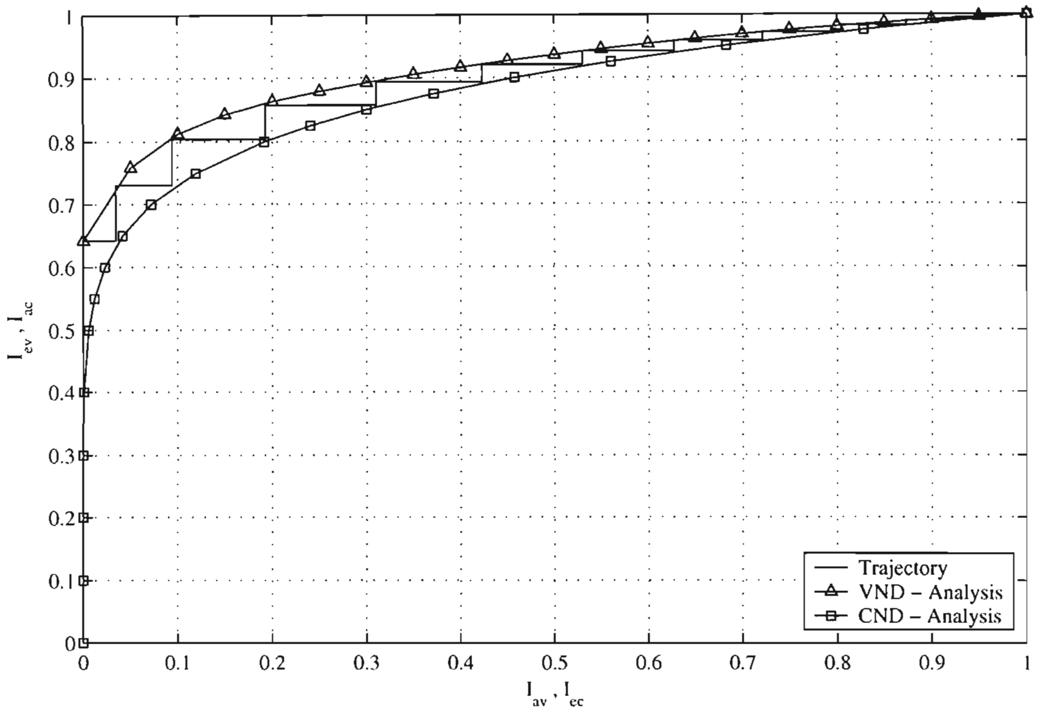

Figure 4.9: EXIT chart for an irregular $GF(4)$ LDPC code with $R = 1/2$ and $E_b/N_0 = 2$ dB.

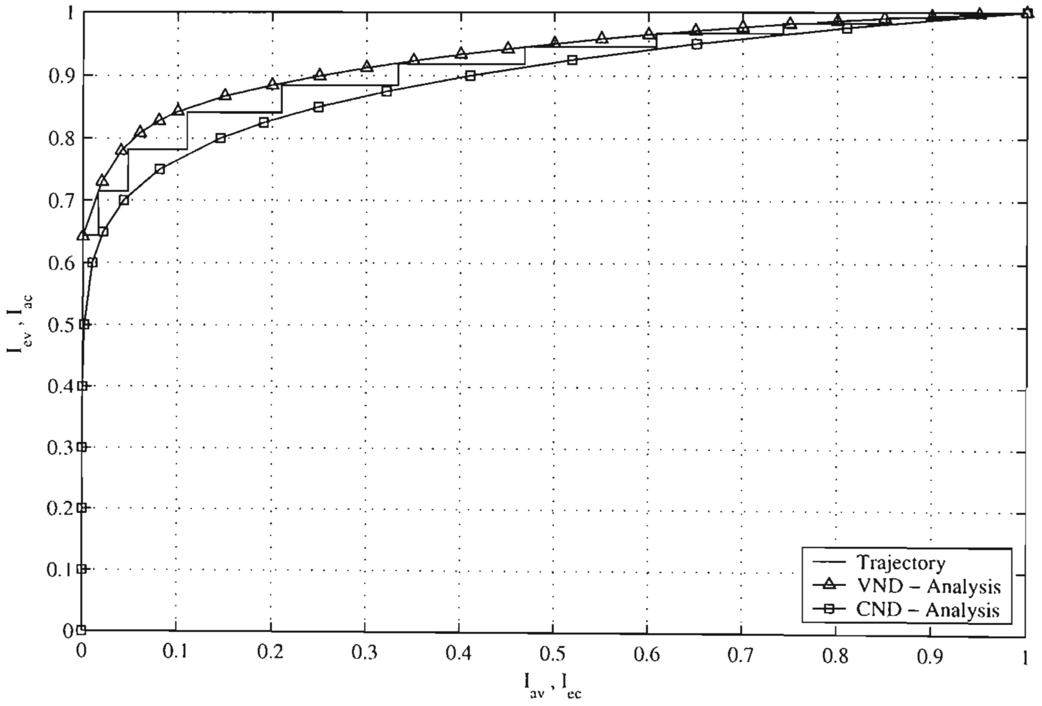

Figure 4.10: EXIT chart for an irregular $GF(8)$ LDPC code with $R = 1/2$ and $E_b/N_0 = 2$ dB.

Cost Functions

In [104], a cost function was not given to assess how well the VND EXIT curve matched the CND EXIT curve and the curve matching was done by manually. In this thesis the curve matching is performed using an optimisation algorithm together with a cost function to assess the match between the EXIT curves. The following four cost functions are investigated:

- **Mean Square Error (MSE):** Evaluates the MSE between the VND and CND EXIT curves. The error is given by

$$E(I_{av}) = I_{ec}[I_{ev}(I_{av})] - I_{av} \tag{4.45}$$

  and can be efficiently calculated using (4.43) and (4.44).

- **Variance:** Calculates the variance of the error $E(I_{av})$ between the VND and CND EXIT curves.

- **Iterations:** Measures the number of iterations taken to reach $I_{ec} = 1$ starting at $I_{av} = 0$. One iteration is evaluated by calculating $I_{ec} = I_{ec}[I_{ev}(I_{av})]$ and then setting $I_{av} = I_{ec}$ for the next iteration. To prevent the decoder from getting stuck, which will occur if the EXIT curves touch or overlap, the maximum number of iterations is set to 200.

- **Area:** Calculates the area between the VND and CND EXIT curves. The area under the VND and CND EXIT curves is given by A_v and A_c respectively and is calculated using trapezoidal numerical integration. For each point that the CND EXIT curve lies above the VND EXIT curve, i.e. $E(I_{av}) < 0$, a penalty function A_p is incremented by 0.01. The area cost function is given by $A_v - A_c + A_p$.

To evaluate the MSE, variance and area cost functions, 100 equally spaced points in the interval $[0, 1]$ are used.

Optimisation Algorithm

An optimisation algorithm can now be employed to search for the code profile which minimises the chosen cost function. The variable and check node degree profiles cannot be chosen freely and are constrained by

$$\sum_i \lambda_i = 1, \quad 0 \leq \lambda_i \leq 1 \tag{4.46}$$

$$\sum_i \rho_i = 1, \quad 0 \leq \rho_i \leq 1 \tag{4.47}$$

$$\sum_i i\lambda_i = (1-R)\sum_i i\rho_i. \tag{4.48}$$

This is a constrained, nonlinear, multidimensional optimisation problem. Differential evolution (DE) [113] has recently proven itself as a robust optimiser for multivariate functions. The algorithm is in part a hill climbing algorithm and in part a genetic algorithm and has been applied to a large range of optimisation problems. It has been successfully used to optimise irregular LDPC codes for different channels [89,91,139]. In this chapter DE is used to minimise the chosen cost function and is described in detail in appendix C.

4.7 Optimisation Results

The proposed EXIT chart approach is now used to optimise $GF(4)$ and $GF(8)$ LDPC codes with $R = 1/2$ for the AWGN channel. To limit the search space, LDPC codes with 3 variable node degrees and 1 check node degree are considered. The variable node profile is optimised using DE in conjunction with the cost functions presented previously. The LDPC codes are decoded using the log-FFT decoding algorithm, described in section 4.5, where the maximum number decoding iterations is 100.

4.7.1 Evaluation of the Cost Functions

The cost functions presented in section 4.6.5 are evaluated by comparing the BER performance of the LDPC codes optimised using each cost function. The variable and check node degrees are fixed to values which are known to give good LDPC codes. In this case the optimisation is performed using DE for fixed variable node degrees as described in appendix C.1. In [104], it was discussed that the EXIT curves should be matched at a SNR where the channel capacity is slightly larger than the code rate. The channel capacity is given by $J_v(0)$ and is 0.5012 at $E_b/N_0 = 0.2$ dB and 0.5243 at $E_b/N_0 = 0.5$ dB. This is slightly larger than $R = 1/2$ in both cases. The results of the search for $GF(4)$ LDPC codes at 0.2 dB and 0.5 dB, based on the four cost functions, are presented in Table 4.3.

Table 4.3: Profiles for $GF(4)$ LDPC codes with $R = 1/2$, optimised for fixed variable node degrees using the MSE, variance, iterations and area cost functions.

	$E_b/N_0 = 0.2$ dB
MSE	$\rho_7 = 1,\ \lambda_2 = 0.57323,\ \lambda_3 = 0.29261,\ \lambda_{11} = 0.13415$
Variance	$\rho_7 = 1,\ \lambda_2 = 0.52753,\ \lambda_3 = 0.34402,\ \lambda_{11} = 0.12844$
Iterations	$\rho_7 = 1,\ \lambda_2 = 0.53475,\ \lambda_3 = 0.33590,\ \lambda_{11} = 0.12934$
Area	$\rho_7 = 1,\ \lambda_2 = 0.56130,\ \lambda_3 = 0.30604,\ \lambda_{11} = 0.13266$
	$E_b/N_0 = 0.5$ dB
MSE	$\rho_7 = 1,\ \lambda_2 = 0.60287,\ \lambda_3 = 0.25927,\ \lambda_{11} = 0.13786$
Variance	$\rho_7 = 1,\ \lambda_2 = 0.50637,\ \lambda_3 = 0.36783,\ \lambda_{11} = 0.12580$
Iterations	$\rho_7 = 1,\ \lambda_2 = 0.43878,\ \lambda_3 = 0.44387,\ \lambda_{11} = 0.11735$
Area	$\rho_7 = 1,\ \lambda_2 = 0.59880,\ \lambda_3 = 0.26385,\ \lambda_{11} = 0.13735$

EXIT charts for the $GF(4)$ LDPC codes optimised at 0.5 dB are given in Fig. 4.11 for each cost function. It is observed that for the MSE and area EXIT charts, the VND and CND EXIT curves converge at $I_{av} \approx 0.6$ which may cause the decoding trajectory to get stuck at this point. It is therefore predicted that the LDPC codes optimised using the MSE and area cost functions will have poor performance. The variance and iterations EXIT charts are similar. In both cases a small gap is present between the EXIT curves for the entire range of I_{av}. However, the EXIT curves for the iterations chart are closer than the variance chart for $I_{av} < 0.3$ and further apart for $I_{av} > 0.6$. Therefore the decoding trajectory of the codes optimised using the iterations

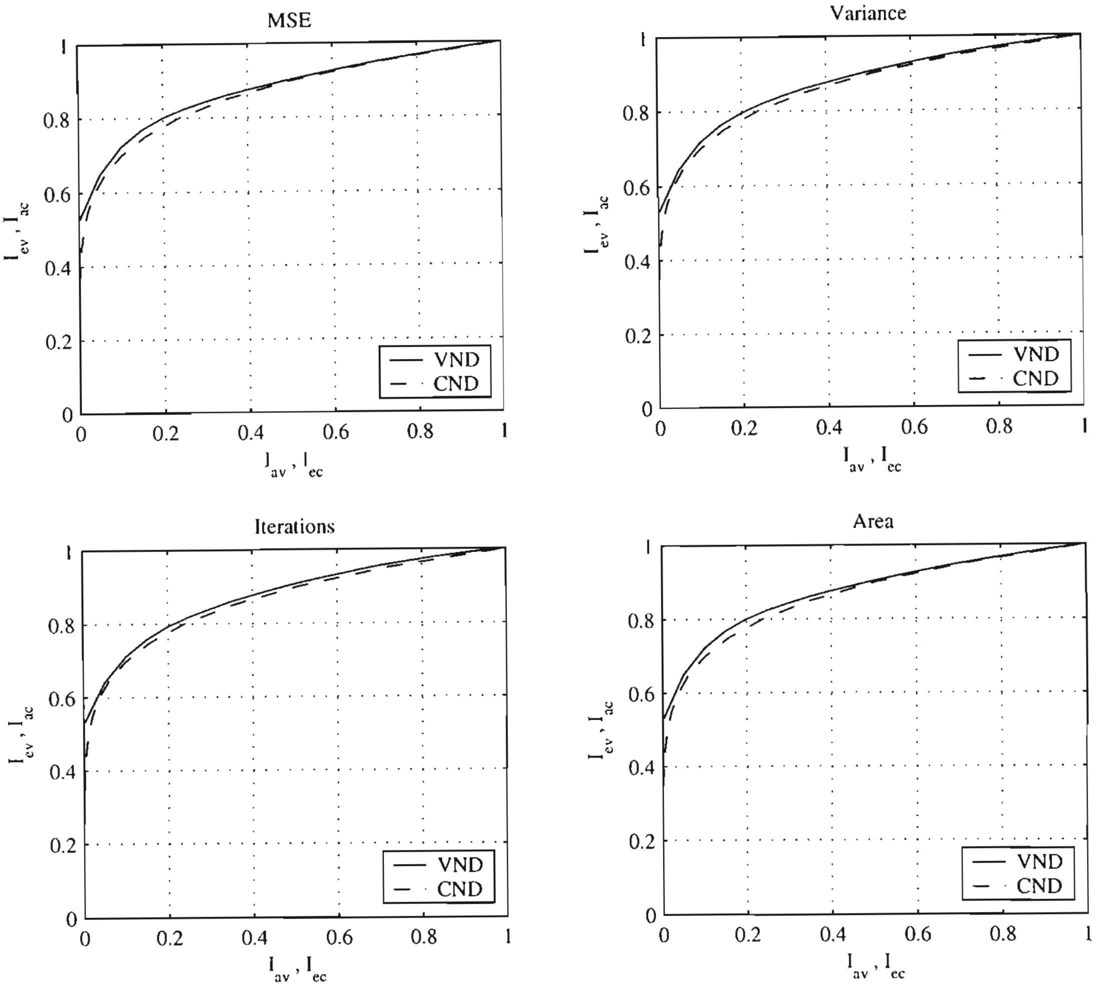

Figure 4.11: EXIT charts for the $GF(4)$ LDPC codes from Table 4.3 optimised at $E_b/N_0 = 0.5$ dB using the MSE, variance, iterations and area cost functions.

cost function is more likely to get stuck at low I_{av} while the decoding trajectory of the codes optimised using the variance cost function is more likely to get stuck at high I_{av}. The latter is more favourable and it is expected that codes optimised using the variance cost function at 0.5 dB will have the best performance.

The performance of the optimised codes is assessed by simulation and their performance is compared to the $GF(4)$ code of [96] as a benchmark. This code was optimised using a simulation based cost function and its profile is given in Table 4.1. A frame length of N = 60 000 bits is used since it was for this frame length that the code from [96] was optimised. The simulation results are presented in Fig. 4.12 and Fig. 4.13 for the

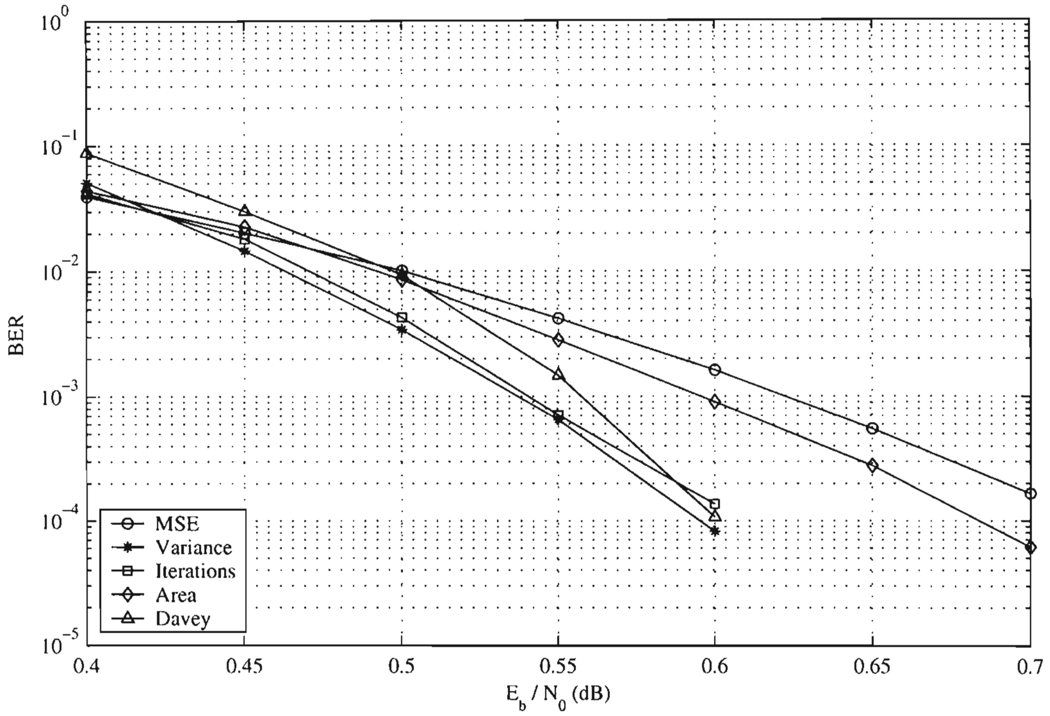

Figure 4.12: Simulation results for the $GF(4)$ LDPC codes from Table 4.3 with $N = 60\ 000$, optimised at $E_b/N_0 = 0.2$ dB.

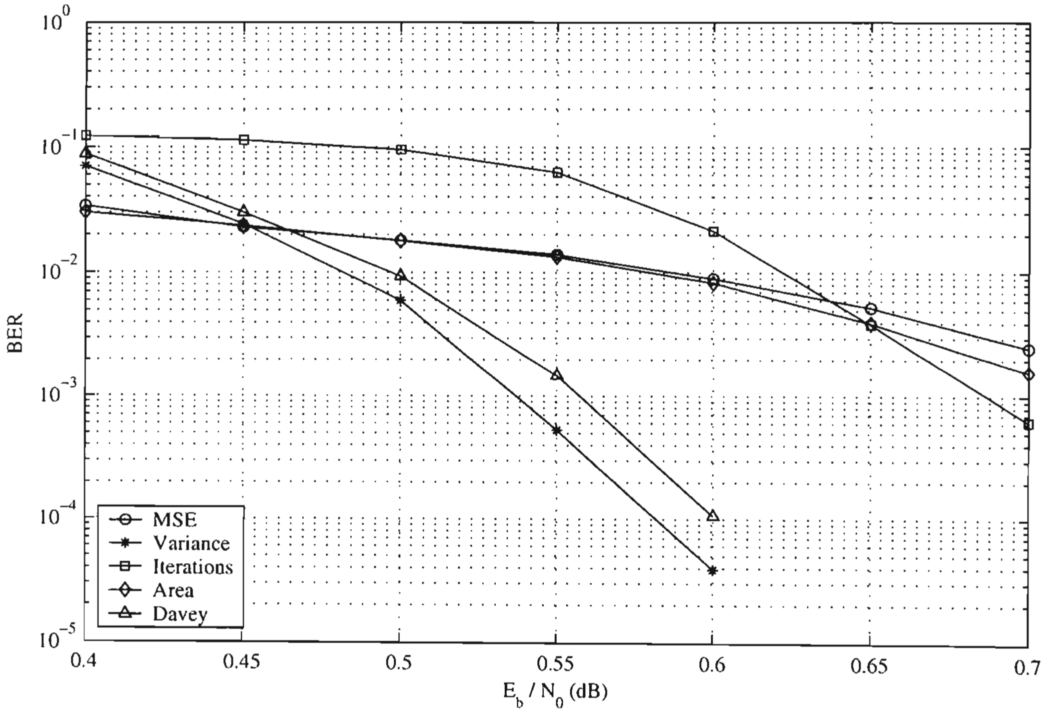

Figure 4.13: Simulation results for the $GF(4)$ LDPC codes from Table 4.3 with $N = 60\ 000$, optimised at $E_b/N_0 = 0.5$ dB.

codes optimised at 0.2 dB and 0.5 dB respectively. The code from [96] is denoted by 'Davey'. It is observed that the code achieving the best performance is optimised using the variance cost function for both SNRs. Therefore the predictions made by studying the EXIT charts of the various cost functions at 0.5 dB were correct. The LDPC code optimised at 0.5 dB outperforms the code optimised at 0.2 dB when using the variance cost function and for this reason it is preferred to optimise the LDPC codes at 0.5 dB.

In addition the code optimised using the variance cost function outperforms the code optimised in [96] for both SNRs even though the code optimised here uses fewer variable and check node degrees. This indicates that the proposed optimisation method, based on EXIT charts, is a promising technique for optimising non-binary LDPC codes. Furthermore the approach used here is considerably less computationally intensive, requiring only function evaluations and table lookups, than the simulation based method used in [96] which requires averaging the number of decoding iterations taken to decode the given code.

4.7.2 Optimising the Variable Node Degrees

The EXIT chart approach has been shown to find good codes if the variable node degrees are fixed. However it would be useful if the variable node degrees could optimised as well. To limit the search space, the codes are constrained to have variable nodes of degree 2 and 3 which is the case for good LDPC codes found in the literature [89,91,96]. Therefore the optimisation algorithm is required to find the third variable node degree and degree fractions which minimise the cost function. This can be done using the DE algorithm for free variable node degrees as described in appendix C.2.

LDPC codes are optimised at 0.5 dB with each cost function and the results are presented in Table 4.4. The simulation results are given in Fig. 4.14 where $N = 60\ 000$. It is shown that the optimal variable node profile is not found using the four cost functions but the variance cost function gives the best results.

Table 4.4: Profiles for $GF(4)$ LDPC codes with $R = 1/2$, optimised for free variable node degrees using the MSE, variance, iterations and area cost functions.

	$E_b/N_0 = 0.5$ dB
MSE	$\rho_7 = 1,\ \lambda_2 = 0.53930,\ \lambda_3 = 0.40600,\ \lambda_{22} = 0.05470$
Variance	$\rho_7 = 1,\ \lambda_2 = 0.48969,\ \lambda_3 = 0.42033,\ \lambda_{14} = 0.08997$
Iterations	$\rho_7 = 1,\ \lambda_2 = 0.39464,\ \lambda_3 = 0.50596,\ \lambda_{12} = 0.09940$
Area	$\rho_7 = 1,\ \lambda_2 = 0.56091,\ \lambda_3 = 0.36836,\ \lambda_{18} = 0.07073$

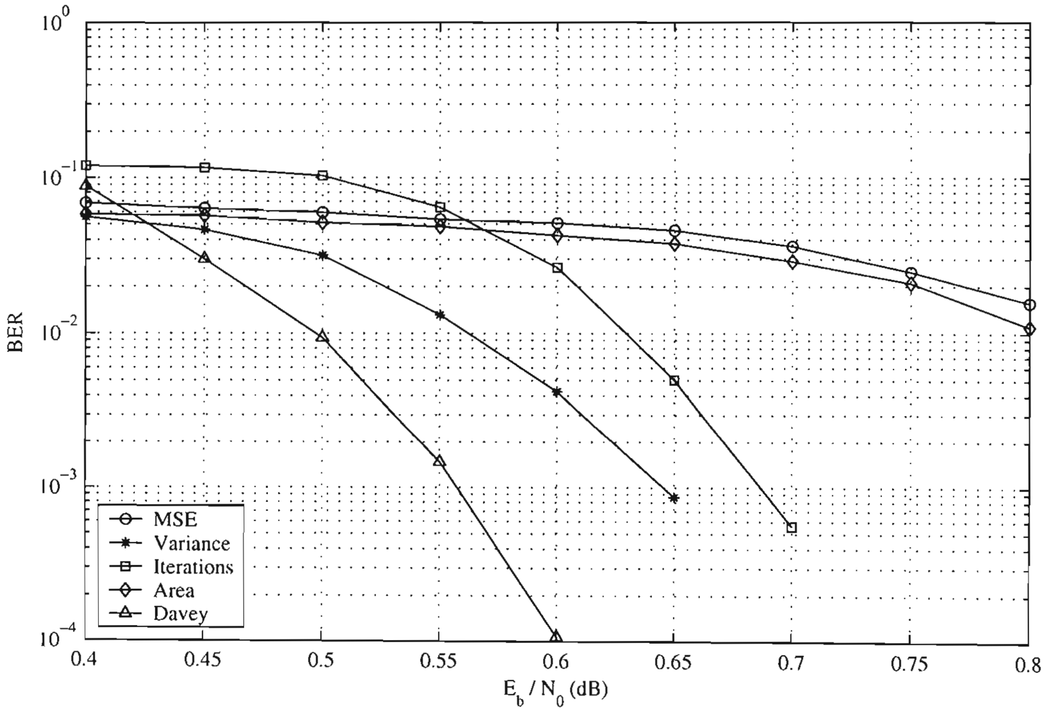

Figure 4.14: Simulation results for the $GF(4)$ LDPC codes from Table 4.4 with $N = 60\ 000$, optimised at $E_b/N_0 = 0.5$ dB.

This optimisation approach, based on EXIT charts, makes the assumption that the bipartite graph associated with the code is cycle-free which is only valid for infinitely long codes. In practice, finite block length effects lead to cycles in the bipartite graph which degrade the performance of the code. For this reason, the EXIT chart approach falls down as it is attempting to optimise infinite codes and not codes of length $N = 60$ 000. Therefore the proposed optimisation approach is only useful if an optimal set of variable node degrees are chosen or if a limit is placed on the maximum allowed variable node degree. For the optimisation of binary LDPC codes using density evolution [89,91] a limit was also placed on the maximum variable node degree. This limit depends on the length of the code and can be found by trial and error.

4.7.3 Optimal LDPC Codes for $GF(4)$ and $GF(8)$

The variance cost function is now used to optimise LDPC codes over $GF(4)$ and $GF(8)$ at 0.5 dB where the variable node degrees are fixed. As discussed in [104] the check node degree is chosen so that the CND EXIT curve is a small distance from the $y-$axis at $I_{ac} = 0.5$. In this way I_{ec} is not too small on the first iteration which gives the decoder a good start. The set of variable node degrees are chosen using a trial an error approach starting with the profile selected by the DE algorithm for free variable node degrees and then fine tuning the maximum variable node degree until the optimal code is found for the frame length of interest. Fine tuning is required because this optimisation approach assumes that the bipartite graph associated with the code is cycle-free which is only valid for infinitely long codes. For each set of variable node degrees, the degree fractions are optimised using DE for fixed variable node degrees with the variance cost function.

The resulting profile for the $GF(4)$ and $GF(8)$ codes are given in Table 4.5 and simulation results are presented in Fig. 4.15. It is observed that the optimised codes give superior performance to the $GF(4)$ code from [96]. Additionally the optimised $GF(8)$ code outperforms the optimised $GF(4)$ code which concurs with the conclusions of [96] that LDPC codes over higher order fields achieve superior results.

Table 4.5: Profiles for $GF(4)$ and $GF(8)$ LDPC codes with $R = 1/2$, optimised for fixed variable node degrees using the variance cost function.

	$E_b/N_0 = 0.5$ dB
$GF(4)$	$\rho_7 = 1,\ \lambda_2 = 0.50637,\ \lambda_3 = 0.36783,\ \lambda_{11} = 0.12580$
$GF(8)$	$\rho_6 = 1,\ \lambda_2 = 0.62763,\ \lambda_3 = 0.26776,\ \lambda_9 = 0.10461$

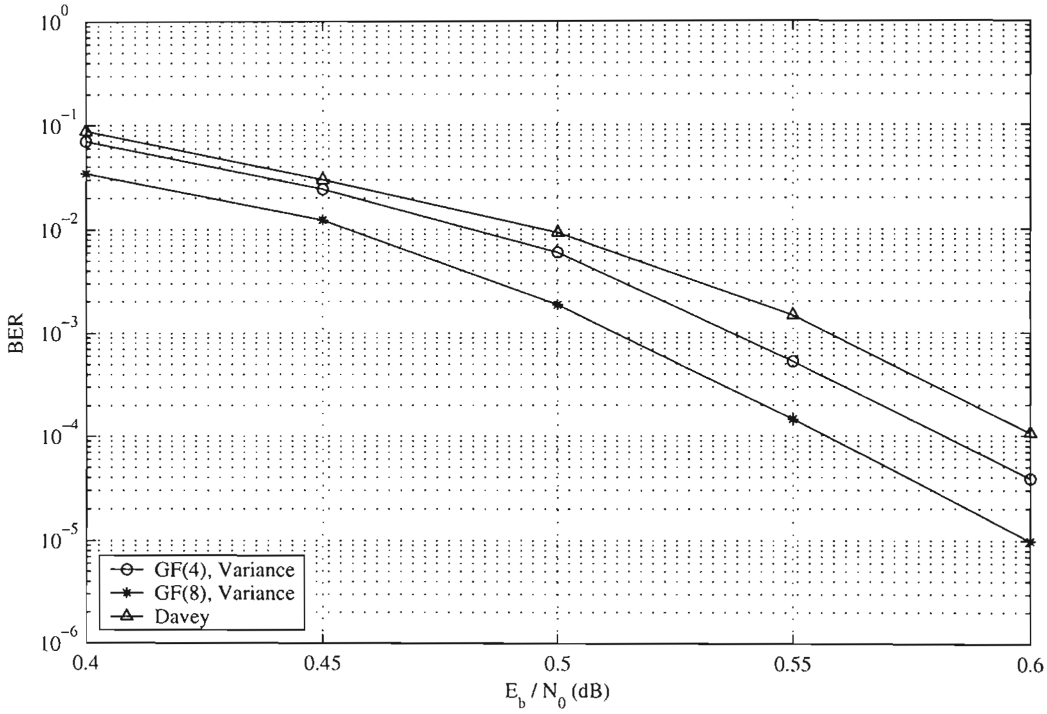

Figure 4.15: Simulation results for the $GF(4)$ and $GF(8)$ LDPC codes from Table 4.5 with $N = 60\ 000$, optimised at $E_b/N_0 = 0.5$ dB.

4.8 Summary

The optimisation of non-binary LDPC codes, using EXIT charts, was proposed in this chapter. Binary and non-binary LDPC codes were discussed as well as the methods available for their optimisation. The encoding, decoding and construction of non-binary LDPC codes was described where a detailed description of the log domain Fourier transform decoding algorithm was presented.

EXIT charts were then proposed to optimise the design of non-binary LDPC codes for the AWGN channel. A new metric was presented to describe the mutual information of the non-binary decoder messages. Decoder models were developed for both the VND and CND where the *a priori* information was modelled using a Gaussian mixture distribution. Analytical expressions were given for the VND and CND EXIT curves for both regular and irregular codes. The EXIT curves obtained from the model and analysis closely matched the simulation results.

The optimisation of non-binary LDPC codes involved matching the EXIT curves of the VND and CND. Four cost functions were considered to assess this match and differential evolution was employed to find the profile which minimised the chosen cost function. It was shown that LDPC codes optimised using the variance cost function achieved the best performance. LDPC codes were optimised for $GF(4)$ and $GF(8)$. The optimised $GF(4)$ code outperformed the $GF(4)$ code optimised in [96]. The optimised $GF(8)$ code outperformed the optimised $GF(4)$ which confirmed that small gains in performance can be achieved by increasing the field size. The main advantage of the proposed EXIT chart approach, over the simulation based approach of [96], is that it is orders of magnitude more efficient and good codes can therefore be optimised very quickly.

Chapter 5

Non-Binary LDPC Codes for Multiple Antenna Systems

5.1 Introduction

In order to approach the information theoretic capacity of MIMO channels, many multiple antenna (MA) systems employing channel coding have been investigated in the literature. These systems are often referred to as space-time coded systems as they merge the fields of antenna diversity and channel coding thereby exploiting the benefits of both. In practice, one must design the MA system to achieve good BER performance and to facilitate implementation with realisable complexity. This performance/complexity tradeoff makes the design of MA systems a challenging problem.

The application of non-binary LDPC codes to MA systems is considered in this chapter. LDPC codes optimised for single antenna systems are not necessarily optimal for MA systems. To this end, the non-binary LDPC codes are optimised for the system of interest using a simulation based or extrinsic information transfer (EXIT) chart based cost function. It is demonstrated that MA systems employing non-binary LDPC codes, achieve a small gain over systems employing binary LDPC codes.

The chapter begins with a brief overview of the various MA systems proposed in the literature. The proposed non-binary LDPC coded MA system and methods chosen to optimise the LDPC codes for this system are then motivated. The system model is described in section 5.3. The optimisation of non-binary LDPC codes for this system is discussed in section 5.4 and 5.5 for the simulation and EXIT chart based approaches respectively. Simulation results are then presented for the different system architectures. Finally, the chapter is summarised in section 5.6.

5.2 Channel Coding for Multiple Antenna Systems

Many MA architectures exist and an overview of these can be found in [18, 21]. The relative performance of MA systems, in terms of link quality and capacity, is discussed in [114]. In this chapter only feedforward schemes are considered where channel state information (CSI) is available to the receiver but not the transmitter. The CSI is generally estimated using pilot symbols included in the transmitted frame. In this section an overview of MA systems is given including space-time and LDPC coded systems followed by a motivation for the proposed non-binary LDPC coded MA system.

5.2.1 Space-Time Codes

Space-time trellis codes (STTCs) were originally proposed in [23] and mark a milestone in the development of space-time coding schemes. These codes can be decoded using a multidimensional version of the Viterbi algorithm. STTCs have been shown to achieve a diversity gain equal to the number of transmit antennas as well as good coding gain in fading channels. These codes are designed to provide the best tradeoff between constellation size, data rate, diversity advantage and trellis complexity.

Space-time block codes (STBCs) were originally proposed for two transmit antennas in [24] and were then extended to an arbitrary number of transmit antennas in [25]. They achieve full diversity gain, equal to the number of the transmit antennas, but minimal coding gain. The advantage of STBCs over STTCs is that they can be maximum likelihood decoded using only linear processing at the receiver. The scheme proposed in [24] has been included in the CDMA-2000 and UMTS standards. These STBC schemes require CSI at the receiver which is difficult to estimate accurately in fast fading channels. Schemes which do not require CSI were investigated in [117–120].

The Bell laboratories layered space-time (BLAST) architecture [22,115] is effectively a spatial multiplexing scheme which aims to maximise the date rate of MIMO systems whereas STTCs and STBCs aim to maximise the diversity gain. BLAST systems are also referred to as layered space-time codes due to their layered structure and feature low complexity suboptimal receivers. Unlike STTCs and STBCs, the BLAST architecture does not achieve full diversity gain and requires that the number of receive antennas is greater than the number of transmit antennas. To address this issue and improve the performance of BLAST, linear dispersion codes were proposed in [116] where the substreams of data are transmitted in linear combinations over space and time.

5.2.2 Concatenated Space-Time Codes

It is well known that concatenated coding schemes can be used to improve a system's coding gain while maintaining a reasonable decoding complexity. If the turbo principle [9] is applied at the decoder, whereby extrinsic information is exchanged between constituent decoders in a iterative fashion, even larger coding gains can be achieved.

This concept has also been applied to space-time coding. The first such scheme was considered in [121] where a turbo trellis coded modulation (TCM) code was concatenated with a STBC. A number of serially concatenated schemes employing STBCs were also investigated in [122]. Systems with STTC component codes were considered in [123–127]. Iterative decoding was considered for the BLAST architecture in [128] where a Turbo-BLAST scheme was presented. In [129], a turbo-coded modulation system was proposed where the output of a turbo code was mapped to multiple transmit antennas. In all cases the concatenated systems demonstrated improved performance over systems employing a single component code.

5.2.3 LDPC Codes for Multiple Antenna Systems

In the space-time coding schemes discussed thus far, LDPC codes have not been considered. These codes have recently been rediscovered [11] and have demonstrated improved performance over turbo codes for long frame lengths [89]. In this section the literature on binary and non-binary LDPC coded MA systems is presented.

Binary LDPC Codes for MA Systems

A number of layered space-time architectures were proposed in [130] where regular LDPC codes were employed as the constituent codes. It was shown that the system employing LDPC constituent codes outperformed the same system employing convolutional constituent codes. The application of LDPC codes to MA systems with OFDM transmission was considered in [131–133]. In [131], LDPC component codes demonstrated improved performance over convolutional component codes. A LDPC coded MA system with iterative equalisation and decoding was presented in [134]. The concatenation of LDPC codes and STBCs have been considered by a number of authors [135–138]. In [137], the concatenated LDPC/STBC system outperformed the concatenated turbo/STBC system in fast fading channels.

The optimisation of LDPC codes for the MA system of interest was not considered in the systems discussed thus far. In most cases LDPC codes which achieve good performance in AWGN channels were used which may not be optimal in MIMO channels. In [139], LDPC codes were optimised using density evolution [88] for the LDPC coded MA OFDM system proposed in [132]. In order to reduce the complexity of density evolution the Gaussian approximation on the message densities was applied [99] which allowed the mean of the message densities to be tracked. The messages passed from the MIMO demodulator to the LDPC decoder were modelled using a Gaussian mixture distribution and the parameters determining the distribution were estimated using an expectation maximisation (EM) algorithm. This estimation needed to be performed on each iteration.

Irregular LDPC codes were optimised specifically for MA systems in [104] using extrinsic information transfer (EXIT) charts [100] and near capacity performance was achieved using frames of length 10^5 bits. Closed form expressions for the EXIT curves of the variable node decoder (VND) and check node decoder (CND) were obtained and a polynomial approximation was used for the EXIT curve of the MIMO detector. A closed form expression was then obtained for the EXIT curve of the combined MIMO detector and VND. By matching the combined MIMO/VND and CND EXIT curves optimal LDPC codes were designed. This method only requires function evaluations and is thus more computationally efficient than the technique proposed in [139] which requires the Gaussian mixture distribution parameters to be re-estimated on each iteration of the density evolution algorithm.

Non-Binary LDPC Codes for MA Systems

Non-binary LDPC codes have demonstrated improved performance over binary LDPC codes in the AWGN channel [96]. However the application of non-binary LDPC codes to MA systems was only investigated in [98] where a small improvement over binary LDPC codes was observed. Here LDPC codes optimised for the AWGN channel were employed and the optimisation of non-binary LDPC codes for the MA system was not examined.

5.2.4 Proposed System

The promising performance of binary LDPC codes in MA systems and the improved performance of non-binary over binary LDPC codes in the AWGN channel has motivated the investigation of non-binary LDPC codes in MA systems. The transmitter structure of the proposed non-binary LDPC coded MA system is different to the system proposed in [98] as explained in section 5.3. In addition, the system proposed here employs LDPC codes optimised for the MA system of interest and utilises feedback from the LDPC decoder to the MIMO detector which was not the case in [98].

The optimisation of binary LDPC codes for MA systems has been addressed in [104,139] but the optimisation of non-binary LDPC codes for MA systems has not been considered in the literature. As far as the author is aware, the only methods available for optimising non-binary LDPC codes, are the simulation based approach used in [96] and the EXIT chart approach proposed in the previous chapter. In this chapter, the optimisation of LDPC codes for short and long frame length codes is considered. The optimisation of LDPC codes using EXIT charts [104] or density evolution [88, 89] assumes the cycle free case in the bipartite graph which is only valid as the length of the code approaches infinity. These methods are therefore only useful for optimising long codes which may not be feasible in wireless systems due to delay constraints. The simulation based optimisation approach is computationally intensive for long codes and is therefore only useful for the optimisation of short codes.

For the optimisation of short codes the simulation based approach successfully applied in [96], to optimise non-binary LDPC codes for the AWGN channel, is utilised. Because the actual decoding process is simulated, this approach is appropriate for optimising short LDPC codes. A slight modification of the cost function used in [96] is introduced to simplify the optimisation process. Furthermore differential evolution is employed to optimise this cost function as opposed to the simplex method used in [96]. For long LDPC codes the EXIT chart approach, applied to the optimisation of non-binary LDPC codes in the previous chapter, is extended to MA systems.

5.3 System Model

Consider a wireless communication system with n_T transmit and n_R receive antennas, employing a non-binary LDPC encoder. Two such systems are investigated in this chapter, namely, the LDPC modulated system (LDPC-M) and the LDPC modulated system with decoder feedback (LDPC-MF).

The transmitter structures of the two systems are identical. The information bits are encoded by the non-binary LDPC encoder, interleaved, M-PSK modulated and simultaneously transmitted from the n_T transmit antennas. The received signals on the n_R receive antennas, corrupted by fading and noise, are demodulated and decoded by the LDPC-M receiver and iteratively demodulated and decoded by the LDPC-MF receiver. A more detailed description of the transmitter and receiver structures as well as the MIMO channel is now presented.

5.3.1 LDPC-M and LDPC-MF Transmitter

A block diagram of the LDPC-M and LDPC-MF transmitter is given in Fig. 5.1. The non-binary LDPC code is defined by a $m \times n$ parity check matrix $\boldsymbol{H}$ with elements drawn from the finite field $GF(q = 2^p)$. The LDPC code has rate $R = k/n$ where $k = n - m$. The $K = kp$ information bits $\underline{u}$, $u_i \in \{0, 1\}$, are encoded by the non-binary LDPC encoder to give $N = np$ coded bits $\underline{c}$ as described in section 4.3. These coded bits are then interleaved by π to give N interleaved bits $\tilde{\underline{s}}$. The block interleaver ensures that the p bits comprising the same LDPC encoded symbol are transmitted at a different time instance which results in each bit being corrupted by independent fading and noise. This introduces diversity for each LDPC encoded symbol and therefore reduces the probability that all of the p bits comprising the same symbol are severely corrupted by the channel.

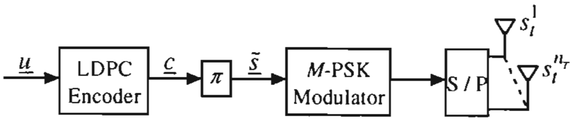

Figure 5.1: Block diagram of the LDPC-M and LDPC-MF transmitter.

The interleaved bits are modulated to give $n_M = N/p_M$, Gray-mapped, M-PSK symbols where $p_M = \log_2 M$. The modulated symbols are split into n_T streams of length $n_S = n_M/n_T$ and at each time instance $t = \{1, \ldots, n_S\}$ the symbols $\underline{s}_t = [s_t^1, \ldots s_t^{n_T}]$ are simultaneously transmitted from the n_T transmit antennas. These n_T symbols correspond to $n_T p_M$ interleaved coded bits. The total transmit power is equally divided between the transmit antennas and the rate of this system is $R_M = R n_T p_M$. This structure is very flexible as different spectral efficiencies can be easily obtained by adjusting the code rate, constellation size and number of transmit antennas.

The system proposed in [98] is different to the system proposed here. In [98], each LDPC encoded symbol was transmitted at the same time instance. For example the output of a $GF(16)$ non-binary LDPC encoder was mapped to 2 transmit antennas using QPSK modulation. For one receive antenna, each bit is corrupted by the same receiver noise and only 2 of the bits experience independent fading. In the system proposed here all 4 bits comprising a $GF(16)$ symbol are transmitted at different time instances and thus experience independent fading and receiver noise.

5.3.2 Channel Model

A rapid Rayleigh fading MIMO channel is considered where the correlation between antenna elements is assumed to be negligible. The signal received after matched filtering on receive antenna $i = \{1, \ldots, n_R\}$ is a noisy superposition of the n_T transmitted signals and is expressed as follows

$$r_t^i = \sum_{j=1}^{n_T} \alpha_t^{ij} s_t^j + \eta_t^i. \tag{5.1}$$

Here α_t^{ij} is the path gain between transmit antenna j and receive antenna i, and η_t^i is the AWGN noise introduced by receiver i. Both α_t^{ij} and η_t^i are modelled as independent, zero-mean complex Gaussian random sequences with variance 0.5 and σ_n^2 per dimension respectively. The noise variance is given by

$$\sigma_n^2 = \frac{n_T n_R}{2R_M E_b/N_0} \tag{5.2}$$

where E_b/N_0 is the signal-to-noise ratio, n_R normalises the receive antenna gain and n_T accounts for the division of power between the transmit antennas. The average energy per transmitted symbol s_t^j is set to unity.

5.3.3 LDPC-M Receiver

The structure of the LDPC-M receiver is shown in Fig. 5.2 which performs the operations of MIMO detection and LDPC decoding. It is assumed that perfect CSI is available to the receiver.

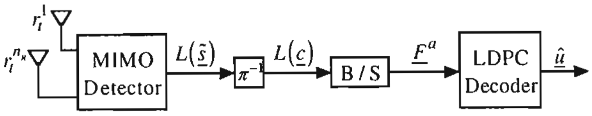

Figure 5.2: Block diagram of the LDPC-M receiver.

The log-likelihood ratios (LLRs) at the output of the MIMO detector are calculated as described in [129]. Let the $p_M n_T$ bits corresponding to the transmitted symbol vector $\underline{s}_t$ be denoted by

$$\underline{\tilde{s}}_t = [\tilde{s}_t^1, \ldots, \tilde{s}_t^{p_M}, \tilde{s}_t^{p_M+1}, \ldots, \tilde{s}_t^{p_M n_T}]. \tag{5.3}$$

The group of bits $\tilde{s}_t^1, \ldots, \tilde{s}_t^{p_M}$ corresponds to the transmitted M-PSK symbol s_t^1. Now the LLR of bit $l \in \{1, \ldots, p_M n_T\}$ of $\underline{\tilde{s}}_t$ is calculated by considering all the M^{n_T} possible symbol vectors $\underline{x} = [x^1, \ldots, x^{n_T}]$ as follows

$$\begin{aligned} L(\tilde{s}_t^l) &= \log \frac{P(\tilde{s}_t^l = 1 | r_t^1, \ldots, r_t^{n_R})}{P(\tilde{s}_t^l = 0 | r_t^1, \ldots, r_t^{n_R})} \\ &= \overset{*}{\max_{\underline{x}:\tilde{x}^l=1}} \{L(\underline{s}_t = \underline{x})\} - \overset{*}{\max_{\underline{x}:\tilde{x}^l=0}} \{L(\underline{s}_t = \underline{x})\} && (5.4) \\ L(\underline{s}_t = \underline{x}) &= -\frac{1}{2\sigma_n^2} \sum_{i=1}^{n_R} \left| r_t^i - \sum_{j=1}^{n_T} \alpha_t^{ij} x^j \right|^2 . && (5.5) \end{aligned}$$

The $\overset{*}{\max}$ operator denotes addition in the log domain as discussed in section 4.6.1 and $\underline{\tilde{x}} = [\tilde{x}^1, \ldots, \tilde{x}^{p_M n_T}]$ is the bitwise representation of symbol vector $\underline{x}$.

The LLRs $L(\underline{\tilde{s}})$ are passed through the inverse interleaver π^{-1} to obtain $L(\underline{c})$. Define $L(c_j^l)$ as the lth LLR in the jth group of p LLRs in $L(\underline{c})$ such that

$$L(\underline{c}) = [L(c_1^1), \ldots, L(c_1^p), L(c_2^1), \ldots, L(c_n^p)]. \tag{5.6}$$

The input to the LDPC decoder F_j^a is calculated by converting the bitwise LLRs $L(\underline{c})$ to symbol LLRs

$$F_j^a = \sum_{l:a_l=1} L(c_j^l) \tag{5.7}$$

where a_l is the lth bit of symbol $a \in GF(q)$.

The non-binary LDPC decoder then attempts to find the most likely estimate $\underline{\hat{u}}$ of the original information bits. The decoding proceeds as described in section 4.5 by iteratively updating the variable and check node messages Q_{ij}^a and R_{ij}^a until a valid codeword is found or the maximum number of decoding iterations is reached.

5.3.4 LDPC-MF Receiver

The performance of the LDPC-M system can be improved by feeding back information from the LDPC decoder to the MIMO detector in order to obtain an improved estimate of the demodulated symbols. This concept was proposed in [129] for a turbo coded MA system and was employed in the decoding of a binary LDPC coded MA system in [104, 139]. This gain in performance comes at the cost of increased receiver complexity.

A block diagram of the LDPC-MF receiver is given in Fig. 5.3 which performs the operations of MIMO detection and LDPC decoding. The structure is similar to that of the LDPC-M system but now a feedback loop is included. It is again assumed that perfect CSI is available to the receiver.

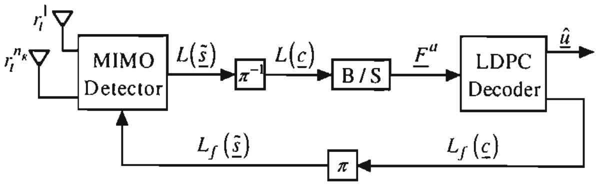

Figure 5.3: Block diagram of the LDPC-MF receiver.

The output of the MIMO detector is calculated by considering the received information as well as the information fed back from the LDPC decoder whereby

$$\begin{aligned} L(\tilde{s}_t^l) &= \max^*_{\underline{x}:\tilde{x}^l=1} \left\{ L(\underline{s}_t = \underline{x}) + \frac{1}{2}\sum_{k\neq l} \hat{x}^k L_f(\tilde{s}_t^k) \right\} \\ &\quad - \max^*_{\underline{x}:\tilde{x}^l=0} \left\{ L(\underline{s}_t = \underline{x}) + \frac{1}{2}\sum_{k\neq l} \hat{x}^k L_f(\tilde{s}_t^k) \right\}. \end{aligned} \tag{5.8}$$

Here $L_f(\tilde{s}_t^k)$ are the LLRs fed back from the LDPC decoder, $L(\underline{s}_t = \underline{x})$ is calculated according to (5.5) and $\hat{x}^k = 2\tilde{x}^k - 1$. The output LLR $L(\tilde{s}_t^l)$ of the MIMO detector is not dependent on the corresponding input LLR $L_f(\tilde{s}_t^l)$ fed back from the LDPC decoder which ensures that only extrinsic information is exchanged between the MIMO detector and the LDPC decoder.

The LLRs $L(\underline{\tilde{s}})$ are passed through the inverse interleaver π^{-1} to obtain $L(\underline{c})$. The LDPC decoder input F_j^a is given by

$$F_j^a = \sum_{l:a_l=1} L(c_j^l). \tag{5.9}$$

The LDPC decoder then performs one iteration by updating the variable and check node messages Q_{ij}^a and R_{ij}^a as described in section 4.5.

The LLRs $L_f(\underline{c})$ at the output of the LDPC decoder are calculated by summing over all check node messages connected to each variable node and converting these symbol LLRs to bitwise LLRs as follows

$$L_f(c_j^l) = \overset{*}{\max_{a:a_l=1}} \left\{ \sum_{k \in M_j} R_{kj}^a \right\} - \overset{*}{\max_{a:a_l=0}} \left\{ \sum_{k \in M_j} R_{kj}^a \right\} \tag{5.10}$$

where M_j is the set of all check nodes connected to variable node j. These LLRs are passed through the interleaver π to obtain $L_f(\underline{\tilde{s}})$, the input to the MIMO detector on the next iteration. Note that only extrinsic information is exchanged between the LDPC decoder and the MIMO detector as the decoder input F_j^a is not used in the calculation of $L_f(c_j^l)$.

In this way information is iteratively exchanged between MIMO detector and LDPC decoder until a valid codeword is found or the maximum number of decoding iterations is reached.

5.4 Optimisation: Simulation Approach

The performance of irregular LDPC codes is strongly influenced by the choice of the variable and check node profiles. It is therefore imperative that the optimal profiles are found. An irregular LDPC code is defined by a variable node profile $\underline{\lambda}$ and check node profile $\underline{\rho}$. The elements of $\underline{\lambda}$ ($\underline{\rho}$) are denoted by λ_i (ρ_i) which give the fraction of variable (check) nodes of degree i.

In this section a simulation based approach is proposed to optimise non-binary LDPC codes for the LDPC-M and LDPC-MF systems. A new cost function is presented and simulation results for the optimised systems are given.

5.4.1 Cost Function

The cost function in [96] measured the average number of iterations taken to find the correct codeword, to assess the effectiveness of the LDPC code defined by $\underline{\lambda}$ and $\underline{\rho}$. To ensure that all frames were eventually decoded, the SNR was increased at each decoding iteration. This method requires that the channel messages are updated for each iteration which adds unnecessary overhead to the calculation of the cost function, especially in the case of MA systems. In addition it was not clarified what starting SNR to use and at what rate the SNR should increase during the decoding process. It was found in practice that the choice of these two parameters influenced the optimised profiles.

To simplify the choice of parameters and to reduce the computational overhead, a slight modification to the cost function from [96] is introduced. The proposed cost function $C(\underline{\lambda}, \underline{\rho})$ measures the average number of iterations taken to decode N_{opt} frames of a LDPC code defined by the profiles $\underline{\lambda}$ and $\underline{\rho}$, at a fixed SNR S_{opt} where the number of decoding iterations is limited to I_{opt}. The complexity is thus reduced as the channel messages are calculated once. It was found in practice that best results are achieved if the code is optimised at a SNR where the optimised code can be decoded in approximately 30 iterations and I_{opt} is set to the maximum number of decoding iterations used in the actual simulation. In this way the only parameter to adjust, for the proposed cost function, is the SNR whereas in [96] both the SNR as well as the rate at which the SNR was increased needed to be adjusted.

The complexity of evaluating the cost function can be further reduced by considering the all-zero sequence which avoids the calculation of the generator matrix $\boldsymbol{G}$. The noisiness of the cost function can be reduced by generating each parity check matrix with the same random starting seed. The noise η_t^i and path gains α_t^{ij} are randomly generated for each cost function evaluation.

5.4.2 Optimisation Algorithm

The optimisation algorithm is required to minimise the cost function $C(\underline{\lambda}, \underline{\rho})$ subject to the following constraints

$$\begin{aligned} \sum_i \lambda_i &= 1, \quad 0 \leq \lambda_i \leq 1 && (5.11) \\ \sum_i \rho_i &= 1, \quad 0 \leq \rho_i \leq 1 && (5.12) \\ \sum_i i\lambda_i &= (1-R)\sum_i i\rho_i. && (5.13) \end{aligned}$$

This is a constrained, nonlinear, multidimensional optimisation problem where the cost function itself is noisy. In [96], the simplex method [141] was used to optimise the variable node profile. Recently differential evolution (DE) [113] has proven itself as a robust optimiser for multivariate problems and is discussed in detail in appendix C. Both the simplex and DE algorithms were considered but it was found that DE is more robust in the presence of noise.

5.4.3 Optimisation Results

In this section simulation results are presented to evaluate the BER performance of the optimised LDPC-M and LDPC-MF systems in an uncorrelated rapid Rayleigh fading channel. The codes are optimised using the simulation based approach.

Optimisation and Simulation Parameters

The notation $n_T \times n_R$ denotes a system with n_T transmit and n_R receive antennas. For both the LDPC-M and LDPC-MF systems the following parameters are used. The encoded frame length is $N = 6000$ bits where $N = np$ remains constant for different field sizes q. Rate 1/2 LDPC codes are employed which are constructed as described in section 4.4. Decoding is executed using log-FFT decoding algorithm explained in section 4.5 where the maximum number of decoding iterations is 100. Systems with 2 transmit and 1 or 2 receive antennas using Gray-mapped QPSK modulation are considered. Therefore the system rate is $R_M = 2$ which gives a bandwidth efficiency of 2 bps/Hz.

To limit the search space, LDPC codes with 3 variable node degrees and 1 check node degree are considered. The check node profile $\underline{\rho}$ is chosen prior to optimisation and the DE algorithm is required to find the variable node profile $\underline{\lambda}$ which minimises the cost function. This is achieved using the DE algorithm for free variable node degrees described in appendix C.2. The cost function is averaged over $N_{\text{opt}} = 100$ frames and maximum number of iterations I_{opt} is set to 100. The parameter S_{opt} is dependent on the system of interest.

Few authors have considered the optimisation of binary LDPC codes for MA systems and for this reason the range of existing results is limited. In [104], binary LDPC codes were optimised for a 2×1 MA system with decoder feedback but not for a 2×2 system. The LDPC codes optimised in [139] are for a MIMO OFDM system and therefore do not apply to this system. Because existing results are limited, only the 2×1 LDPC-MF system can be compared to results in the literature. Nevertheless to assess the performance of the optimised LDPC codes all codes are compared to the binary LDPC code optimised in [104]. This code was optimised for a 2×1 MA system with feedback using EXIT charts and is described by the profile $\rho_8 = 1,\ \lambda_2 = 0.4804,\ \lambda_3 = 0.4552,\ \lambda_{26} = 0.0644$.

Optimisation Results for the LDPC-M System

The optimised variable and check node profiles for the LDPC-M system are presented in Table 5.1 for $GF(2,4,8)$. The 2×1 and 2×2 systems are optimised at 6.5 dB and 3.25 dB respectively.

The simulation results for the optimised codes are given in Fig. 5.4 and Fig. 5.5. The optimised codes for the 2×1 LDPC-M system outperform the code from [104] which is denoted by 'Brink'. It is shown that by increasing the field size from $GF(2)$, a small gain in performance is obtained but the performance of the $GF(4)$ and $GF(8)$ codes is very similar. For the 2×2 LDPC-M system, it is again observed that the optimised

Table 5.1: LDPC code profiles for the LDPC-M system with $R = 1/2$ and QPSK modulation, optimised using the simulation approach.

	2×1, $S_{\text{opt}} = 6.5$ dB
$GF(2)$	$\rho_8 = 1,\ \lambda_2 = 0.40300,\ \lambda_3 = 0.48910,\ \lambda_{16} = 0.10790$
$GF(4)$	$\rho_7 = 1,\ \lambda_2 = 0.44440,\ \lambda_3 = 0.48300,\ \lambda_{16} = 0.07264$
$GF(8)$	$\rho_6 = 1,\ \lambda_2 = 0.54190,\ \lambda_3 = 0.40880,\ \lambda_{14} = 0.04927$
	2×2, $S_{\text{opt}} = 3.25$ dB
$GF(2)$	$\rho_8 = 1,\ \lambda_2 = 0.37720,\ \lambda_3 = 0.48510,\ \lambda_{13} = 0.13770$
$GF(4)$	$\rho_7 = 1,\ \lambda_2 = 0.43820,\ \lambda_3 = 0.46800,\ \lambda_{13} = 0.09382$
$GF(8)$	$\rho_6 = 1,\ \lambda_2 = 0.49410,\ \lambda_3 = 0.46100,\ \lambda_{14} = 0.04492$

codes outperform the code from [104]. Increasing the field size from $GF(2)$, gives a more significant performance gain than that achieved for the 2×1 system and the $GF(8)$ code has a small gain over the $GF(4)$ code.

Optimisation Results for the LDPC-MF System

Table 5.2 gives the optimised variable and check node profiles for the LDPC-MF system for $GF(2,4,8)$. The 2×1 and 2×2 systems are optimised at 4.5 dB and 2.5 dB respectively.

The performance of the optimised codes is investigated in Fig. 5.6 and Fig. 5.7. It is noted that the LDPC-MF system outperforms the LDPC-M system where a performance gain of 2 dB and 0.7 dB is achieved for the 2×1 and 2×2 systems respectively.

The optimised codes outperform the code from [104] which was optimised for a 2×1 MA system with decoder feedback using EXIT charts. As discussed in section 5.2.4 the EXIT chart approach is only appropriate for long codes. It can be clearly seen that for short codes this approach does not lead to good codes.

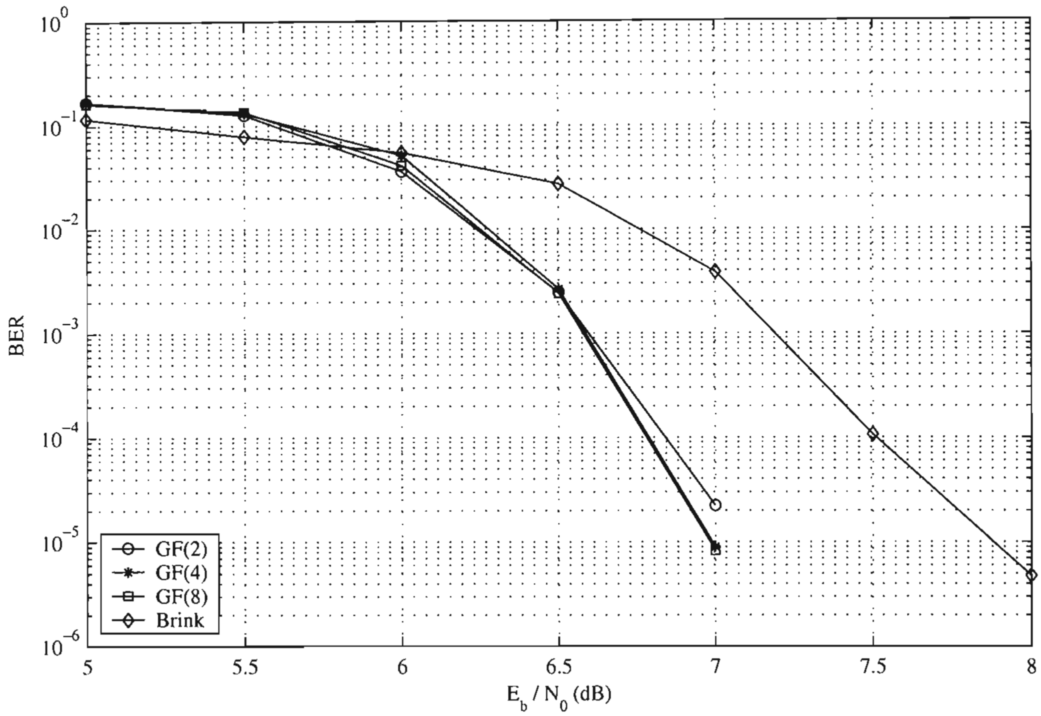

Figure 5.4: Performance of the 2 × 1 LDPC-M system with N = 6000, optimised using the simulation approach.

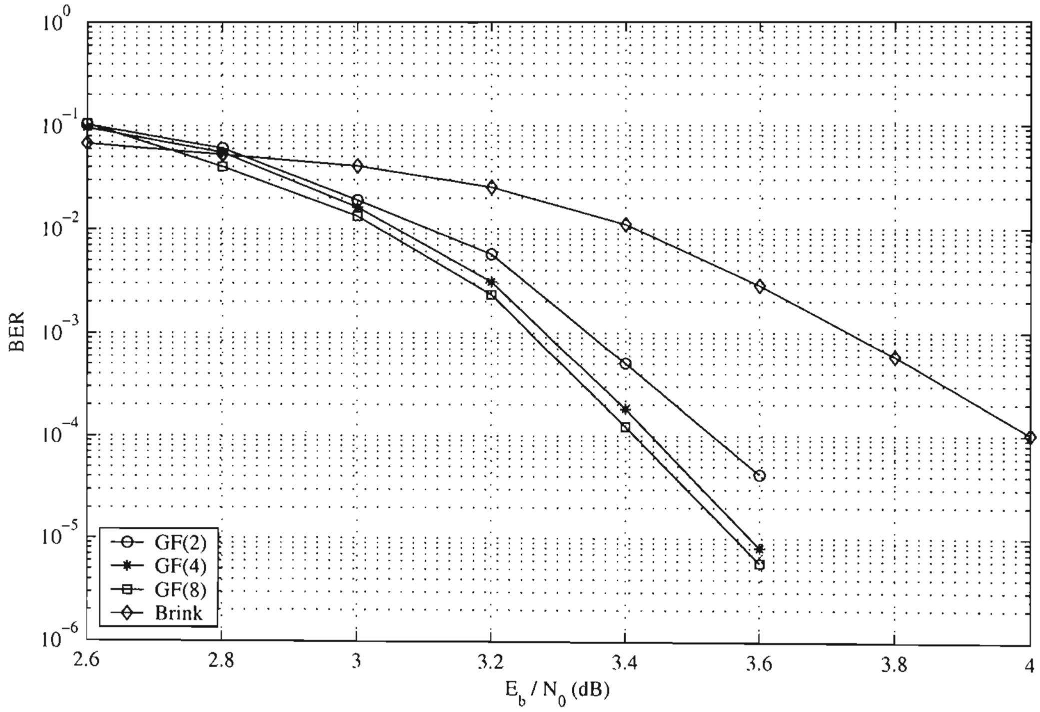

Figure 5.5: Performance of the 2 × 2 LDPC-M system with N = 6000, optimised using the simulation approach.

Table 5.2: LDPC code profiles for the LDPC-MF system with $R = 1/2$ and QPSK modulation, optimised using the simulation approach.

	2×1, $S_{\text{opt}} = 4.5$ dB
$GF(2)$	$\rho_7 = 1$, $\lambda_2 = 0.47000$, $\lambda_3 = 0.49120$, $\lambda_{28} = 0.03880$
$GF(4)$	$\rho_6 = 1$, $\lambda_2 = 0.64320$, $\lambda_3 = 0.32760$, $\lambda_{25} = 0.02923$
$GF(8)$	$\rho_5 = 1$, $\lambda_2 = 0.90850$, $\lambda_3 = 0.05746$, $\lambda_{15} = 0.03404$
	2×2, $S_{\text{opt}} = 2.5$ dB
$GF(2)$	$\rho_7 = 1$, $\lambda_2 = 0.38670$, $\lambda_3 = 0.54510$, $\lambda_{16} = 0.06821$
$GF(4)$	$\rho_7 = 1$, $\lambda_2 = 0.50420$, $\lambda_3 = 0.44300$, $\lambda_{22} = 0.05285$
$GF(8)$	$\rho_5 = 1$, $\lambda_2 = 0.72000$, $\lambda_3 = 0.24850$, $\lambda_{10} = 0.03144$

Increasing the field size results in a degradation in performance for both the 2 × 1 and 2 × 2 systems. It is conjectured that the performance of the LDPC-MF system is degraded, when the field size is increased, due to the conversion between bitwise and symbol LLRs at the input and output of the LDPC decoder. The non-binary LDPC decoder is attempting to find the most likely sequence of symbols which may not necessarily be the most likely sequence of bits. Therefore, improving the reliability of the bitwise LLRs at the MIMO detector output, by feeding back information from the LDPC decoder, may not always improve the reliability of the symbol LLRs at the LDPC decoder input. In this way the performance of the non-binary coded system is worse than the binary coded system which does not require conversion between symbol and bitwise LLRs.

On the other hand, for the LDPC-M system, there is only a conversion from bitwise to symbol LLRs at initialisation and from that point on the decoder attempts to find the most likely sequence of symbols. For this reason the performance of the LDPC-M system is improved by increasing the field size.

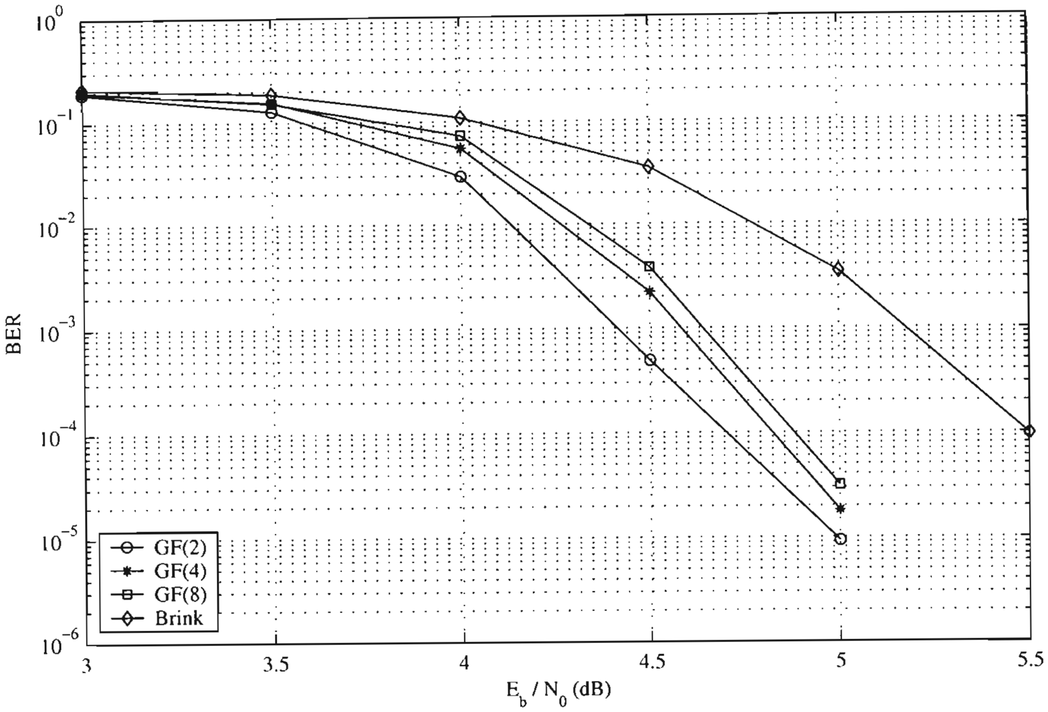

Figure 5.6: Performance of the 2 × 1 LDPC-MF system with $N = 6000$, optimised using the simulation approach.

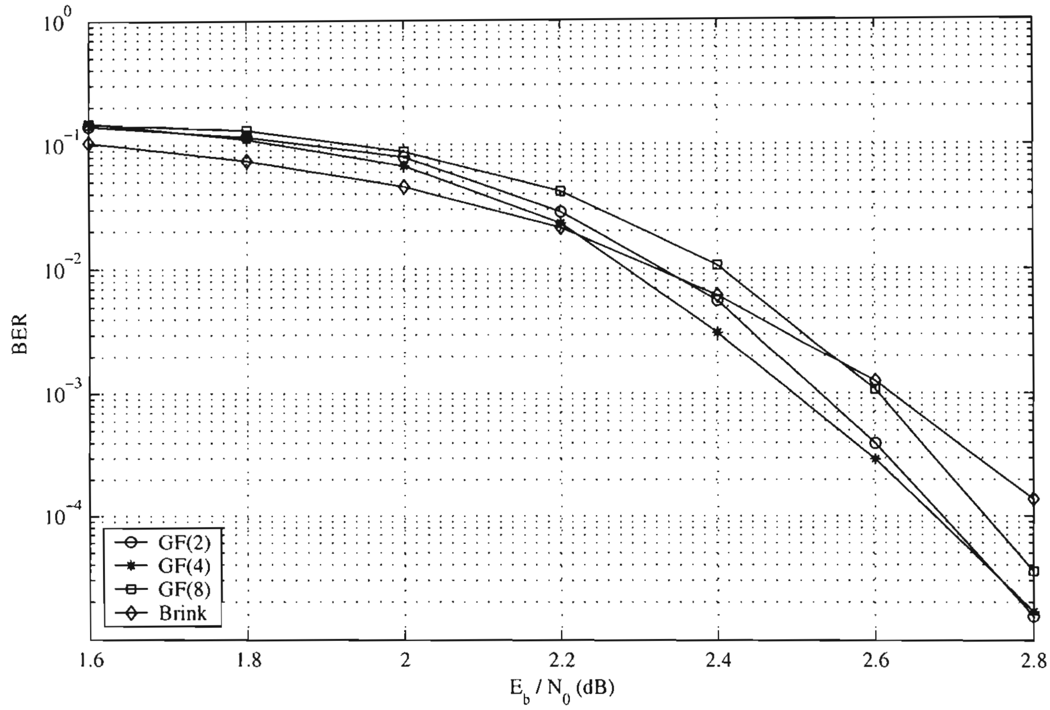

Figure 5.7: Performance of the 2 × 2 LDPC-MF system with $N = 6000$, optimised using the simulation approach.

5.5 Optimisation: EXIT Chart Approach

The EXIT chart approach, described in chapter 4, is now extended to optimise non-binary LDPC codes for the LDPC-M system. The calculation of the EXIT curves for the variable and check node decoders is discussed and simulation results for the optimised LDPC-M system are then given.

A block diagram of the iterative LDPC-M decoder is presented in Fig. 5.8. The set of variable and check nodes and the operations they perform is referred to as the variable node decoder (VND) and the check node decoder (CND). Here the notation I_{md} denotes the mutual information of the MIMO detector messages, I_{av} and I_{ev} denotes the mutual information at the VND input and output, and I_{ac} and I_{ec} denotes the mutual information at the CND input and output. This structure is very similar to the LDPC decoder for the AWGN channel given in Fig. 4.5 but here the VND receives information from the MIMO detector and not directly from the communications channel.

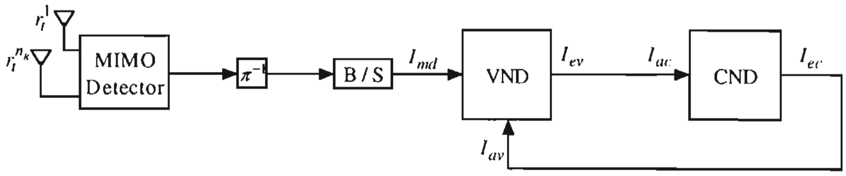

Figure 5.8: Iterative decoder for the LDPC-M system.

5.5.1 EXIT Curves for the Variable Node Decoder

Consider an arbitrary variable node of degree d_v which receives d_v messages $L^a_{i,iv}$ from the CND and one message L^a_{md} from the MIMO detector. The variable node computes the d_v output messages

$$L^a_{i,ov} = L^a_{md} + \sum_{k \neq i} L^a_{k,iv}. \tag{5.14}$$

Assume that this variable node is associated with symbol $x \in GF(q)$. It was found that the VND input messages $L^a_{i,iv}$ can also be modelled using the Gaussian mixture distribution given by (4.29). An exact expression for the MIMO detector messages is difficult to obtain analytically but it is straightforward to model these by simulation.

This is done by generating a frame $\underline{w}$ of random symbols $w_j \in GF(q)$ and converting these to a frame of bits $\underline{c}$. This frame is interleaved, modulated and transmitted as described in section 5.3. The signal received after matched filtering is given by (5.1) and the messages F_j^a, calculated according to (5.7), and their associated symbols w_j are stored in an ensemble. An ensemble of size 10^5 messages is used. The MIMO detector message L_{md}^a is drawn at random from this ensemble where the associated symbol $w_j = x$.

The EXIT curve of a variable node of degree d_v is given by

$$
\begin{aligned}
I_{ev}(I_{av}, d_v) &= J_v\left(\sqrt{d_v - 1} \cdot J_c^{-1}(I_{av})\right). && (5.15)\\
J_v(\sigma) &= I\left[X; \mathcal{B}(\underline{L}_{md} + \underline{L}_{iv}(\sigma))\right] && (5.16)\\
J_c(\sigma) &= I\left[X; \mathcal{B}(\underline{L}_{iv}(\sigma))\right] && (5.17)
\end{aligned}
$$

This expression is almost identical to that for the AWGN channel (4.32) but here $\underline{L}_{ch}$ is replaced by $\underline{L}_{md}$. The notation used here is described in section 4.6.2.

5.5.2 EXIT Curves for the Check Node Decoder

Consider an arbitrary check node of degree d_c which receives d_c messages $L_{i,ic}^a$ from the VND. Let x_i be the encoded symbol associated with each message $L_{i,ic}^a$. The d_c output messages $L_{i,oc}^a$ are computed according to (4.36) and the input messages are modelled as follows

$$L_{i,ic}^a(\sigma) = L_{i,c}^a(\sigma) + L_{i,md}^a. \tag{5.18}$$

Here $L_{i,c}^a(\sigma)$ is given by (4.38) and the d_c messages $L_{i,md}^a$ are drawn at random from the ensemble of messages F_j^a where $w_j = x_i$. As discussed in section 4.6.3 it is difficult to obtain analytical expressions for the CND EXIT curves and

$$I_{ec}(I_{ac}, d_c) = I_{ac}^{\alpha(d_c) \cdot I_{ac} + \beta(d_c)} \tag{5.19}$$

is fitted to the CND EXIT curves of interest.

5.5.3 EXIT Charts for Irregular LDPC Codes

The EXIT curve of an irregular code is simply the average of the component code EXIT curves where the VND and CND EXIT curves are given by

$$I_{ev}(I_{av}) = \sum_i \lambda_i^e \cdot I_{ev}(I_{av}, i) \tag{5.20}$$

$$I_{ec}(I_{ac}) = \sum_i \rho_i^e \cdot I_{ec}(I_{ac}, i). \tag{5.21}$$

In Fig. 5.9 and Fig. 5.10 the analytical EXIT curves, (5.20) and (5.21), are compared to the average decoding trajectory obtained from simulation for the 2 × 1 and 2 × 2 LDPC-M systems. The irregular $GF(4)$ code from [96] is considered where the variable and check node profiles are given in Table 4.1. The frame length is N = 12 000 bits and the decoding trajectory is averaged over 20 frames. It is observed that the analysis provides a good approximation of the decoding trajectory.

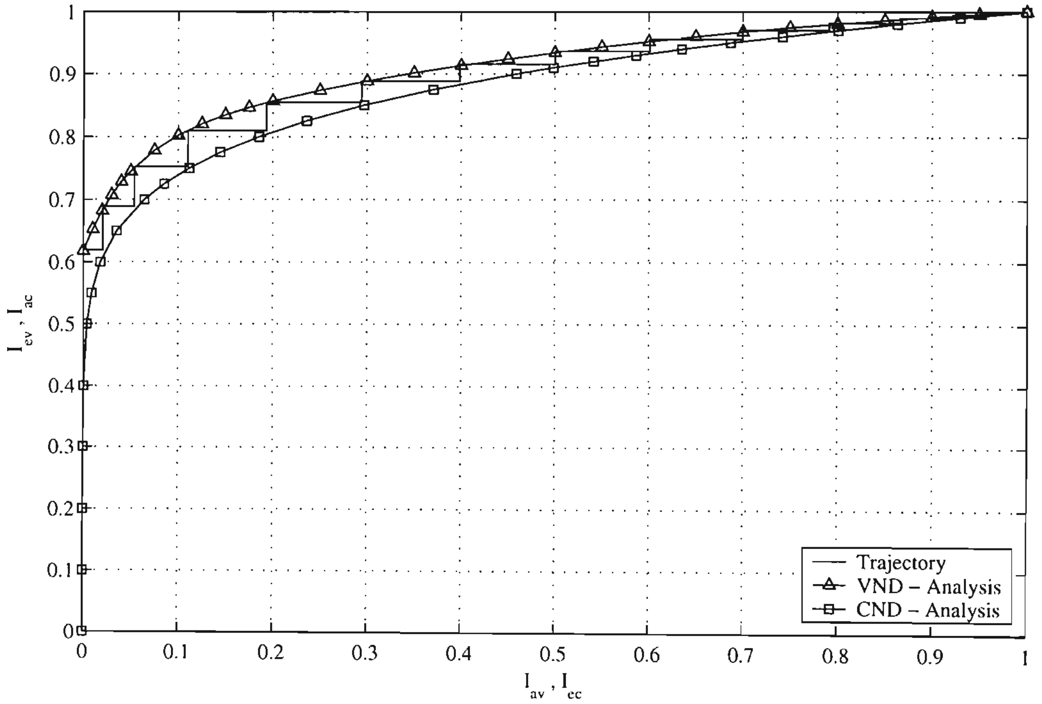

Figure 5.9: EXIT chart for the 2 × 1 LDPC-M system at $E_b/N_0 = 8$ dB.

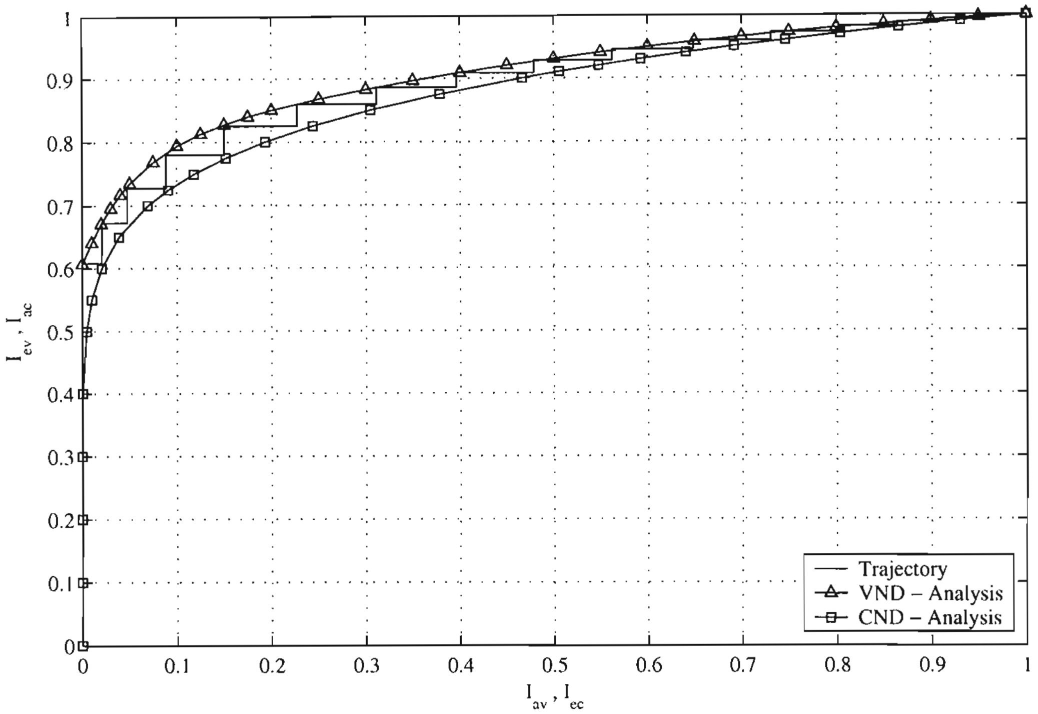

Figure 5.10: EXIT chart for the 2 × 2 LDPC-M system at $E_b/N_0 = 4$ dB.

5.5.4 Optimisation Results for the LDPC-M System

The EXIT chart approach is now used to optimise non-binary LDPC codes for the LDPC-M system. The search is performed using DE together with the variance cost function discussed in section 4.6.5. To limit the search space, rate 1/2 LDPC codes with 3 variable node degrees and 1 check node degree are considered and the procedure described in section 4.7.3 is used to search for the optimal code profile. The 2 × 1 and 2 × 2 LDPC-M systems are optimised at 5.5 dB and 2.5 dB respectively and the optimised profiles are presented in Table 5.3.

Simulation results are given in Fig. 5.11 and Fig. 5.12 for the optimised 2 × 1 and 2 × 2 LDPC-M systems. Here N = 60 000 and the simulation parameters are described in section 5.4.3. For both systems the optimised codes outperform the code from [104], although this code was optimised for the 2 × 1 LDPC-MF system. Increasing the field size is shown to improve system performance where a gain of 0.1 dB is observed, for both systems, by the $GF(8)$ code over the binary code . This indicates that the EXIT chart approach is also useful for optimising non-binary LDPC codes for MA systems.

Table 5.3: LDPC code profiles for the LDPC-M system with $R = 1/2$ and QPSK modulation, optimised using the EXIT chart approach.

	2×1, $E_b/N_0 = 5.5$ dB
$GF(2)$	$\rho_8 = 1,\ \lambda_2 = 0.45593,\ \lambda_3 = 0.41171,\ \lambda_{14} = 0.13236$
$GF(4)$	$\rho_7 = 1,\ \lambda_2 = 0.54988,\ \lambda_3 = 0.34513,\ \lambda_{13} = 0.10499$
$GF(8)$	$\rho_6 = 1,\ \lambda_2 = 0.67335,\ \lambda_3 = 0.23045,\ \lambda_{10} = 0.09619$
	2×2, $E_b/N_0 = 2.5$ dB
$GF(2)$	$\rho_8 = 1,\ \lambda_2 = 0.43751,\ \lambda_3 = 0.43181,\ \lambda_{14} = 0.13068$
$GF(4)$	$\rho_7 = 1,\ \lambda_2 = 0.53510,\ \lambda_3 = 0.34988,\ \lambda_{12} = 0.11501$
$GF(8)$	$\rho_6 = 1,\ \lambda_2 = 0.65200,\ \lambda_3 = 0.25486,\ \lambda_{10} = 0.09314$

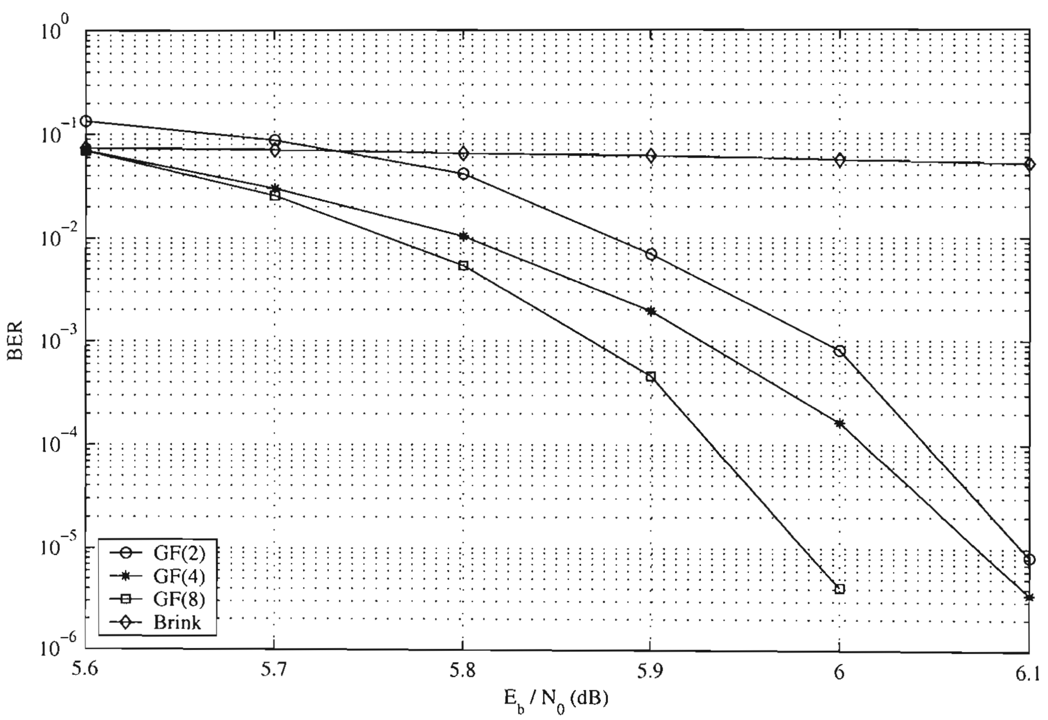

Figure 5.11: Performance of the 2×1 LDPC-M system with $N = 60\ 000$, optimised using the EXIT chart approach.

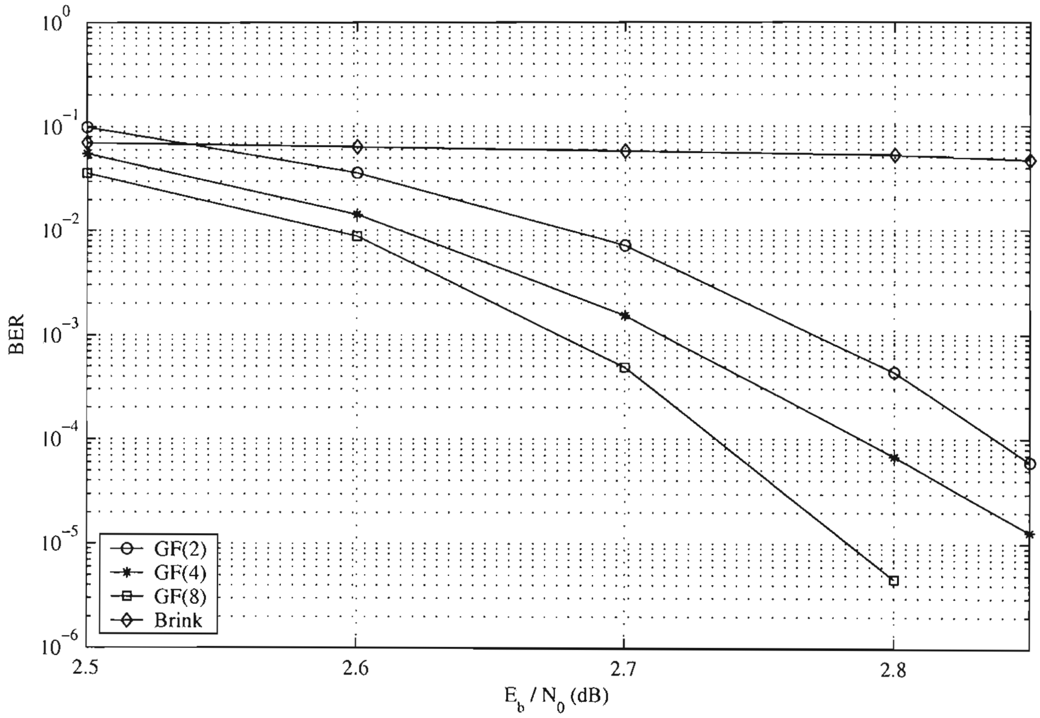

Figure 5.12: Performance of the 2 × 2 LDPC-M system with $N = 60\ 000$, optimised using the EXIT chart approach.

5.6 Summary

This chapter considered the effectiveness of non-binary LDPC codes in MA systems. Firstly, an overview of the literature on MA coding schemes was presented where it became clear that the application of non-binary LDPC codes to MA systems had not been well studied. Where non-binary LDPC codes had been considered, they had not been optimised for the system of interest. Two MA systems, employing non-binary LDPC codes, were considered. The LDPC-MF system fed back information from the LDPC decoder to the MIMO detector while the LDPC-M system did not. The transmitter and receiver structures for the proposed systems were described. Two approaches were proposed to optimise the non-binary LDPC codes for the system of interest, namely, the simulation based approach and the EXIT chart based approach.

LDPC codes over $GF(2,4,8)$ were investigated for systems with 2 transmit and 1 or 2 receive antennas. The optimisation of short codes for the LDPC-M and LDPC-MF system was carried out using the simulation based approach. It was shown that non-binary LDPC codes provide a small gain in performance over their binary counterparts for the LDPC-M system but not for the LDPC-MF system. The LDPC-MF system was shown to outperform the LDPC-M system but this came at the cost of increased receiver complexity. For long codes, the optimisation was performed using the EXIT chart approach where only the LDPC-M system was investigated. It was again shown that non-binary LDPC codes achieve superior performance to binary LDPC codes.

Chapter 6

Conclusions

The main focus of this thesis was on multiple input, multiple output (MIMO) systems where two important issues were considered. The first issue was concerned with the capacity of realistic MIMO channels. The second issue looked at the optimisation of LDPC based coding schemes for MIMO systems.

The wireless market and various wireless systems existing today were discussed in chapter 1. It became clear that future wireless systems must provide very high data rates but to achieve this, using conventional technologies, requires a large amount of radio spectrum which is both limited and expensive. Therefore, future systems will need to make optimal use of the available radio spectrum by using advanced technologies. Some of these technologies were discussed where MIMO systems were predicted to have the greatest potential to enhance system performance and spectral efficiency. The enhancements achieved by MIMO systems come at no increase in system bandwidth or transmitted power. The research performed was discussed and motivated and an overview of this thesis was presented. The original contributions of this thesis were presented and the publications, as a result of the research performed, were listed.

Chapter 2 considered the outage capacity of realistic MIMO channels. It was discussed that the spatial and temporal correlation are critical to the performance of future wireless systems. However, the impact of this on the capacity of MIMO channels had not been well studied. A MIMO channel with non-isotropic scattering at both ends of the radio link and receiver motion was considered but models for such a channel are not available in the literature. To this end, a geometric model for this channel was presented and a closed form expression describing the spatial and temporal correlation was derived. The derivation was shown to be accurate by comparison with correlation results obtained from the simulation of the geometric model and existing channel models in the literature. The method used to efficiently generate this channel, with the desired spatial and temporal correlation, was described where the vector autoregressive stochastic model was used. The outage capacity was then investigated where the effects of antenna spacing, array angle, degree of local scattering and receiver motion were examined. It was shown that it is important to optimise both ends of the radio link in order to achieve maximum capacity and that the antenna spacing is more critical at the receiver than at the transmitter. It was also established that the capacity increases linearly with respect to the number of transmit and receive antennas despite the presence of both spatial and temporal correlation. Spatial correlation was observed to decrease the slope of the capacity curve while temporal was shown to cause a downward shift of the capacity curve.

Analytical expressions for the capacity of MIMO channels provide useful insight into the factors effecting the capacity. Closed form expressions were derived for the ergodic capacity of spatially correlated MIMO channels in chapter 3. Spatial correlation at the receiver and at both the transmitter and receiver was considered. Analytical expressions for the former, were shown to be accurate by comparison with simulation results. Analytical expressions for the latter, were not amenable to numerical evaluation as they contained a hypergeometric function with 3 matrix arguments. The analysis is very general as it is based on the transmitter and receiver correlation matrices and can thus be applied to any spatially correlated MIMO channel.

In chapter 4, extrinsic information transfer (EXIT) charts were proposed as an efficient method for optimising non-binary LDPC codes for the AWGN channel. The encoding, decoding and code construction of non-binary LDPC codes was described. The *a priori* information of the variable node decoder (VND) and check node decoder (CND) was accurately modelled using a Gaussian mixture distribution. Analytical expressions were given for the EXIT curves of the VND and CND, for both regular and irregular codes. The analysis was shown to be accurate by comparison with simulation results. It was then shown that by matching the VND and CND EXIT curves, by minimising the variance of the error between these curves, non-binary LDPC could be optimised for the AWGN channel. Codes were optimised for $GF(4)$ and $GF(8)$ and the search was performed using differential evolution. The optimised $GF(4)$ code outperformed the $GF(4)$ code designed in [96] using a computationally intensive simulation based approach. The optimised $GF(8)$ code outperformed the $GF(4)$ code. It therefore concluded that the proposed EXIT chart approach is a promising method for efficiently optimising non-binary LDPC codes.

The performance of non-binary LDPC codes in multiple antenna (MA) systems was investigated in chapter 5. A brief overview of the existing coding schemes for MA systems was presented but few authors considered the application of non-binary LDPC codes to MA systems. Two non-binary LDPC coded MA systems were considered where the LDPC-MF system utilised decoder feedback and the LDPC-M system did not. Non-binary LDPC codes were optimised for both the LDPC-M and LDPC-MF systems using a simulation based approach and for the LDPC-M system using an EXIT chart based approach. Simulation results demonstrated that non-binary LDPC codes achieve a small gain in performance over binary LDPC codes for the LDPC-M system but not for the LDPC-MF system due to the conversion between bitwise and symbol LLRs in the decoder. The LDPC-MF system outperformed the LDPC-M system as the iterative demodulation and decoding improved the reliability of the demodulated symbols. Both the simulation and EXIT chart based optimisation approaches were shown to be useful for designing good LDPC codes for MA systems.

Appendix A

List of Acronyms

2G	Second Generation
3G	Third Generation
AMPS	Advanced Mobile Phone System
AR	AutoRegressive
AWGN	Additive White Gaussian Noise
BER	Bit Error Rate
BLAST	Bell laboratories LAyered Space-Time
CDMA	Code Division Multiple Access
cdmaOne	Code Division Multiple Access One
CND	Check Node Decoder
CSI	Channel State Information
DE	Differential Evolution
EDGE	Enhanced Data rates for GSM Evolution
EM	Expectation Maximisation
EXIT	EXtrinsic Information Transfer
FFT	Fast Fourier Transform
FEC	Forward Error Correction
GPRS	General Packet Radio Service
GSM	Global System for Mobile communication

HSDPA	High-Speed Downlink Packet-Access
LDPC	Low-Density Parity-Check
LLR	Log-Likelihood Ratio
MA	Multiple Antenna
MIMO	Multiple-Input–Multiple-Output
MSE	Mean Square Error
OFDM	Orthogonal Frequency Division Multiplexing
PDC	Personal Digital Cellular
SNR	Signal-to-Noise Ratio
STBC	Space-Time Block Code
STTC	Space-Time Trellis Code
TCM	Trellis Coded Modulation
TDMA	Time Division Multiple Access
ULA	Uniform Linear Array
UMTS	Universal Mobile Telecommunications System
VND	Variable Node Decoder
Wi-Fi	Wireless Fidelity
WiMAX	Worldwide Interoperability for Microwave Access

Appendix B

Finite Fields

In this appendix the finite fields $GF(2^p)$ are described in detail and lookup tables are given for the addition and multiplication operations over $GF(2^2)$ and $GF(2^3)$. More information on finite fields can be found in [140].

B.1 Finite Field Theory

A field is a set of numbers with addition and multiplication operations. The result of adding or multiplying two numbers in a particular field, is again a number in this field. For any field, there is a zero element and an identity element. For every number in the field, there is an additive and multiplicative inverse and the commutative, associative, and distributive laws are obeyed. Examples of fields are integers, real numbers and complex numbers which have an infinite number of elements. Finite fields have a finite number of elements and are commonly known as Galois fields in honour of the mathematician Evariste Galois who first studied finite fields.

The simplest finite field is $GF(n)$ which contains the set of integers $\{0, \ldots, n-1\}$ and the addition and multiplication operations are defined modulo n. A common example of such a field is the binary field $GF(2)$.

The finite field $GF(2^p)$ contains the set of integers $\{0, \ldots, 2^{p-1}\}$. An arbitrary integer $A \in GF(2^p)$ can be represented as a polynomial

$$A \rightarrow A(x) = a_{p-1}x^{p-1} + a_{p-2}x^{p-2} + \ldots + a_0 \tag{B.1}$$

where the coefficients $a_i \in \{0, 1\}$ correspond to the binary representation of A. For example if $A = 11$ then $A(x) = x^3 + x + 1$.

Arithmetic in $GF(2^p)$ is defined modulo an irreducible polynomial $G(x)$ which has no divisors other than itself and 1. The addition $\oplus$ and multiplication $\otimes$ operations in $GF(2^p)$ are defined by

$$A \oplus B \rightarrow A(x) + B(x) \tag{B.2}$$

$$A \otimes B \rightarrow A(x) \times B(x) \mod G(x) \tag{B.3}$$

where operations on the coefficients are defined using binary arithmetic but operations on the exponents are defined using integer arithmetic. To clarify the modulo operation, if $Q(x)$ is the quotient and $R(x)$ the remainder after division of $C(x)$ by $G(x)$ then $R(x) = C(x) \mod G(x)$.

An example is presented for the addition and multiplication operations over the finite field $GF(2^3)$ with irreducible polynomial $G(x) = x^3 + x + 1$. Let $A = 5$ and $B = 6$ which are represented by the polynomials $A(x) = x^2+1$ and $B(x) = x^2+x$ respectively. Now

$$\begin{aligned} A \oplus B &\rightarrow A(x) + B(x) \\ &= x + 1 \\ A \otimes B &\rightarrow A(x) \times B(x) \mod G(x) \\ &= x^4 + x^3 + x^2 + x \mod x^3 + x + 1 \\ &= x + 1 \end{aligned}$$

and converting from polynomial to integer representation $A \oplus B = 3$ and $A \otimes B = 3$.

B.2 Lookup Tables for Finite Field Arithmetic

Lookup tables are now presented for the addition and multiplication operations over $GF(2^2)$ and $GF(2^3)$. The two integers involved in the operation are given in the top row and left hand column. The intersection of the row and column containing the operands gives the result.

Table B.1: The addition $\oplus$ and multiplication $\otimes$ operations for $GF(2^2)$ with $G(x) = x^2 + x + 1$.

$\oplus$	0	1	2	3
0	0	1	2	3
1	1	0	3	2
2	2	3	0	1
3	3	2	1	0

$\otimes$	0	1	2	3
0	0	0	0	0
1	0	1	2	3
2	0	2	3	1
3	0	3	1	2

Table B.2: The addition $\oplus$ and multiplication $\otimes$ operations for $GF(2^3)$ with $G(x) = x^3 + x + 1$.

$\oplus$	0	1	2	3	4	5	6	7
0	0	1	2	3	4	5	6	7
1	1	0	3	2	5	4	7	6
2	2	3	0	1	6	7	4	5
3	3	2	1	0	7	6	5	4
4	4	5	6	7	0	1	2	3
5	5	4	7	6	1	0	3	2
6	6	7	4	5	2	3	0	1
7	7	6	5	4	3	2	1	0

$\otimes$	0	1	2	3	4	5	6	7
0	0	0	0	0	0	0	0	0
1	0	1	2	3	4	5	6	7
2	0	2	4	6	3	1	7	5
3	0	3	6	5	7	4	1	2
4	0	4	3	7	6	2	5	1
5	0	5	1	4	2	7	3	6
6	0	6	7	1	5	3	2	4
7	0	7	5	2	1	6	4	3

Appendix C

Differential Evolution

In this appendix the optimisation of the variable node degree profile using differential evolution is described where some modifications to the original algorithm are included to handle boundaries, constraints and integer variables.

The optimisation algorithm is required to minimise the cost function $C(\underline{\lambda}, \underline{\rho})$ of a rate R LDPC code subject to the following constraints:

$$\begin{aligned} \sum_i \lambda_i &= 1, \quad 0 \leq \lambda_i \leq 1 && \text{(C.1)} \\ \sum_i \rho_i &= 1, \quad 0 \leq \rho_i \leq 1 && \text{(C.2)} \\ \sum_i i\lambda_i &= (1-R) \sum_i i\rho_i. && \text{(C.3)} \end{aligned}$$

The variable node profile $\underline{\lambda}$ has elements λ_i which give the fraction of variable nodes of degree i. Similarly the check node profile $\underline{\rho}$ has elements ρ_i which give the fraction of check nodes of degree i.

This is a constrained, nonlinear, multidimensional optimisation problem and in the case of chapter 5 the cost function itself is noisy. Such optimisation problems are generally very difficult. Recently differential evolution (DE) [113] has proven itself as a robust optimiser for multivariate problems. The DE algorithm operates in parallel where a set of NP vectors are updated on each iteration. In this way, DE is able to escape local minima and avoid misconvergence to false minima. The handling of boundaries, constraints and integer variables was described in [142] which was not discussed in the original paper on DE. Some of these concepts are applied to the version of the DE algorithm presented here.

The DE algorithm is now described for two cases: fixed variable node degrees and free variable node degrees. This version of the algorithm is based on the DE1 scheme from [113] with some modifications to incorporate the handling of boundaries, constraints and integer variables.

C.1 Fixed Variable Node Degrees

In this case the check node profile and variable node degrees are selected prior to optimisation and the DE algorithm is required to find the variable node degree fractions which minimises the cost function.

Given a LDPC code of rate R, let d be the number of variable node degrees and let v_i be the fraction of variable nodes of degree w_i. Define $\underline{v} = [v_1, \ldots, v_d]$ and $\underline{w} = [w_1, \ldots, w_d]$ where $\underline{v}$ contains the non-zero entries of $\underline{\lambda}$ and $\underline{w}$ the corresponding degrees. Due to the constraints only $n = d - 2$ elements of $\underline{v}$ can be chosen freely. Let $\underline{x} = [v_3, \ldots, v_d]$ be the set of fractions to be optimised. The degree fractions v_1 and v_2 are calculated by solving the following two equations simultaneously:

$$\begin{aligned} v_1 + v_2 + \sum_{i=1}^{n} x_i &= 1, \quad 0 \leq v_1, v_2, x_i \leq 1 \qquad \text{(C.4)} \\ v_1 w_1 + v_2 w_2 + \sum_{i=1}^{n} x_i w_{i+2} &= (1 - R) \sum_{i} i\rho_i \qquad \text{(C.5)} \end{aligned}$$

Given a check node profile $\underline{\rho}$ and a set of variable node degrees $\underline{w}$ the vector $\underline{x}$ which minimises the cost function $C(\underline{x})$ is found using DE as follows for $i = \{1, \ldots, NP\}$ and $j = \{1, \ldots, n\}$:

1. **Initialisation:** Define a set of $NP = 10n$ vectors $\underline{x}_i = [x_{i,1}, \ldots, x_{i,n}]$ where $x_{i,j}$ is uniformly distributed in the interval $[0, 1]$. To speed up convergence each $\underline{x}_i$ can be initialised to $\underline{x}_{opt}$, an optimum solution from a previous search, with Gaussian

noise added to each element. The vector $\underline{x}_i$ is generated again if the corresponding v_1 and v_2, calculated using (C.4) and (C.5), are not in the interval $[0, 1]$.

2. **Mutation:** A set of trial vectors $\underline{z}_i$ are generated as follows

$$z_{i,j} = \begin{cases} x_{r_1,j} + F \cdot (x_{r_2,j} - x_{r_3,j}), & \text{if } a_j \leq CR \text{ or } b = j \\ x_{i,j}, & \text{otherwise} \end{cases} \tag{C.6}$$

   Here r_1, r_2, r_3 are unique integers which are distinct from i and chosen randomly from $\{1, \ldots, NP\}$. The variable a_j is uniformly distributed in the interval $[0, 1]$ and b is an integer randomly chosen from $\{1, \ldots, n\}$. For each trial vector $\underline{z}_i$ the random variables r_1, r_2, r_3, a_j and b are regenerated. F and CR are the differential evolution control parameters which remain constant during the search process. F is a constant which controls the amplification of the differential variations and is generally in the range $[0, 2]$. CR is the crossover probability and is confined to the range $[0, 1]$. Crossover helps to increase the diversity of the vectors where some elements of the new vector $\underline{z}_i$ are identical to the old vector $\underline{x}_i$. In this thesis $F = 0.5$ and $CR = 0.5$. Another $\underline{z}_i$ is generated if the elements $z_{i,j}$ or the corresponding v_1 and v_2 are not in the interval $[0, 1]$. The soft-constraint (penalty) approach discussed in [142] was not considered here because it is not possible to construct LDPC codes with $\lambda_i > 1$ or $\lambda_i < 0$.

3. **Selection:** DE uses the following selection criteria:

$$\underline{x}_i = \begin{cases} \underline{z}_i, & \text{if } C(\underline{z}_i) \leq C(\underline{x}_i) \\ \underline{x}_i, & \text{otherwise} \end{cases} \tag{C.7}$$

   What makes DE unique to other evolutionary algorithms is that the trial vector is not compared against all vectors in the current population but only against its counterpart in the current population.

4. **Termination:** The mutation and selection steps of the DE algorithm are repeated until the variance of $C(\underline{x}_i)$ falls below a desired threshold.

C.2 Free Variable Node Degrees

In this case only the check node profile is selected prior to optimisation and the DE algorithm is required to find the set of variable node degrees and degree fractions which minimises the cost function.

In the literature it was found that good LDPC codes have variable nodes of degree 2 and 3 [89,91,96]. To limit the search space, w_1 and w_2 were set to 2 and 3 respectively which allows only $m = d - 2$ elements of $\underline{w}$ to be chosen freely. Due to the constraints only $d - 2$ elements of $\underline{v}$ can be chosen freely. Let $\underline{x} = [v_3, \ldots, v_d, w_3, \ldots, w_d]$ be the length $n = 2m$ vector of degree fractions and degrees to be optimised. The vector $\underline{w}$ is ordered such that $w_1 \leq w_2 \leq \ldots \leq w_d$. The degree fractions v_1 and v_2 are calculated by solving the following two equations simultaneously:

$$\begin{aligned} v_1 + v_2 + \sum_{i=1}^{m} x_i &= 1 && \text{(C.8)} \\ 2v_1 + 3v_2 + \sum_{i=1}^{m} x_i \lfloor x_{i+m} \rfloor &= (1 - R) \sum_{i} i\rho_i && \text{(C.9)} \end{aligned}$$

The $\lfloor x \rfloor$ operator finds the floor of the real value x which allows the DE algorithm to continue operate with continuous variables. This is the method proposed to handle integer values in [142].

Given a check node profile $\underline{\rho}$ the vector $\underline{x}$ which minimises the cost function $C(\underline{x})$ is found using DE as follows for $i = \{1, \ldots, NP\}$ and $j = \{1, \ldots, n\}$:

1. **Initialisation:** Define a set of $NP = 10n$ vectors $\underline{x}_i = [x_{i,1}, \ldots, x_{i,n}]$ where $x_{i,j}$ is uniformly distributed in the interval $[0, 1]$ for $j = \{1, \ldots, m\}$ and $[4, d_{v,\max}]$ for $j = \{m+1, \ldots, n\}$. Here $d_{v,\max}$ is the maximum variable node degree considered. The vector $\underline{x}_i$ is generated again if the corresponding v_1 and v_2 are not in the interval $[0, 1]$.

2. **Mutation:** The mutation step is similar to that described previously where a set of trial vectors $\underline{z}_i$ are generated as follows

$$z_{i,j} = \begin{cases} x_{r_1,j} + F \cdot (x_{r_2,j} - x_{r_3,j}), & \text{if } a_j \leq CR \text{ or } b = j \\ x_{i,j}, & \text{otherwise} \end{cases} \qquad \text{(C.10)}$$

Another $\underline{z}_i$ is generated if the elements $z_{i,j}$ for $j = \{1, \ldots, m\}$ or the corresponding v_1 and v_2 are not in the interval $[0, 1]$. The trial vector is also regenerated if $z_{i,j}$ is not in the interval $[4, d_{v,\max}]$. In this thesis $F = 0.5$ and $CR = 0.5$.

3. **Selection:** The selection criteria is the same as that described previously:

$$\underline{x}_i = \begin{cases} \underline{z}_i, & \text{if } C(\underline{z}_i) \leq C(\underline{x}_i) \\ \underline{x}_i, & \text{otherwise} \end{cases} \tag{C.11}$$

4. **Termination:** The mutation and selection steps of the DE algorithm are repeated until the variance of $C(\underline{x}_i)$ falls below a desired threshold.

References

[1] GSM Association, "Membership and market statistics as at end of March 2004," http://www.gsmworld.com/news/statistics/pdf/mar04.pdf.

[2] M. Frodigh, S. Parkvall, C. Roobol, P. Johansson and P. Larsson, "Future-generation wireless networks," *IEEE Pers. Commun.*, pp. 10–17, Oct. 2001.

[3] J. Vriendt, P. Lainé, C. Lerouge and X. Xu, "Mobile network evolution: A revolution on the move," *IEEE Commun. Mag.*, pp. 104–111, April 2002.

[4] L. Philippe, B. Dietrich, B. Christophe and F. Laurence, "WiMAX, making ubiquitous high-speed data services a reality," *Alcatel Strategy White Paper*, http://www.alcatel.com/publications.

[5] P. Johansson, M. Kazantzidis, R. Kapoor and M. Gerla, "Bluetooth: An enabler for personal area networking," *IEEE Network*, pp. 28–37, Sep. 2001.

[6] T. S. Rappaport, A. Annamalai, R. M. Buehrer and W. Tranter, "Wireless communications: Past events and a future perspective," *IEEE Commun. Mag.*, 50th Anniversary Issue, pp. 148–161, May 2002.

[7] Y. Kim, B. J. Jeong, J. Chung, C. Hwang, J. S. Ryu et al., "Beyond 3G: Vision, requirements, and enabling technologies," *IEEE Commun. Mag.*, pp. 120–124, Mar. 2003.

[8] J. G. Proakis, *Digital Communications.* McGraw-Hill Companies, Inc., fourth ed., 2001.

[9] C. Berrou, A. Glavieux and P. Thitimajshima, "Near Shannon limit error-correcting coding and decoding: Turbo codes," in *Proc. IEEE ICC '93*, Geneva, Switzerland, May 1993, pp. 1064–1070.

[10] R. G. Gallager, "Low-density parity-check codes," *IEEE Trans. Inform. Theory*, vol. IT-8, pp. 21–28, Jan. 1962.

[11] D. J. C. MacKay, "Good error-correcting codes based on very sparse matrices," *IEEE Trans. Inform. Theory*, vol. 45, pp. 399–431, Mar. 1999.

[12] R. Nee and R. Prasad, *OFDM for Wireless Multimedia Communications.* Artech House, 2000.

[13] S. Verdú, *Multiuser Detection.* Cambridge University Press, 1998.

[14] R. T. Derryberry, S. D. Gray, D. M. Ionescu, G. Mandyam and B. Raghothaman, "Transmit diversity in 3G CDMA systems," *IEEE Commun. Mag.*, pp. 68–75, April 2002.

[15] J. H. Winters, "Smart antennas for wireless systems," *IEEE Pers. Commun.*, pp. 23-27, Feb. 1998.

[16] I. E. Telatar, "Capacity of multi-antenna Gaussian channels," Tech. Rep. #BL0112170-950615-07TM, AT&T Bell Laboratories, 1995.

[17] G. J. Foschini and M. J. Gans, "On limits of wireless communications in a fading environment when using multiple antennas," *Wireless Personal Communications*, vol. 6, pp. 311–335, Mar. 1998.

[18] D. Gesbert, M. Shafi, D. Shiu, P. J. Smith and A. Naguib, "From theory to practice: An overview of MIMO space-time coded wireless systems," *IEEE J. Select. Areas Commun.*, vol. 21, pp. 281–301, April 2003.

[19] A. Alexiou and M. Haardt, "Smart antenna technologies for future wireless systems: Trends and challenges," *IEEE Commun. Mag.*, vol. 42, pp. 90–97, Sep. 2004.

[20] "Multiple-Input Multiple-Output in UTRA (Release 6)," 3GPP TR 25.876, V1.4.0, June 2004.

[21] B. Vucetic and J. Yuan, *Space-Time Coding.* John Wiley & Sons Ltd, 2003.

[22] G. J. Foschini, "Layered space-time architecture for wireless communication in a fading environment when using multiple antennas," *Bell Labs Tech. J.*, vol. 1, pp. 41–59, Autumn 1996.

[23] V. Tarokh, N. Seshadri and A. R. Calderbank, "Space-time codes for high data rate wireless communication: Performance criterion and code construction," *IEEE Trans. Inform. Theory*, vol. 44, pp. 744–765, Mar. 1998.

[24] S. M. Alamouti, "A simple transmit diversity technique for wireless communications," *IEEE J. Select. Areas Commun.*, vol. 16, pp. 1451–1458, Oct. 1998.

[25] V. Tarokh, H. Jafarkhani and A. R. Calderbank, "Space-time block codes from orthogonal designs," *IEEE Trans. Inform. Theory*, vol. 45, pp. 1456–1467, July 1999.

[26] B. Holter, "On the capacity of the MIMO channel - A tutorial introduction," in *Proc. Norwegian Signal Processing Conf.*, Trondheim, Norway, Oct. 2001.

[27] A. Goldsmith, S. A. Jafar, N. Jindal, S. Vishwanath, "Capacity limits of MIMO channels," *IEEE J. Select. Areas Commun.*, vol. 21, pp. 684–702, June 2003.

[28] T. L. Marzetta and B. M. Hochwald, "Capacity of a mobile multiple-antenna communication link in Rayleigh flat fading," *IEEE Trans. Inform. Theory*, vol. 45, pp. 139–157, Jan. 1999.

[29] E. Biglieri, G. Caire and G. Taricco, "Limiting performance of block-fading channels with multiple antennas," *IEEE Trans. Inform. Theory*, vol. 47, pp. 1273–1289, May 2001.

[30] M. K. Ozdemir, E. Arvas and H. Arslan, "Dynamics of spatial correlation and implications on MIMO systems," *IEEE Commun. Mag.*, vol. 42, pp. s14–s19, June 2004.

[31] D. Shiu, G. J. Foschini, M. J. Gans and J. M. Kahn, "Fading correlation and its effect on the capacity of multilelement antenna systems," *IEEE Trans. Commun.*, vol. 48, pp. 502–513, Mar. 2000.

[32] H. Bölcskei, D. Gesbert and A. J. Paulraj, "On the capacity of OFDM-based spatial multiplexing systems," *IEEE Trans. Commun.*, vol. 50, pp. 225–234, Feb. 2002.

[33] A. Abdi and M. Kaveh, "A space-time correlation model for multielement antenna systems in mobile fading channels," *IEEE J. Select. Areas Commun.*, vol. 20, pp. 550–560, April 2002.

[34] M. T. Ivrlac, W. Utschick and J. A. Nossek, "Fading correlations in wireless MIMO communication systems," *IEEE J. Select. Areas Commun.*, vol. 21, pp. 819–828, June 2003.

[35] F. Boixadera Espax and J. J. Boutros, "Capacity considerations for wireless MIMO channels," in *Proc. Workshop on Multiaccess, Mobility and Teletraffic for Wireless Communications*, Venice, Italy, Oct. 1999.

[36] D. Gesbert, H. Bölcskei, D. A. Gore and A. J. Paulraj, "Outdoor MIMO wireless channels: Models and performance prediction," *IEEE Trans. Commun.*, vol. 50, pp. 1926–1934, Dec. 2002.

[37] C. Chuah, D. N. C. Tse, J. M. Kahn and R. A. Valenzuela, "Capacity scaling in MIMO wireless systems under correlated fading," *IEEE Trans. Inform. Theory*, vol. 48, pp. 637–650, Mar. 2002.

[38] D. Chizhik, G. J. Foschini, M. J. Gans and R. A. Valenzuela, "Keyholes, correlations, and capacities of multielement transmit and receive antennas," *IEEE Trans. on Wireless Commun.*, vol. 1, pp. 361-368, Apr. 2002.

[39] J. W. Wallace and M. A. Jensen, "Spatial characteristics of the MIMO wireless channel: Experimental data acquisition and analysis," in *Proc. IEEE International Conference on Accoustics, Speech and Signal Processing*, vol. 4, May 2001, pp. 2497–2500.

[40] R. Stridh, B. Ottersten and P. Karlsson, "MIMO channel capacity on a measured indoor radio channel at 5.8 GHz," in *Proc. Asilomar Conf. on Signals, Systems and Computers*, vol. 1, Oct. 2000, pp. 733–737.

[41] D. P. McNamara, M. A. Beach and P. N. Fletcher, "Experimental investigation of the temporal variation of MIMO channels," in *Proc. IEEE VTC Fall '01*, vol. 2, Oct. 2001, pp. 1063–1067.

[42] P. Kyritsi, D. C. Cox, R. A. Valenzuela and P. W. Wolniansky, "Correlation analysis based on MIMO channel measurements in an indoor environment," *IEEE J. Select. Areas Commun.*, vol. 21, pp. 713–720, June 2003.

[43] J. P. Kermoal, L. Schumacher, K. I. Pedersen, P. E. Mogensen and F. Frederiksen, "A stochastic MIMO radio channel model with experimental validation," *IEEE J. Select. Areas Commun.*, vol. 20, pp. 1211–1226, Aug. 2002.

[44] C. C. Martin, J. H. Winters and N. R. Sollenberger, "MIMO radio channel measurements: Performance comparison of antenna configurations," in *Proc. IEEE VTC Fall '01*, vol. 2, Oct. 2001, pp. 1225–1229.

[45] P. Soma, D. S. Baum, V. Erceg, R. Krishnamoorthy and A. J. Paulraj, "Analysis and modeling of multiple-input multiple-output (MIMO) radio channel based on outdoor measurements conducted at 2.5 GHz for fixed BWA applications," in *Proc. IEEE ICC '02*, vol. 1, May 2002, pp. 272–276.

[46] H. Xu, M. Gans, D. Chizhik, J. Ling, P. Wolniansky and R. Valenzuela, "Spatial and temporal variations of MIMO channels and impacts on capacity," in *Proc. IEEE ICC '02*, vol. 1, May 2002, pp. 262–266.

[47] D. Chizhik, J. Ling, P. W. Wolniansky, R. A. Valenzuela, N. Costa and K. Huber, "Multiple-input–multiple-output measurements and modeling in Manhattan," *IEEE J. Select. Areas Commun.*, vol. 21, pp. 321–331, April 2003.

[48] K. Yu and B. Ottersten, "Models for MIMO propagation channels, a review," *J. Wireless Commun. Mobile Comput.*, vol. 2, pp. 653–666, Nov. 2002.

[49] K. Yu, M. Bengtsson, B. Ottersten, D. McNamara, P. Karlsson and M. Beach, "Modeling of wide-band MIMO radio channels based on NLoS indoor measurements," *IEEE Trans. Vehic. Tech.*, vol. 52, pp. 655–665, May 2004.

[50] W. C. Jakes, *Microwave Mobile Communications.* New York: Wiley, 1974.

[51] A. Abdi, J. A. Barger and M. Kaveh, "A parametric model for the distribution of the angle of arrival and the associated correlation function and power spectrum at the mobile station," *IEEE Trans. Vehic. Tech.*, vol. 51, pp. 425–434, May 2002.

[52] W. C. Y. Lee, "Level crossing rates of an equal-gain predetection diversity combiner," *IEEE Trans. Commun. Technol.*, vol. 18, pp. 417–426, 1970.

[53] R. B. Ertel, P. Cardieri, K. W. Sowerby, T. S. Rappaport and J. H. Reed, "Overview of spatial channel models for antenna array communication systems," *IEEE Personal Commun.*, vol. 5, pp. 10–22, Feb. 1998.

[54] J. Fuhl, A. F. Molisch and E. Bonek, "Unified channel model for mobile radio systems with smart antennas," *IEE Proc. Radar, Sonar, Navig.*, vol. 145, pp. 32–41, Feb. 1998.

[55] T. A. Chen, M. P. Fitz, W. Y. Kuo, M. D. Zoltowski and J. H. Grimm, "A space-time model for frequency nonselective Rayleigh fading channels with applications to space-time modems," *IEEE J. Select. Areas Commun.*, vol. 18, pp. 1175–1190, July 2000.

[56] A. Abdi and M. Kaveh, "A versatile spatio-temporal correlation function for mobile fading channels with nonisotropic scattering," in *Proc. IEEE Workshop on Statistical Signal Array Processing*, Aug. 2000, pp. 58–62.

[57] A. F. Molisch, "A generic model for MIMO wireless propagation channels," in *Proc. IEEE ICC '02*, vol. 1, May 2002, pp. 277-282.

[58] I. S. Gradshteyn and I. M. Ryzhik, *Table of integrals, series and products.* 5^{th} ed, A. Jeffrey, Ed. San Diego, CA: Academic, 1994.

[59] K. E. Baddour and N. C. Beaulieu, "Accurate simulation of multiple cross-correlated fading channels," in *Proc. IEEE ICC '02*, vol. 1, May 2002, pp. 267–271.

[60] K. E. Baddour and N. C. Beaulieu, "Autoregressive models for fading channel simulation," in *Proc. IEEE GLOBECOM '01*, vol. 2, Nov. 2001, pp. 1187-1192.

[61] D. W. Bliss, K. W. Forsythe and A. F. Yegulalp, "MIMO communication capacity using infinite dimension random matrix eigenvalue distributions," in *Proc. Thirty-Fifth Asilomar Conf. on Signals, Systems and Computers*, vol. 2, Nov. 2001, pp. 969–974.

[62] L. Hanlen and M. Fu, "MIMO wireless systems: Capacity limits for sparse scattering," in *Proc. 3rd Australian Communications Theory Workshop*, Feb. 2002.

[63] P. J. Smith and M. Shafi, "On a Gaussian approximation to the capacity of wireless MIMO systems," in *Proc. IEEE ICC '02*, vol. 1, May 2002, pp. 406–410.

[64] P. Smith and M. Shafi, "An approximate capacity distribution for MIMO systems," *IEEE Trans. Commun.*, vol. 52, pp. 887–890, June 2004.

[65] H. Ge, K. D. Wong, M. Barton and J. C. Liberti, "Statistical characterization of multiple-input multiple-output (MIMO) channel capacity," in *Proc. IEEE WCNC '02*, vol. 2, Mar. 2002, pp. 789–793.

[66] P. J. Smith and L. M. Garth, "Exact capacity distribution for dual MIMO systems in Ricean fading," *IEEE Commun. Lett.*, vol. 8, pp. 18–20, Jan. 2004.

[67] S. Loyka and A. Kouki, "New compound upper bound on MIMO channel capacity," *IEEE Commun. Lett.*, vol. 6, pp. 96–98, Mar. 2002.

[68] X. Mestre, J. R. Fonollosa and A. Pagès-Zamora, "Capacity of MIMO channels: Asymptotic evaluation under correlated fading," *IEEE J. Select. Areas Commun.*, vol. 21, pp. 829–838, June 2003.

[69] P. J. Smith, L. M. Garth and S. Loyka, "Exact capacity distributions for MIMO systems with small numbers of antennas," *IEEE Commun. Lett.*, vol. 7, pp. 481–483, Oct. 2003.

[70] C. Martin and B. Ottersten, "Asymptotic eigenvalue distributions and capacity for MIMO channels under correlated fading," *IEEE Trans. on Wireless Commun.*, vol. 3, pp. 1350–1359, July 2004.

[71] H. Shin and J. H. Lee, "Capacity of multiple-antenna fading channels: Spatial fading correlation, Double scattering, and keyhole," *IEEE Trans. Inform. Theory*, vol. 49, pp. 2636–2647, Oct. 2003.

[72] X. W. Cui and Z. M. Feng, "Lower capacity bound for MIMO correlated fading channels with keyhole," *IEEE Commun. Lett.*, vol. 8, pp. 500–502, Aug 2004.

[73] Ö. Oyman, R. U. Nabar, H. Bölcskei and A. J. Paulraj, "Characterizing the statistical properties of mutual information in MIMO channels," *IEEE Trans. Signal Processing*, vol. 51, pp. 2784–2795, Nov. 2003.

[74] P. J. Smith, S. Roy and M. Shafi, "Capacity of MIMO systems with semicorrelated flat fading," *IEEE Trans. Inform. Theory*, vol. 49, pp. 2781–2788, Oct. 2003.

[75] M. Chiani, M. Z. Win and A. Zanella, "On the capacity of spatially correlated MIMO Rayleigh-fading channels," *IEEE Trans. Inform. Theory*, vol. 49, pp. 2363–2371, Oct. 2003.

[76] R. J. Muirhead, *Aspects of Multivariate Statistical Theory.* New York: Wiley, 1982.

[77] A. T. James, "Distributions of matrix variates and latent roots derived from normal samples," *Ann. Math. Statist.*, vol. 35, pp. 475–501, 1964.

[78] K. I. Gross and D. St. P. Richards, "Total positivity, spherical series, and hypergeometric functions of matrix argument," *J. Approx. Theory*, vol. 59, pp. 224–246, 1989.

[79] C. G. Khatri, "On certain distribution problems based on positive definite quadratic functions in normal vectors," *Ann. Math. Statist*, vol. 37, pp. 468–479, 1966.

[80] N. A. S. Crowther and D. J. de Waal, "On the distribution of a generalised positive semidefinite quadratic form of normal vectors," *South African Statist. J.*, vol. 7, pp. 119-127, 1973.

[81] R. G. Gallager, *Low-Density Parity-Check Codes.* Cambridge, MA: MIT Press, 1963.

[82] D. J. C. MacKay and R. M. Neal, "Near Shannon limit performance of low-density parity-check codes," *Electron. Lett.*, vol. 32, pp. 1645–1646, Aug. 1996.

[83] V. V. Zyablov and M. S. Pinsker, "Estimation of the error-correction complexity of Gallager low-density codes," *Problemy Peredachi Informatsii*, vol. 11, pp. 23–36, 1975.

[84] R. M. Tanner, "A recursive approach to low complexity codes," *IEEE Trans. Inform. Theory*, vol. IT-27, pp. 533–547, Sept. 1981.

[85] N. Wiberg, *Codes and Decoding on General Graphs.* PhD thesis, Dept. of Electrical Engineering, Linköping, Sweden, 1996.

[86] M. Luby, M. Mitzenmacher, A. Shokrollahi, and D. Spielman, "Analysis of low density codes and improved designs using irregular graphs," in *Proc. 30th Annual ACM Symp. Theory of Computing*, pp. 249–258, 1998.

[87] M. G. Luby, M. Mitzenmacher, M. A. Shokrollahi and D. A. Spielman, "Improved low-density parity-check codes using irregular graphs," *IEEE Trans. Inform. Theory*, vol. 47, pp. 585–598, Feb. 2001.

[88] T. J. Richardson and R. L. Urbanke, "The capacity of low-density parity-check codes under message-passing decoding," *IEEE Trans. Inform. Theory*, vol. 47, pp. 619–637, Feb. 2001.

[89] T. J. Richardson, M. A. Shokrollahi and R. L. Urbanke, "Design of capacity-approaching irregular low-density parity check codes," *IEEE Trans. Inform. Theory*, vol. 47, pp. 619–637, Feb. 2001.

[90] S. Chung, G. D. Forney Jr., T. J. Richardson and R. Urbanke, "On the design of low-density parity-check codes within 0.0045dB of the Shannon limit," *IEEE Commun. Lett.*, vol. 5, pp. 58–60, Feb. 2001.

[91] J. Hou, P. H. Siegel and L. B. Milstein, "Performance analysis and code optimization of low density parity-check codes on Rayleigh fading channels," *IEEE J. Select. Areas Commun.*, vol. 19, pp. 924–934, May 2001.

[92] M. Lentmaier and K. Sh. Zigangirov, "On generalized low-density parity-check codes based on Hamming component codes," *IEEE Commun. Lett.*, vol. 3, pp. 248–250, Aug. 1999.

[93] J. Boutros, O. Pothier, and G. Zemor, "Generalized low density (Tanner) codes," in *Proc. IEEE ICC 99*, Houston, Texas, July 1999, pp. 441–445.

[94] M. C. Davey and D. J. C. MacKay, "Low-density parity-check codes over $GF(q)$," in *Proc. IEEE Inform. Theory Workshop*, June 1998, pp. 70–71.

[95] M. C. Davey and D. MacKay, "Low-density parity-check codes over $GF(q)$," *IEEE Commun. Lett.*, vol. 2, pp. 165–167, June 1998.

[96] M. C. Davey, Error-correction using low-density parity-check codes, *Ph.D. dissertation*, Univ. of Cambridge, Cambridge, U.K., Dec. 1999.

[97] H. Song and J. R. Cruz, "Reduced-complexity decoding of Q-ary LDPC codes for magnetic recording," *IEEE Trans. Magn.*, vol. 39, pp. 1081–1087, Mar. 2003.

[98] G. Li, I. J. Fair and W. A. Krzymień, "Low density parity check codes for space-time wireless transmission," in *Proc. Intl. Conference on Wireless Communications*, Calgary, Canada, July 2002.

[99] S. Chung, T. J. Richardson and R. L. Urbanke, "Analysis of sum-product decoding of low-density parity-check codes using a Gaussian approximation," *IEEE Trans. Inform. Theory*, vol. 47, pp. 657–670, Feb. 2001.

[100] S. ten Brink, "Convergence of iterative decoding," *Electron. Lett.*, vol. 35, pp. 806–808, May 1999.

[101] S. ten Brink, "Convergence behaviour of iteratively decoded parallel concatenated codes," *IEEE Trans. Commun.*, vol. 49, pp. 1727–1737, Oct. 2001.

[102] M. Tüchler, S. ten Brink and J. Hagenauer, "Measures for tracing convergence of iterative decoding algorithms," in *Proc. 4th Int. ITG Conf. Source and Channel Coding*, Berlin, Germany, Jan. 2002, pp. 53–60.

[103] A. Ashikhmin, G. Kramer and S. ten Brink, "Extrinsic information transfer functions: A model and two properties," in *Proc. Conf. Inform. Sciences and Systems*, Princeton, NJ, Mar. 2002, pp. 742–747.

[104] S. ten Brink, G. Kramer and A. Ashikhmin, "Design of low-density parity-check codes for modulation and detection," *IEEE Trans. Commun.*, vol. 52, pp. 670–678, April 2004.

[105] S. ten Brink and G. Kramer, "Design of repeat-accumulate codes for iterative detection and decoding," *IEEE Trans. Signal Processing*, vol. 51, pp. 2764–2772, Nov. 2003.

[106] M. Tüchler, "Design of serially concatenated systems depending on block length," *IEEE Trans. Commun.*, vol. 52, pp. 209–218, Feb. 2004.

[107] D. J. C. MacKay, S. T. Wilson and M. C. Davey, "Comparison of Constructions of Irregular Gallager Codes," *IEEE Commun. Lett.*, vol. 47, pp. 1149–1454, Oct. 1999.

[108] A. Grant, "Convergence of non-binary iterative decoding," in *Proc. IEEE GLOBECOM '01*, vol. 2, Nov. 2001, pp. 1058–1062.

[109] C. Schlegel and A. Grant, "Concatenated space-time coding," in *Proc. IEEE PIMRC '01*, Sep. 2001.

[110] H. Chen and A. Haimovich, "Convergence analysis for turbo trellis coded modulation," in *Proc. Conf. on Inform. Sciences and Systems*, Mar. 2004.

[111] S. Benedetto, D. Divsalar, G. Montorsi and F. Pollara, "Serial concatenation of interleaved codes: Performance analysis, design and iterative decoding," *IEEE Trans. Inform. Theory*, vol. 44, pp. 909–926, May 1998.

[112] M. Tüchler and J. Hagenauer, "EXIT charts of irregular codes," in *Proc. 2002 Conf. Inform. Sciences and Systems*, Princeton, NJ, Mar. 2002, pp. 748–753.

[113] R. Storn and K. Price, "Differential evolution - A simple and efficient adaptive scheme for global optimization over continuous spaces," *Progress Report TR-95-012*, Mar. 1995.

[114] S. Catreux, L. J. Greenstein and V. Erceg, "Some results and insights on the performance gains of MIMO systems," *IEEE J. Select. Areas Commun.*, vol. 21, pp. 839–847, June 2003.

[115] G. D. Golden, G. J. Foschini, R. A. Valenzuela and P. W. Wolniansky, "Detection algorithm and initial laboratory results using V-BLAST space-time communication architecture," *Electron. Lett.*, vol. 35, pp. 14–16, Jan. 1999.

[116] B. Hassibi and B. M. Hochwald, "High-rate codes that are linear in space and time," *IEEE Trans. Inform. Theory*, vol. 48, pp. 1804–1824, July 2002.

[117] V. Tarokh and H. Jafarkhani, "A differential detection scheme for transmit diversity," *IEEE J. Select. Areas Commun.*, vol. 18, pp. 1169–1174, July 2000.

[118] B. L. Hughes, "Differential space-time modulation," *IEEE Trans. Inform. Theory*, vol. 46, pp. 145–149, Nov. 2000.

[119] B. M. Hochwald and T. L. Marzetta, "Unitary space-time modulation for multiple-antenna communications in Rayleigh flat fading," *IEEE Trans. Inform. Theory*, vol. 46, pp. 543–564, Mar. 2000.

[120] B. M. Hochwald and W. Sweldens, "Differential unitary space-time modulation," *IEEE Trans. Commun.*, vol. 48, pp. 2041–2052, Dec. 2000.

[121] G. Bauch, "Concatenation of space-time block codes and "Turbo"-TCM," in *Proc. IEEE ICC '99*, Vancouver, Canada, June 6-10, 1999, pp. 1202-1206.

[122] T. H. Liew and L. Hanzo, "Space-time codes and concatenated channel codes for wireless communications," *Proc. IEEE*, vol. 90, pp. 187–219, Feb. 2002.

[123] X. Lin and R. S. Blum, "Improved space-time codes using serial concatenation," *IEEE Commun. Lett.*, vol. 4, pp. 221–223, July 2000.

[124] D. Tujkovic, "Recursive space-time trellis codes for turbo coded modulation," in *Proc. IEEE GLOBECOM '00*, San Francisco, CA, vol. 2, Nov. 2000, pp. 1010–1015.

[125] H. Su, E. Geraniotis, "Space-time turbo codes with full antenna diversity," *IEEE Trans. Commun.*, vol. 49, pp. 47–57, Jan. 2001.

[126] Y. Liu, M. P. Fitz and O. Y. Takeshita, "Full rate space-time turbo codes," *IEEE J. Select. Areas Commun.*, vol. 19, pp. 969–980, May 2001.

[127] V. Gulati and K. R. Narayanan, "Concatenated codes for fading channels based on recursive space-time trellis codes," *IEEE Trans. on Wireless Commun.*, vol. 2, pp. 118–128, Jan. 2003.

[128] M. Sellathurai and S. Haykin, "Turbo-BLAST for wireless communications: Theory and experiments," *IEEE Trans. Signal Processing*, vol. 50, pp. 2538–2546, Oct. 2002.

[129] A. Stefanov and T. M. Duman, "Turbo-coded modulation for systems with transmit and receive antenna diversity over block fading channels: System model, decoding approaches and practical considerations," *IEEE J. Select. Areas Commun.*, vol. 19, pp. 958–968, May 2001.

[130] K. L. Lo, S. Marinkovic, Z. Chen and B. Vucetic, "Performance comparison of layered space time codes," in *Proc. IEEE ICC '02*, May 2002.

[131] Y. Li and J. Moon, "Increasing data rates through iterative decoding and antenna diversity in OFDM based wireless communication," in *Proc. IEEE GLOBECOM '01*, vol. 5, Nov. 2001, pp. 3130–3134.

[132] B. Lu, X. Wang and K. R. Narayanan, "LDPC-based space-time coded OFDM systems over correlated fading channels: Performance analysis and receiver design," *IEEE Trans. Commun.*, vol. 50, pp. 74–88, Jan. 2002.

[133] H. Lee, "LDPC coded modulation MIMO OFDM transceiver: Performance comparison with MAP equalization," in *Proc. IEEE VTC Spring '03*, vol. 2, April 2003, pp. 1178–1182.

[134] H. Lee and V. Gulati, "Iterative equalization/decoding of LDPC code transmitted over MIMO fading ISI channels," in *Proc. IEEE PIMRC '02*, vol. 3, Sep. 2002, pp. 1330–1336.

[135] D. Barral , R. A. Carrasco and B. Acha, "Concatenation of space-time block codes and low-density parity-check codes," in *Proc. IEE/IEEE 3rd Intl. Symp. Commun. Systems, Networks and Digital Signal Proc.*, July 2002.

[136] J. Ha, A. N. Mody, J. H. Sung, J. R. Barry, S. W. McLaughlin and G. L. Stüber, "LDPC coded OFDM with Alamouti/SVD diversity technique," *Wireless Personal Communications*, vol. 23, issue 1, pp. 183–194, Oct. 2002.

[137] H. Futaki and T. Ohtsuki, "LDPC-based space-time transmit diversity schemes with multiple transmit antennas," in *Proc. IEEE VTC Spring '03*, vol. 4, April 2003, pp. 2589–2593.

[138] M. Y. Alias, F. Guo, S. X. Ng, T. H. Liew and L. Hanzo, "LDPC and turbo coding assisted space-time block coded OFDM," in *Proc. IEEE VTC Spring '03*, vol. 4, April 2003, pp. 2309–2313.

[139] B. Lu, G. Yue and X. Wang, "Performance analysis and design optimization of LDPC-coded MIMO OFDM systems," *IEEE Trans. Signal Processing*, vol. 52, pp. 348–361, Feb. 2004.

[140] R. Lidl and H. Niederreiter, *Introduction to finite fields and their applications.* Cambridge University Press, Cambridge, 1986.

[141] J. J. McKeown, D. Meegan and D. Sprevak, *An introduction to unconstrained optimisation.* Bristol : Hilger, 1990.

[142] J. Lampinen and I. Zelinka, "Mixed integer-discrete-continuous optimization by differential evolution, part 1: The optimization method," *5th International Mendel Conference on Soft Computing*, Brno, Czech Republic, June 1999.